THE DYNAMICS OF DNA-CAPPED GOLD NANOPARTICLE SUPERLATTICE ASSEMBLY IN ELECTROLYTE SOLUTIONS

A Dissertation

Presented to the Faculty of the Graduate School

Of Cornell University

In Partial Fulfillment of the Requirements for the Degree of

Doctor of Philosophy

By

Thomas Louis Frederic Derrien

May 2017

THE DYNAMICS OF DNA-CAPPED GOLD NANOPARTICLE SUPERLATTICE ASSEMBLY IN ELECTROLYTE SOLUTIONS

Thomas L. Derrien

Cornell University 2012

Highly ordered nanoparticle arrays, or nanoparticle superlattices, are a sought after class of materials due to their novel physical properties, distinct from both the individual nanoparticle and the bulk material from which they are composed. Several successful methods have been established to produce these exotic materials. One method in particular, DNA-mediated assembly, has enabled a stunning variety of lattice structures to be constructed. By covalently conjugating DNA molecules to nanoparticle surfaces, this method uses the sequence binding specificity of DNA to mediate the large-scale assembly of nanoparticles. This method however, relied on complex sequence design, and is optimized to a very specific set of solution parameters, such as pH, ionic strength, and temperature.

Here, we sought to expand the parameter base in which DNA capped gold nanoparticles can form superlattices in solution. This was achieved by treating DNA as a generic polymer, namely by eliminating the complex base-pairing interactions, greatly simplifying the assembly process. In particular we aimed to understand the solution phase parameters governing the assembly dynamics of DNA-capped gold nanoparticles. The adsorption dynamics of individual DNA-capped gold nanoparticles on a positively charged substrate was first characterized in various electrolyte solutions, establishing a

kinetic model of adsorption. These same parameters were then used to facilitate the self-assembly of three-dimensional DNA-capped gold nanoparticles in solution. Finally, progress towards the application of solution phase two-dimensional nanoparticle superlattices was undertaken. We envision that this work characterizing and elucidating the solution phase dynamics of DNA-capped gold nanoparticles will serve to ultimately facilitate their application in functional materials.

BIOGRAPHICAL SKETCH

Thomas L. F. Derrien was born in Poissy, France but after several years moved to the United States, first to Seattle, WA, then to Cincinnati, OH. After graduating from Kings Mills High School in Kings Mills, OH, he pursued studies in chemistry at McGill University in Montreal, QC. Here he first earned a B.Sc. in 2007 followed by an M.Sc. in 2009 under the supervision of Prof. Bruce Lennox, studying the interactions of lipid bilayer with gold nanoparticles. After McGill, he then went to Cornell University, first earning an M.Eng, in biomedical engineering, working with Dr. Jonathan Butcher, before joining the group of Dan Luo in pursuit of a Doctor of Philosophy.

Thomas was awarded a National Science Foundation Integrative Graduate Education and Research Traineeship (IGERT): Materials for a Sustainable Future Fellowship in 2013.

To my family, and my fiancé, Beccy.

ACKNOWLEDGEMENTS

After many years as a graduate student I can conclude that successful research seems to me the optimization of many failed experiments, each with their many frustrations. It is for this reason that any success I have achieved has undoubtedly been facilitated by the unwavering support of countless individuals. First thanks are due to my supervisor, Dan Luo, for sharing his unique scientific vision and direction, encouragement, and teaching. The Luo Lab has proven to be an unmatchable environment to work due not only to the efforts of our supervisor but also to the diligent members, thank you all! In particular I would like thank Jason Kahn, who promoted many useful discussions and learning experiences, but in particular made the long hours in lab much more enjoyable with a constant dose of sarcasm and humor. Shawn Tan was my first lab mentor, and his meticulousness did not go unnoticed. Thanks to other past members, Ed Rice, Mark Hartman, Songming Peng and Michael Campolongo. I would also like to thank Detelf Smilgies for making this work possible, and whose constant enthusiasm for interfacial and colloidal phenomena have spawned many great discussions. Thanks are due to my committee members, Lois Pollack and Ulrich Wiesner, for contributing their invaluable intuition to the progress of this work.

Aside from academic support, I have been fortunate enough to have the generosity of family by my side; my parents who no matter how far away are always available, and my brothers who though also geographically distant, never fail to inject humor into daily life. Finally I would thank my fiancé, Beccy, whose presence and love throughout the last several years have sustained me, and who continues to inspire me everyday. Thank You.

TABLE OF CONTENTS

LIST OF FIGURES

CHAPTER ONE:

NANOPARTICLE SUPERLATTICES AND THEIR APPLICATIONS

1.1 NANOPARTICLES AS "ARTIFICAL ATOMS"

Colloidal nanocrystals, though often associated with contemporary science, have been the subject of fascination since antiquity. An iconic example of early nanocrystal application is the Lycurgus cup (Figure 1. 1), a 4th century cup made with dichroic glass, whose effect was achieved by mixing of both gold and silver nanoparticles into the glass. The striking appearance of the Lycurgus cup is the result of the nanoscale confinement of the individual nanoparticles, an attribute that gives nanoparticles properties unique from that of the bulk material from which they are made. The colloidal nanoparticles employed in the Lycurgus cup were obtained using finely ground powders of bulk silver and gold. To date, a host of synthesis techniques have been developed, resulting in nanoparticles with various, compositions, morphologies and symmetries. Even within groups of nanoparticles with the same composition, the resultant electronic, optical, and even magnetic properties can be tuned by morphological differences. It is this controlled variation which has led to the development a nanoparticle "periodic table."[1] Together, these special properties have allowed nanoparticles to be employed in applications ranging from optoelectronic devices[2], data storage[3], metamaterials[4], and biosensing[5].

Figure 1. 1: The Lycurgus cup, a 4th century roman vessel with dichroic glass. The cup appears (left) green when illuminated from the front, but appears (right) red when illuminated from behind, a result obtained by using a mixture of gold and silver colloidal nanocrystals. Redistributed under the creative commons license[6].

The distinction between the properties of individual nanoparticles and that of the bulk material has led to nanoparticles being widely referred to as "artificial atoms." As the name implies, these "atoms" can be used as building blocks from which to build "artificial solids."[7] Analogous to the disparity between the "artificial atoms" and the bulk material, "artificial solids" exhibit properties that are distinct from both. The disparity arises from the coupling of the individual nanoparticle properties, resulting in collective oscillations over the span of the entire "solid".

One such example is the tuning of nanoparticle plasmonics. Plasmons are the result of electronic excitations in response to visible light. The propagation of plasmons on

metal or semiconductor surfaces, resulting from excitation of conduction band electrons produce oscillations known as surface plasmons. In a bulk material, the scale of this propagation will appear infinite when compared to scale of the plasmons. However, the plasmon mode of a nanoparticle will experience nanoscale confinement, resulting in surface plasmons with frequencies within the optical range. It is for this very reason that nanoparticles have long been used to impart vibrant colors to glass, such as in the case of the Lycurgus cup. When within sufficient proximity to nearby nanoparticles these nanoscale plasmon modes can also couple to one another, resulting in plasmon frequency shifts. Arising from the electric field enhancement in the region between nanoparticle pairs, plasmon couplings will only occur within a narrow distance window, decreasing exponentially with larger separations. The relationship between nanoparticle separation has been experimentally determined by the El-Sayed group. Using lithographically produced nanoparticle pairs a universal plasmon ruler relation was determined[8]:

$$\frac{\Delta\lambda}{\lambda_0} \approx 0.18e^{-0.23\frac{S}{D}}, \qquad \text{(Equation 1.1)}$$

where $\Delta\lambda$ is the plasmon peak shift, λ_0 is the un-coupled plasmon peak, S is the nanoparticle separation and, D is the nanoparticle diameter. Extrapolating from equation 1.1, it can be seen that when the separation-to-diameter ratio is above 2.5, no significant coupling will occur. The above case only applies to spherical nanoparticles, as morphological differences can introduce multiple plasmon modes. Further complication can arise from large-scale assemblies, where one nanoparticles can experience near-field effects from multiple nanoparticles, such as those in "artificial solids." Such assemblies of nanoparticles are in fact the subjects of prolific study due to the plethora of complex phenomenon which arise from large scale nanoparticle constructs. In order to study the

underlying phenomena governing the physical properties of "artificial solids" precise control over the nanoparticle separation and arrangements must be achieved. For this reason the building of nanoparticle superlattices, where like in traditional crystal lattices, nanoparticles serve as the basis "atom", has become a central goal of nanotechnology.

1.2 NANOPARTICLE SUPERLATTICES: CONSIDERATIONS FOR ASSEMBLY

1.2.1 Anatomy of a Nanoparticle

Many considerations such as the wide variety of nanoparticle compositions, sizes and shapes that have been produced govern interparticle interactions, and thus ultimately determine the large-scale assemblies. An additional consideration that can influence particle-particle interactions is the capping ligand, the chemical moiety adsorbed to the surface of the nanoparticle. An abundance of chemical methods exist by which to add, modify, or exchange the nanoparticle capping ligands[4, 9], hence determining the class of interaction between adjacent nanoparticles. The capping ligand also serves a crucial role in allowing nanoparticles to exist in solution by preventing aggregation. This is because at short separations, London dispersion and van der Waals forces create an attractive potential between two particles, as first described by Hamaker in 1937[10]. The Hamaker potential, however, fails to address the repulsive interactions experienced by charged ligands in polar solvents. It was not until several years later the groups of Derjaguin and Landau[11], and Vervwey and Overbeek[12] both individually managed to derive a potential for charged colloids in solution. Further complications to particle-particle interactions may arise, such as charge inversion due to adsorbed counterions, but in general it is a

careful balance of these attractive-repulsive forces that must be weighed when constructing nanoparticle superlattices.

1.2.2 Assembly of Nanoparticle Superlattices: Balancing Forces at the Nanoscale

Precise positioning and morphology of nanoparticles can be readily achieved using photolithographic methods, however, such top-down approaches lack the scalability of bottom-up processes. Self-assembly of nanoparticles is one such approach with high-throughput scalability. As mentioned above, self-assembly of nanoparticles requires a careful balance of nanoscale forces. These forces can however, be minimized, and thus the assembly greatly simplified. One such method, though by no means trivial, is to assemble neutrally charged nanoparticles in non-polar solvents, thereby eliminating, or at least greatly reducing electrostatic considerations present in polar solvents.

A simple example of such a case is the drying mediated assembly of nanoparticles. By simply drop-casting a solution of nanoparticles in nonpolar solvents, and slowly drying the droplet on a surface, a variety of nanoparticle arrangements can be achieved.[13] In the simplest of these scenarios, the drying process can impose a convective flow to draw nanoparticles in close proximity, and when a critical volume fraction is reached, crystallization can occur.[14] Even in such carefully controlled systems absent of significant electrostatic forces, precise balancing of the nanoscale forces can result in significant differences. For example, Korgel and co-workers showed that by simply changing the solvent from chloroform to hexane, the direction of superlattice growth can be tuned, resulting in gold and silver nanoparticle superlattices with different morphologies. This morphological variance was found to arise from the discrepancy in the interparticle attraction experienced in the different solvents, with hexane displaying

an approximately 20% higher attraction. [15] The density of the nanoparticle capping ligand can also be used to fine-tune the three-dimensional superlattice structure. Choi *et al*. showed that a denser ligand shell will result in the more densely packed fcc crystal structure, while sparsely covered nanoparticles formed bcc crystallites[16] Similarly, ligand length, even on the sub-nanometer scale, can dramatically change the resulting superlattice order and structure. [17]

The influence of the ligand shell, even in non-polar solvents, illustrates another important class of nanoscale force at play: entropic forces. This emergent entropic force is typically repulsive, emanating from work required to compress the ligand shell. An equally important entropic contribution that follows from the presence of a ligand shell are attractive depletion forces. In a mixture of nanoparticles of different size, or nanoparticle-solute systems, when two nanoparticles are within a range in which the solute or smaller nanoparticle cannot fit between, the solute or nanoparticle is effectively excluded from this region. Normally, when the nanoparticles are sufficiently separated, this volume is inaccessible to the smaller nanoparticle/solute, and is referred to as the excluded volume. In close proximity, the overlap of the excluded volume between the two nanoparticles corresponds to a gain of volume for the smaller nanoparticle/solute (Figure 1. 2). This increase in available volume serves to increase the free energy of the system, effectively driving such mixtures to bring the larger nanoparticles together. Baranov *et al*. showed that by adding a depletant to a solution of semiconductor nanorods, vertically stacked and hexagonally arranged superlattices could be formed, whose micron-scale sheets could be fished out of solution.[18]

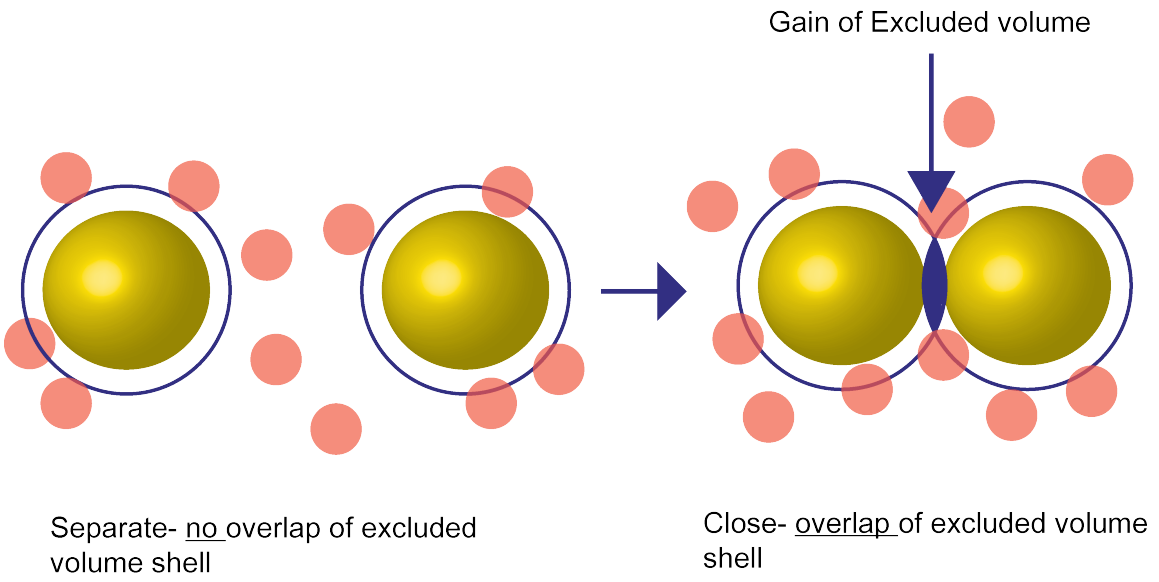

Figure 1. 2: Schematic of the depletion interaction. Normally at large nanoparticle separation, shown above on the left, no overlap of the excluded volume region occurs. However as the large gold nanoparticles become sufficiently close, the excluded volume region, shown by the blue rings, overlap. This results in an overall gain of available volume for the smaller nanoparticle, shown in red.

The examples above serve to highlight the complexity of the seemingly simple non-polar interactions of nanoparticles. Additional considerations must be made when assembling superlattices of charged nanoparticles. The added complexity arises from the presence of electrostatic interactions mentioned above. These can nevertheless be taken advantage of to carefully control the arrangements of nanoparticles at the nanoscale. Surprisingly, electrostatic interactions can even be tuned in solvents such as chloroform. Shevchenko *et al*. demonstrated that by adding surfactants to mixtures of nanoparticles in non-polar solutions, the charge state of the nanoparticles could be altered. These altered charge states could then be used to assemble oppositely charges nanoparticles into

numerous three-dimensional lattices.[19] In aqueous solutions, binary superlattices could also be formed using gold and silver nanoparticles of opposite charges. Using this method, several crystalline lattices were formed, including diamond-like lattices[20]. Electrostatic assembly of nanoparticle superlattices has even found success in forming hybrid biological-metal nanoparticle superlattices, where negatively charged protein cages were used to direct the self-assembly of positively charged gold nanoparticles, even assembling into non-naturally occurring crystal structures[21].

The use of biomolecules to direct colloidal self-assembly has been met with considerable success for one molecule in particular- deoxyribonucleic acid, DNA. In fact, its use as a nanoscale assembly scaffold is not limited to nanoparticles. The inherent properties specific to DNA, and how they can be exploited to construct self-assembled structures will be discussed in the next section.

1.3 DNA-MEDIATED ASSEMBLY

1.3.1 Properties of DNA

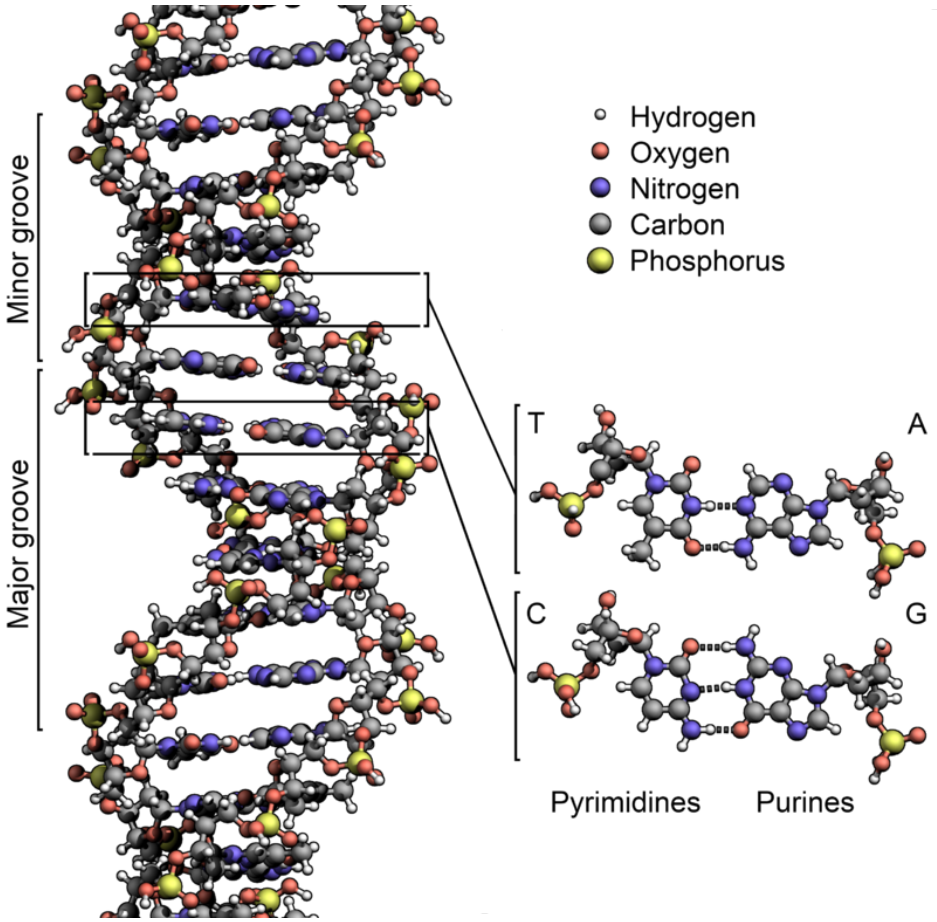

Figure 1. 3: Schematic of double stranded DNA. On the right the double helical structure is illustrated, and on the left are the Watson-Crick base pairing rules, showing the hydrogen bonding between nucleobases. Reprinted under the creative commons license[22].

It may seem unorthodox to adopt the genetic material of life, DNA, and repurpose it as a generic material, but in fact, it is it's evolutionarily optimized nature that lends itself so well to a myriad of other uses. The fundamental property of DNA that enables such multifunctionality is its "programmable" nature- the iconic Watson-Crick base

pairing rules, where adenine (A) nucleobases pair with thymine (T) and guanine (G) pairs with cytosine (C) (Figure 1. 3). As well as this ability for *de novo* design are its many structural variants. In its simplest form, single-stranded DNA (ssDNA) can be considered a flexible molecule, with a persistence length on the order of 0.5 nm. On the other hand, dsDNA is rigid material, with a persistence length of approximately 50 nm ten fold that of its ssDNA variant. In fact, by careful design, this rigidity can even be tuned. Pioneering work in the field of DNA nanotechnology by Seeman[23], showed that by using multi-stranded double and triple crossover DNA motifs, the rigidity of DNA structures can be increased. Nanometer-level precision is afforded by its well-characterized structure, each helical turn, comprising the minor (1.2 nm) and major grooves (2.2 nm), is approximately 10 bases in length, with each base separated by 0.34 nm. Further topological complexity can be introduced by combining more than two partially complementary ssDNAs, resulting in DNA structures referred to as X- and Y-DNAs (Figure 1. 4)[24-25]. Finally a litany of chemical procedures has been developed that allow almost limitless functionality to be introduced, a few examples from our groups work which are shown in Figure 1. 4.

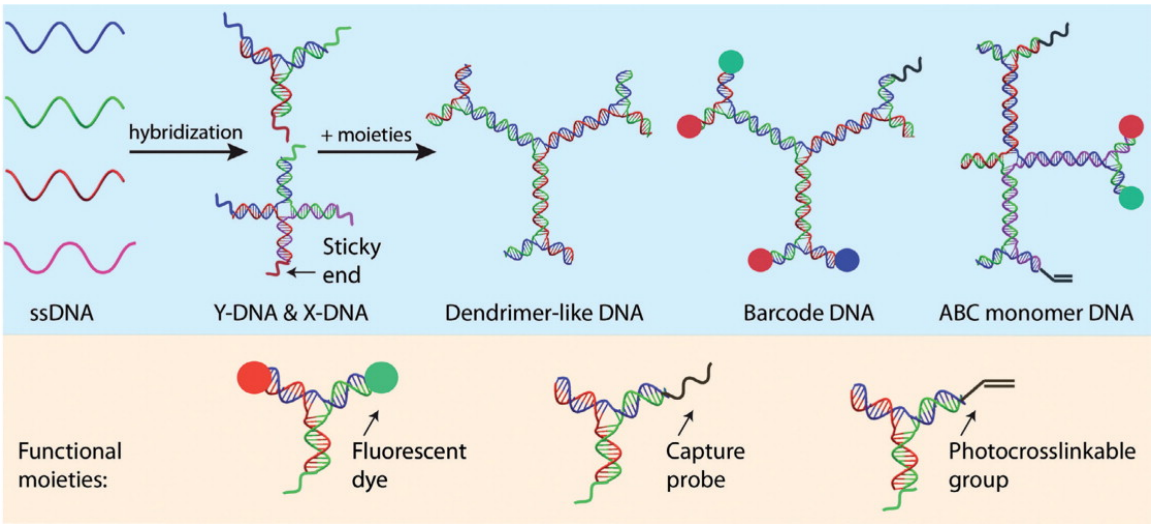

Figure 1. 4: Examples of the formations of functional DNA structures. (Top) Three or four ssDNA can be designed to hybridize into X- or Y-DNA. These can then be further combined to form dendrimer-like DNA with which additional chemical modifications can become barcode DNA or ABC monomer DNA. (Bottom) Examples of chemical modifications used to impart functionality mentioned above. Reprinted from reference 24.

1.3.2 DNA as a Multifunctional Assembler

The aforementioned structural versatility as well as the programmability of DNA have borne several self-assembly strategies. Building on the founding work of Seeman, methods such as DNA origami[26-27] and DNA tiles[28] have enabled the design of nanoscale scaffolds from which to further assemble nanoparticles. The success of these stratergies has culminated in a remarkable array of superlattices. Here, however, the focus is on using nanoparticles as "artificial atoms"- where the nanoparticles themselves serve as the scaffold. To this end, DNA can again be considered an ideal substance. Chemical modification, in the form of terminal thiols, can be used to rapidly form covalent bonds between DNA and the surface of inorganic nanocrystals such as gold and silver

nanoparticles. The result is a dense DNA ligand shell, which effectively imparts the functional nanoparticle core with the base-pairing capabilities of DNA. This approach was first demonstrated by Mirkin and co-workers in 1996[29], though the resulting structures were amorphous, the groundwork to one of the most prolific thrusts of nanotechnology was laid. More than a decade later, both the Mirkin[30] and Gang[31] groups independently first described the DNA-mediated assembly of large three-dimensional superlattices of nanoparticles with bcc crystal structure. Mirkin and co-workers also found that by using self-complementary DNA linkers, fcc morphology was favored. Remarkably, similar results were also achieved in our lab by the drying mediated assembly of non-base pairing DNA-gold nanoparticles, nanoparticles with a ligand shell composed of a generic DNA sequence unable to participate in Watson-Crick base pairing[32].

1.4 SIGNIFICANCE AND ORGANIZATION OF DISSERTATION

Since these pioneering works, the DNA-mediated assembly of nanoparticles has led to the realization of numerous elegant three-dimensional superlattices[33-37]. These methods, however, are not without their limitations. The DNA base pairing interactions, which enable the stunning array of possible arrangements of "artificial solids", are only able to exist in a narrow set of parameters. In this dissertation I will demonstrate efforts to expand the utility of DNA-functionalized gold nanoparticle (DNA-AuNPs) superlattices. Namely, I will build on our lab's previously reported work building two-dimensional nanoparticle superlattices from non-base pairing DNA-AuNPs at the air-water interface.[38-39] First, I will discuss efforts aimed at understanding the solution phase

dynamics of this system at a charged solid-liquid interface. Work extending these two-dimensional crystallites in the third dimension are then described. Finally, progress towards their application will be outlined. Here I aim to show that by eliminating the complex base pairing interactions of DNA-mediated nanoparticle assembly, and instead treating DNA as a generic polymer, that the assembly process can be simplified, without compromising its utility.

REFERENCES

1. Tan, S. J.; Campolongo, M. J.; Luo, D.; Cheng, W., Building plasmonic nanostructures with DNA. *Nat Nanotechnol* **2011,** *6* (5), 268-76.

2. Kamat, P. V.; Christians, J. A.; Radich, J. G., Quantum dot solar cells: hole transfer as a limiting factor in boosting the photoconversion efficiency. *Langmuir* **2014,** *30* (20), 5716-25.

3. Sun, S.; Murray, C. B.; Weller, D.; Folks, L.; Moser, A., Monodisperse FePt nanoparticles and ferromagnetic FePt nanocrystal superlattices. *Science* **2000,** *287* (5460), 1989-92.

4. Daniel, M. C.; Astruc, D., Gold nanoparticles: assembly, supramolecular chemistry, quantum-size-related properties, and applications toward biology, catalysis, and nanotechnology. *Chem Rev* **2004,** *104* (1), 293-346.

5. Lee, J.; Hernandez, P.; Lee, J.; Govorov, A. O.; Kotov, N. A., Exciton-plasmon interactions in molecular spring assemblies of nanowires and wavelength-based protein detection. *Nat Mater* **2007,** *6* (4), 291-5.

6. Johnbod, Wikimedia Commons. **2010**.

7. Yin, Y.; Alivisatos, A. P., Colloidal nanocrystal synthesis and the organic-inorganic interface. *Nature* **2005,** *437* (7059), 664-70.

8. Jain, P. K.; El-Sayed, M. A., Universal scaling of plasmon coupling in metal nanostructures: extension from particle pairs to nanoshells. *Nano Lett* **2007,** *7* (9), 2854-8.

9. Iravani, S.; Korbekandi, H.; Mirmohammadi, S. V.; Zolfaghari, B., Synthesis of silver nanoparticles: chemical, physical and biological methods. *Res Pharm Sci* **2014,** *9* (6), 385-406.

10. Hamaker, H. C., The London - Van Der Waals attraction between spherical particles. *Physica* **1937,** *4*, 1058-1072.

11. Derjaguin, B., Landau., L, Theory of the stability of strongly charged lyophobic sols and of the adhesion of strongly charged particles in solutions of electrolytes. *Acta Physico Chemica URSS* **1941,** *14* (633).

12. Verwey, E. J., Theory of the stability of lyophobic colloids. *J Phys Colloid Chem* **1947,** *51* (3), 631-6.

13. Ming, T.; Kou, X.; Chen, H.; Wang, T.; Tam, H. L.; Cheah, K. W.; Chen, J. Y.; Wang, J., Ordered gold nanostructure assemblies formed by droplet evaporation. *Angew Chem Int Ed Engl* **2008,** *47* (50), 9685-90.

14. Bishop, K. J.; Wilmer, C. E.; Soh, S.; Grzybowski, B. A., Nanoscale forces and their uses in self-assembly. *Small* **2009,** *5* (14), 1600-30.

15. Sigman, M. B., Jr.; Saunders, A. E.; Korgel, B. A., Metal nanocrystal superlattice nucleation and growth. *Langmuir* **2004,** *20* (3), 978-83.

16. Choi, J. J.; Bealing, C. R.; Bian, K.; Hughes, K. J.; Zhang, W.; Smilgies, D. M.; Hennig, R. G.; Engstrom, J. R.; Hanrath, T., Controlling nanocrystal superlattice symmetry and shape-anisotropic interactions through variable ligand surface coverage. *J Am Chem Soc* **2011,** *133* (9), 3131-8.

17. Wan, Y. F.; Goubet, N.; Albouy, P. A.; Pileni, M. P., Hierarchy in Au nanocrystal ordering in supracrystals: a potential approach to detect new physical properties. *Langmuir* **2013,** *29* (24), 7456-63.

18. Baranov, D.; Fiore, A.; van Huis, M.; Giannini, C.; Falqui, A.; Lafont, U.; Zandbergen, H.; Zanella, M.; Cingolani, R.; Manna, L., Assembly of colloidal semiconductor nanorods in solution by depletion attraction. *Nano Lett* **2010,** *10* (2), 743-9.

19. Shevchenko, E. V.; Talapin, D. V.; Kotov, N. A.; O'Brien, S.; Murray, C. B., Structural diversity in binary nanoparticle superlattices. *Nature* **2006,** *439* (7072), 55-9.

20. Kalsin, A. M.; Fialkowski, M.; Paszewski, M.; Smoukov, S. K.; Bishop, K. J.; Grzybowski, B. A., Electrostatic self-assembly of binary nanoparticle crystals with a diamond-like lattice. *Science* **2006,** *312* (5772), 420-4.

21. Kostiainen, M. A.; Hiekkataipale, P.; Laiho, A.; Lemieux, V.; Seitsonen, J.; Ruokolainen, J.; Ceci, P., Electrostatic assembly of binary nanoparticle superlattices using protein cages. *Nat Nanotechnol* **2013,** *8* (1), 52-6.

22. Wheeler, R., Wikimedia Commons. **2011**.

23. Seeman, N. C., Nucleic acid junctions and lattices. *J Theor Biol* **1982,** *99* (2), 237-47.

24. Peng, S. M., Derrien, T.L., Cui, J., Xu, C.Y., Luo, D., From cells to DNA materials. *Materials Today* **2012,** *15* (5), 190-194.

25. Yang, D.; Hartman, M. R.; Derrien, T. L.; Hamada, S.; An, D.; Yancey, K. G.; Cheng, R.; Ma, M.; Luo, D., DNA materials: bridging nanotechnology and biotechnology. *Acc Chem Res* **2014,** *47* (6), 1902-11.

26. Kuhler, P.; Roller, E. M.; Schreiber, R.; Liedl, T.; Lohmuller, T.; Feldmann, J., Plasmonic DNA-origami nanoantennas for surface-enhanced Raman spectroscopy. *Nano Lett* **2014,** *14* (5), 2914-9.

27. Kuzyk, A.; Schreiber, R.; Zhang, H.; Govorov, A. O.; Liedl, T.; Liu, N., Reconfigurable 3D plasmonic metamolecules. *Nat Mater* **2014,** *13* (9), 862-6.

28. Sharma, J.; Chhabra, R.; Cheng, A.; Brownell, J.; Liu, Y.; Yan, H., Control of self-assembly of DNA tubules through integration of gold nanoparticles. *Science* **2009,** *323* (5910), 112-6.

29. Mirkin, C. A.; Letsinger, R. L.; Mucic, R. C.; Storhoff, J. J., A DNA-based method for rationally assembling nanoparticles into macroscopic materials. *Nature* **1996,** *382* (6592), 607-9.

30. Park, S. Y.; Lytton-Jean, A. K.; Lee, B.; Weigand, S.; Schatz, G. C.; Mirkin, C. A., DNA-programmable nanoparticle crystallization. *Nature* **2008,** *451* (7178), 553-6.

31. Nykypanchuk, D.; Maye, M. M.; van der Lelie, D.; Gang, O., DNA-guided crystallization of colloidal nanoparticles. *Nature* **2008,** *451* (7178), 549-52.

32. Cheng, W.; Hartman, M. R.; Smilgies, D. M.; Long, R.; Campolongo, M. J.; Li, R.; Sekar, K.; Hui, C. Y.; Luo, D., Probing in real time the soft crystallization of DNA-capped nanoparticles. *Angew Chem Int Ed Engl* **2010,** *49* (2), 380-4.

33. Macfarlane, R. J.; Lee, B.; Jones, M. R.; Harris, N.; Schatz, G. C.; Mirkin, C. A., Nanoparticle superlattice engineering with DNA. *Science* **2011,** *334* (6053), 204-8.

34. Macfarlane, R. J.; Jones, M. R.; Lee, B.; Auyeung, E.; Mirkin, C. A., Topotactic interconversion of nanoparticle superlattices. *Science* **2013,** *341* (6151), 1222-5.

35. Jones, M. R.; Macfarlane, R. J.; Lee, B.; Zhang, J.; Young, K. L.; Senesi, A. J.; Mirkin, C. A., DNA-nanoparticle superlattices formed from anisotropic building blocks. *Nat Mater* **2010,** *9* (11), 913-7.

36. Zhang, Y.; Lu, F.; Yager, K. G.; van der Lelie, D.; Gang, O., A general strategy for the DNA-mediated self-assembly of functional nanoparticles into heterogeneous systems. *Nat Nanotechnol* **2013,** *8* (11), 865-72.

37. Vo, T.; Venkatasubramanian, V.; Kumar, S.; Srinivasan, B.; Pal, S.; Zhang, Y.; Gang, O., Stoichiometric control of DNA-grafted colloid self-assembly. *Proc Natl Acad Sci U S A* **2015,** *112* (16), 4982-7.

38. Tan, S. J.; Kahn, J. S.; Derrien, T. L.; Campolongo, M. J.; Zhao, M.; Smilgies, D. M.; Luo, D., Crystallization of DNA-capped gold nanoparticles in high-concentration, divalent salt environments. *Angew Chem Int Ed Engl* **2014,** *53* (5), 1316-9.

39. Campolongo, M. J.; Tan, S. J.; Smilgies, D. M.; Zhao, M.; Chen, Y.; Xhangolli, I.; Cheng, W.; Luo, D., Crystalline Gibbs monolayers of DNA-capped nanoparticles at the air-liquid interface. *ACS Nano* **2011,** *5* (10), 7978-85.

CHAPTER TWO:

DYNAMICS OF DNA-CAPPED GOLD NANOPARTICLE ASORPTION AT THE SILICON-WATER INTERFACE

2.1: BACKGROUND

The controlled assembly of nanoscale building blocks into highly ordered mesostructures has resulted in a new generation of nanodevices with novel optical, electronic and magnetic properties, with applications ranging from data storage[1] to biosensing[2-3]. In particular, the assembly of colloidal nanocrystals into long-range ordered superstructures has generated strong interest, due to the rich phenomena that are the result of the collective oscillations of the nanocrystals[4]. One such system employing DNA as a designer ligand to mediate the assembly of nanoparticles has achieved remarkable success in rationally designing and building such "artificial solids[5]." While the processes controlling the assembly of such systems in solution is well characterized[6], a detailed understanding of the solution phase processes controlling their ability to self-assemble on silicon substrates is not well understood. In order to ensure the development of such technologies, it is imperative that these nanoscale building blocks can be readily integrated into the ubiquitous photolithography processes of silicon.

Recently our group reported the ability to control the crystallization of DNA-AuNPs at the air-water interface by controlling the salt species and ionic strength of aqueous solutions[7]. While the findings extended 2D nanoparticle crystallization to conditions relevant to real world sensing and diagnostic applications as well as presented a semi-empirical model to predict the behavior of the DNA brush, the applicability of air-water interface crystallization is limited. Extending these phenomena to the liquid-solid interface as well as dry state can enable the novel properties of nanoparticle assemblies to be incorporated into nanofabricated devices, merging top-down and bottom up processes.

Adsorption of nanoparticles at the solid interface is a well-characterized process[8]. However, to the best of our knowledge, a comprehensive study of the adsorption of DNA-AuNPs on silicon surfaces has not been undertaken. In order to characterize and elucidate the processes controlling the adsorption of DNA- AuNPs on Si we undertook a comprehensive study of DNA-AuNPs on variously functionalized surfaces using a combination QCM-D and SAXS. Specifically we investigated the dynamics of DNA-AuNPs in solutions of various ionic strengths, monitoring the kinetics of adsorption using QCM-D and characterized the adsorbed layer using GISAXS. This chapter describes the study of the kinetics of AuNP adsorption using QCM-D and the development of a kinetic model describing the adsorption processes.

2.2 MATERIALS AND METHODS

2.2.1 Synthesis of DNA-capped Gold Nanoparticles

15 nm diameter gold nanoparticles (AuNPs) used in these experiments were purchased from Ted Pella. The oligonucleotides used were ordered conjugated with a 5' thiol group from Integrated DNA Technologies. Prior to attachment of the oligonucleotides to the AuNPs, the thiol group was first deprotected with tris(2-carboxyethyl)phosphine hydrochloride (TCEP) by incubating the oligonucleotides at a 1:5 (DNA:TCEP) ratio for 30 minutes. The oligonucleotides were then added to the AuNPs at a DNA:AuNP ratio of 1200:1 to ensure maximum surface coverage, then shaken overnight at 500 rpm at room temperature after which NaCl was slowly added over a period of 8 hours to a final concentration of 750 mM, reducing DNA-DNA repulsion and further increasing the DNA coverage. The nanoparticles were then purified of salt and excess DNA by several centrifugation cycles in pure water. Three different non-basing pairing single stranded sequences were used for the QCM studies, each comprising 10, 30, or 60

thymine bases, hereafter referred to as T10, T30, and T60, respectively. A base pairing sequence was also tested, composed of 30 thymine bases followed by an 8 base palindromic "sticky end", referred to as T30p. The palindromic sticky end employed was eight bases long, with a sequence of CTCATGAG.

2.2.2 Quartz Crystal Microbalance with Dissipation Studies

The QCM system used was a QSense QCM-D E1 system (Biolin Scientific) located at the Cornell High Energy Synchrotron Source (CHESS). All measurement were conducted using the proprietary Qsense software QSoft 401. QSense QCM-D sensors, with a 50 nm silicon coating were purchased from Biolin Scientific.The frequency traces recorded in these studies were then converted to ng/cm^2 using the Saurbrey model in the Qsense Qtools data analysis software. The Sauerbrey model (Equation 2.1) is a simple formula that relates the change in the fundamental resonance frequencies of the silicon substrate to the adsorbed mass on the silicon:

$$\Delta m = -\frac{C\Delta f}{n} \qquad \text{Equation 2.1}$$

where, Δm is the change in adsorbed mass, Δf, is the change in frequency, n, is the overtone number and, C, is a constant specific to the substrate, which for silicon is 17.7 ng cm^{-2} s^{-1}. For soft films the viscoelastic model must be used which also takes into account the dissipation changes of the vibrations, however, as the DNA-AuNPs adsorb in a monolayer, the Sauerbrey model holds, further confirmed by the lack of significant dissipation changes.

In order to maximize the DNA-AuNP loading on the silicon surfaces studied, a positively charged silane, 3-aminopropyl triethoxysilane (APTES), was functionalized on the silicon surface to attract the negatively charged DNA-AuNPs. This was achieved by first incubating the QCM sensor in a 2% APTES solution in 95% ethanol overnight. After rinsing in pure ethanol

followed by a rinsing in isopropanol, the sensor was baked at 95 °C for 1 hour followed by another rinsing cycle.

In order to obtain measurements with minimal noise, dry sensors were allowed to incubate on the instrument for ca. 10 minutes. Following equilibration of the dry sensors (no visible natural frequency change over ca. 60 s) a drop of approximately 200 μL of the appropriate ionic strength was covered and allowed to equilibrate over approximately 15 minutes. Once the sensor was deemed equilibrated a stock solution of nanoparticles was added to a final nanoparticle concentraion of ~5 nM. QCM-D traces were allowed to proceed until no further frequency changes were detectable. Samples were tested at ionic strengths of 0, 13, 66, 133, and 266 mM in NaCl as well as up to 1000 mM in $MgCl_2$.

2.2.3 Kinetic Modeling

All fits to the kinetic traces obtain by QCM were performed in MATLAB using the curve fitting tool.

2.2.4 Grazing Incidence Small Angle X-ray Scattering Experiments

Grazing incidence small angle X-ray scattering experiments (GISAXS) were performed at the D1 experimental station at the Cornell High Energy Synchrotron Source (CHESS). An incident X-ray beam with a flux of $\sim 10^{12}$ photons s^{-1} mm^{-1} was used with a bandwidth of 1.5% achieved using a multilayer monochromator. The dimensions of the collimated X-ray beam were 0.3 mm (horizontal) and 0.2 mm (vertical). During these experiments a MedOptics CCD detector with a pixel size of 46.9 x 46.9 microns was used, with a sample-to-detector distance of 1873 mm, a wavelength of 1.26 Å, and an incident angle of 0.25°.

Kinetic scattering spectra were collected by placing a ca. 5 μL of DNA-AuNPs in salt solution on a cleaned, freshly APTES functionalozed Si substrate. In order to avoid drying

effects, the substrate was placed in a sealed sample environment chamber with a reservoir of equal salt concentration. The concentration of the nanoparticles in the droplet was approximately 0.05 nM, which is ~100 fold more dilute than the samples used for the QCM-D experiments. This concentration was chosen to minimize scattering from the bulk solution and to maximize scattering from surface adsorbed nanoparticles. To avoid DNA damage from the incident X-ray beam[9], spectra were taken every 2 minutes at different locations on the droplet, with the same location being illuminated every 10 minutes.

2.3 RESULTS

2.3.1 Adsorption Kinetics

In order to understand the dynamics of DNA-AuNP adsorption on silicon, a broad range of parameters were explored. Specifically, 1) ionic strength, in both monovalent (NaCl) and divalent ($MgCl_2$) salts, 2) DNA ligand length, and 3) DNA complementarity were investigated using QCM-D. Example kinetic traces from two of the non-base pairing ligands tested are shown in Figure 2. 1.

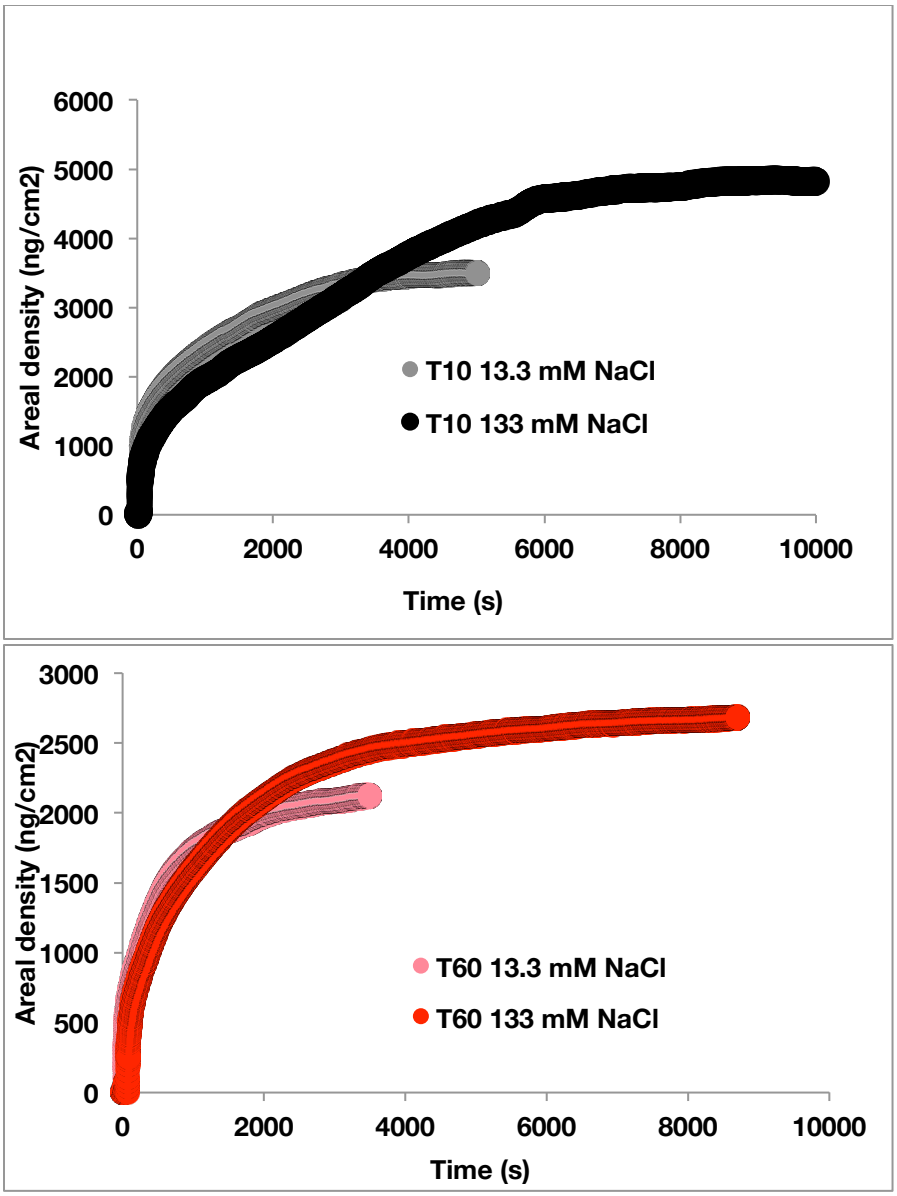

Figure 2. 1: QCM adsorption profiles of DNA-AuNPs functionalized with two ligand lengths at various NaCl ionic strengths. (Top) T10 DNA-AuNPs at (grey) 13 mM NaCl and (black) 133 mM NaCl as well as (bottom) T60 DNA-AuNPs at both (dark red) 13 mM and (light red) 133 mM. Two trends are readily visible 1) the time to reach maximum adsorption is longer for higher ionic strengths and 2) shorter ligands allow a higher mass of nanoparticle adsorption.

From the data, it can be seen that increasing the ionic strength has the effect of increasing the saturation coverage of the nanoparticles on the surface. While more nanoparticles were adsorbed at higher ionic strengths, the kinetics of this adsorption was slower- it took notably longer to reach saturation coverage at increased ionic strengths. The saturation coverage between the non-base pairing nanoparticles as a function of ionic strength can be seen in Figure 2. 2.

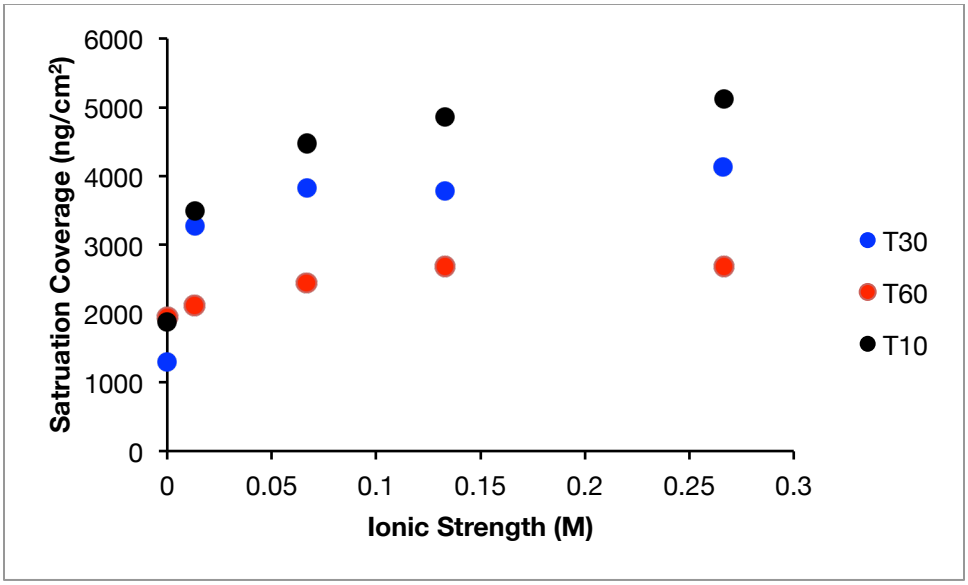

Figure 2. 2: Saturation coverage as a function of NaCl ionic strength for the three DNA-AuNPs tested. The plot shows that surface coverage is increased by both shortening ligand lengths, as seen by the higher surface coverage for shorter ligands, as well as by higher ionic strengths.

Again it can be seen that higher ionic strength resulted in higher saturation coverage. It can also be seen that increasing the ligand length results in a lower surface coverage. This is not surprising, as longer ligands will occupy more surface area on the silicon surface, thereby reducing the total number of nanoparticles adsorbed. The effect of increased particle coverage by shorter ligands also served to slow the adsorption kinetics. This is analogous to the ionic strength trend, where at higher ionic strenght more nanoparticles are adsorbed but this also serves to slow the kinetics.

In previous studies, our group used $MgCl_2$ to control the air-water interfacial assembly of non-base paring DNA-AuNPs. It was shown that DNA-AuNPs in $MgCl_2$ experienced larger DNA compression than in NaCl solutions of equivalent ionic strength, allowing nanoparticles to pack closer together[7]. Here, this same effect is explored at the solid-liquid interface. Comparing the saturation adsorption of T30 DNA-AuNPs, the same trend is again seen (Figure 2. 3). For equivalent ionic strengths, $MgCl_2$ solutions enable higher surface accumulation. The same reasoning applied to the air-water interface can be invoked here- higher DNA compression allows DNA-AuNPs to pack closer together. This higher surface accumulation enabled by $MgCl_2$ was coupled with a notable increase in adsorption kinetics. This effect is illustrated in the kinetic traces shown in Figure 2. 4. Here it can be seen that at equivalent ionic strengths, $MgCl_2$ solutions experience markedly faster kinetics in both the early and later adsorption regimes.

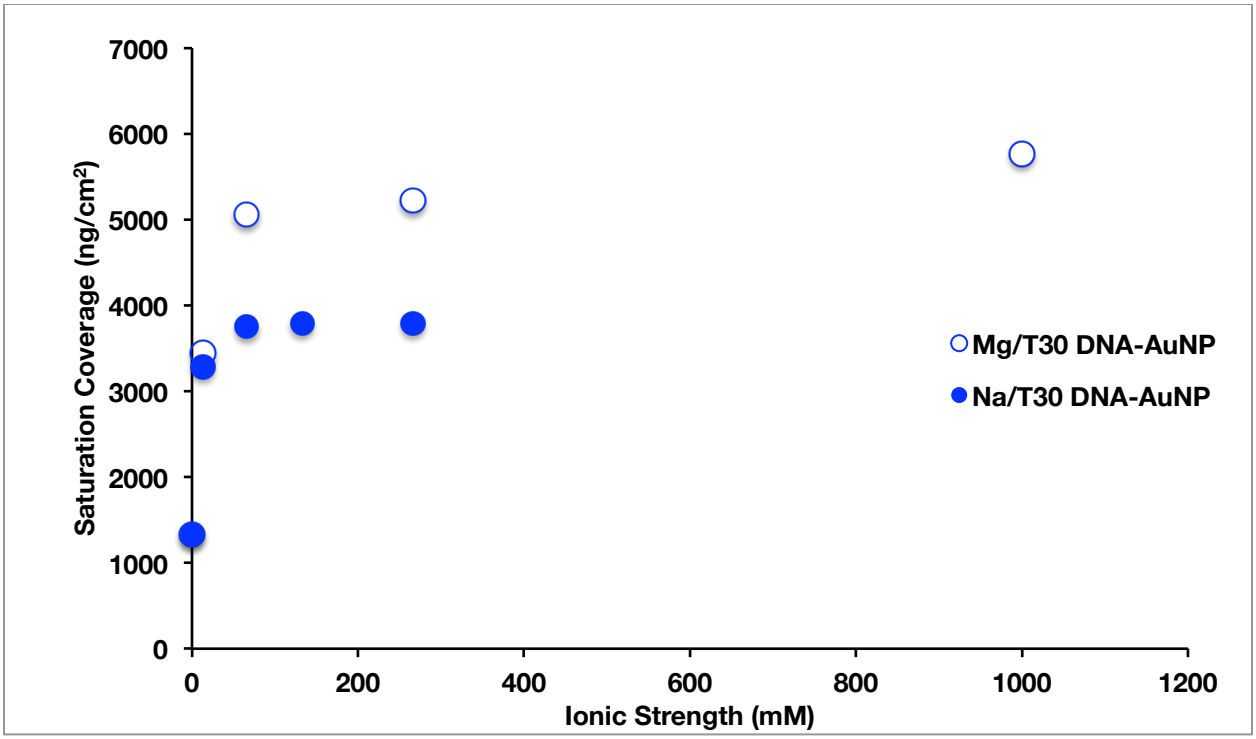

Figure 2. 3: Saturation coverage at various ionic strengths in both NaCl (filled circles) and $MgCl_2$ (hollow circles) for T30 DNA-AuNPs. It can clearly be seen that $MgCl_2$ solutions of equivalent ionic strengths result in greater nanoparticle adsorption.

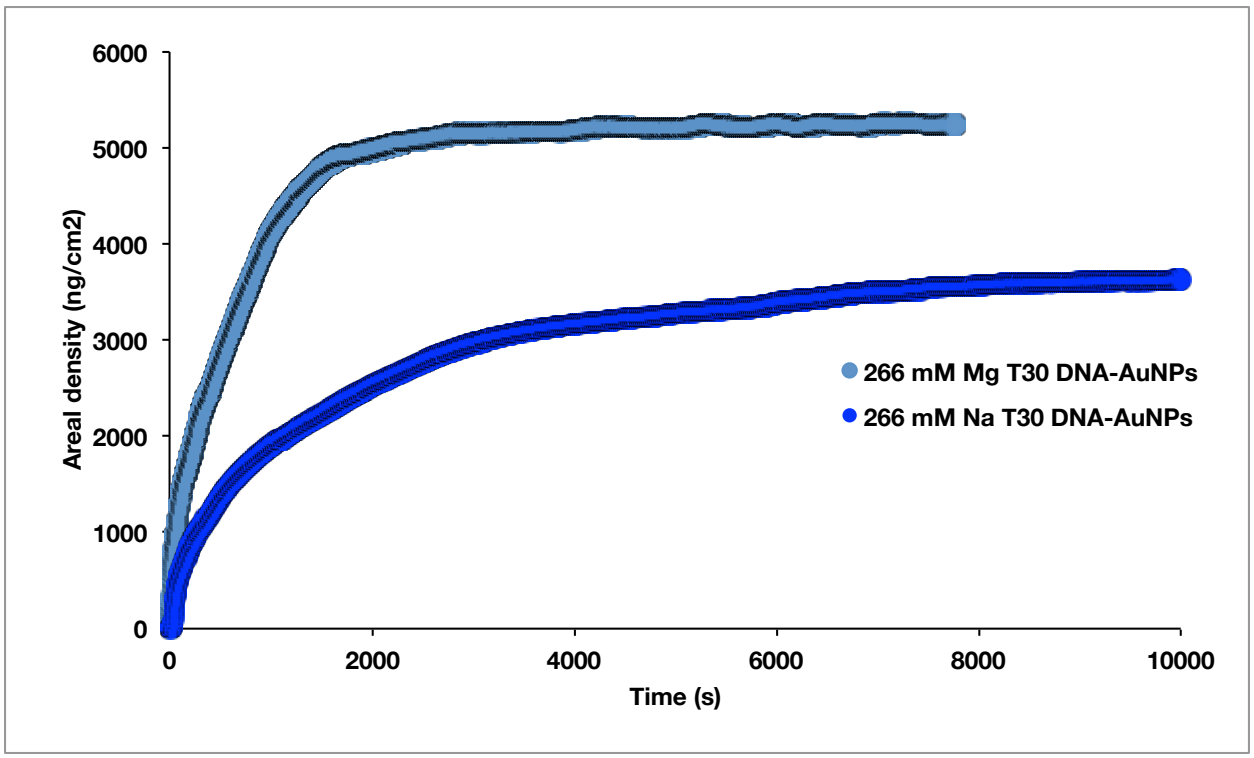

Figure 2. 4: Kinetic traces for T30 DNA-AuNPs at 266 mM ionic strength for both (light blue) $MgCl_2$ and (dark blue) NaCl. The traces demonstrate the slower kinetics of adsorption for NaCl solutions.

The above data have shown that ionic strength, ligand length, and electrolyte species can be used to control the surface density of DNA-AuNPs. Another important consideration in the assembly of DNA-AuNPs is the nature of the DNA itself, that is, the specific sequence used. Typically, DNA-AuNPs are assembled using DNA oligomers that promote base pairing between neighboring particles. By comparing two DNA ligands of the same length, one with palindromic "sticky ends", allowing hybridization with neighboring nanoparticles, and the non-base pairing sequences used above, it is possible to directly compare how DNA-DNA base pairing interactions affect the kinetics and magnitude of assembly at the solid-liquid interface. This was done by incorporating a self-hybridizing (palindromic) DNA sequence to the 30 base thymine

oligomer. Comparison of the hybridizing (T30p) and non-hybridizing (T30) sequences can be seen in Figure 2. 5. Though it may be surmised that promoting binding between neighboring nanoparticles may increase the silicon surface accumulation, the opposite result was obtained. Upon inspection of figure 2.5 it can be clearly seen that a greater nanoparticle surface density is obtained using non-base pairing DNA-AuNPs than with DNA-AuNPs with palindromic "sticky ends".. Here we see that T30 DNA-AuNPs consistently recorded a higher surface density among all the NaCl ionic strengths tested. This is presumably due to the increase in length of the ligand upon addition of the base pairing region.

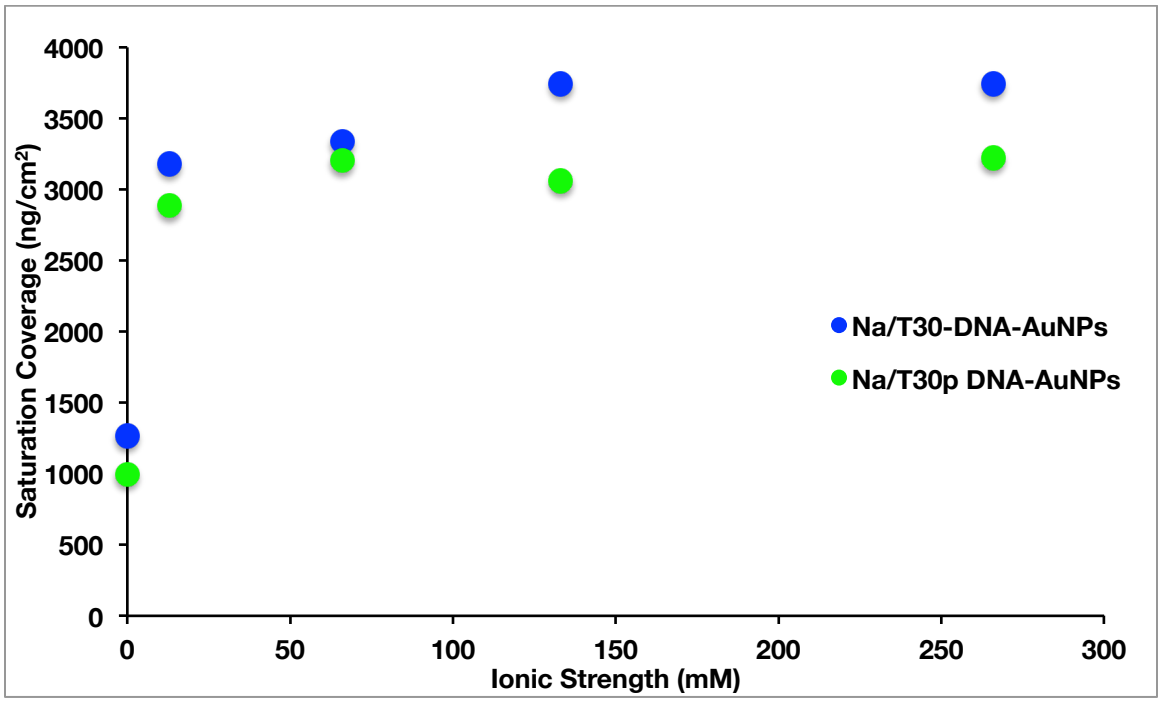

Figure 2. 5: Comparison of base pairing (green) and non-base (blue) pairing ligands saturation coverage in NaCl. The lower saturation coverage of the base pairing nanoparticles is attributed to the additional length resulting from the addition of a base pairing region.

This difference, however, is erased in $MgCl_2$ solutions. As shown in Figure 2. 6, the saturation coverage between the base pairing and non-base pairing ligands is roughly equivalent.

This implies that $MgCl_2$ effectively increases the packing of nanoparticles to a greater degree for base-pairing ligands as compared to non-base pairing ligands. Considering the lower compressibility of dsDNA, this finding is surprising. The reason for this unequal increase remains unclear.

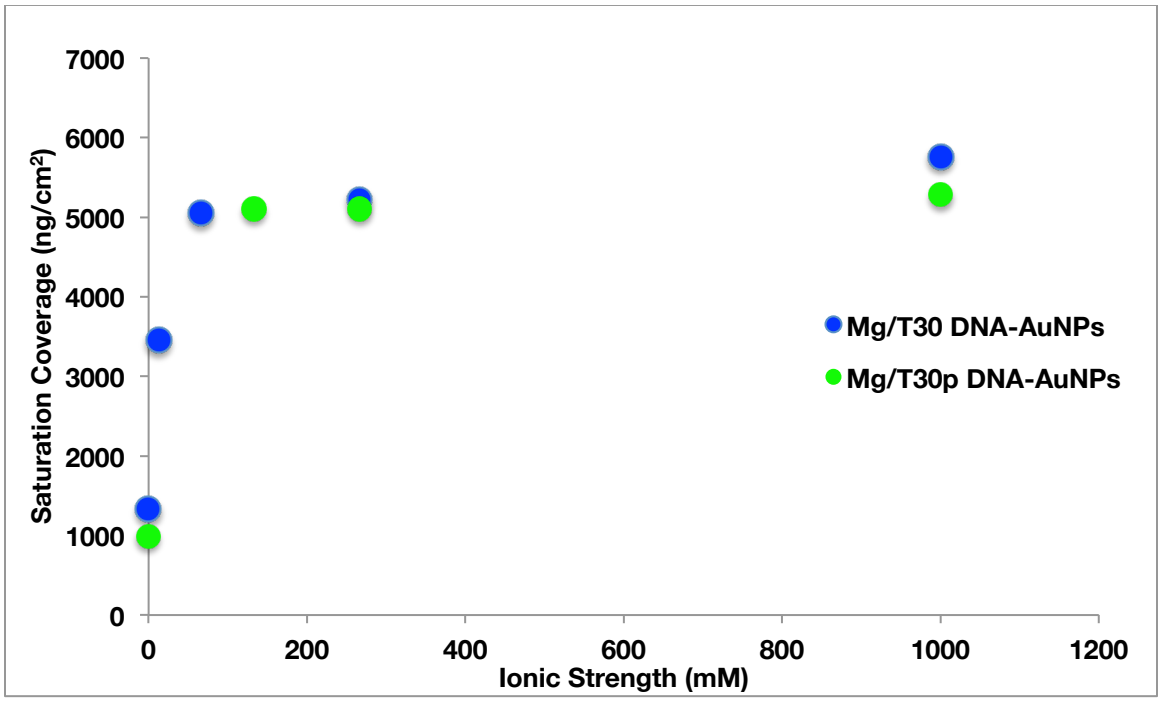

Figure 2. 6: Comparison of base pairing (green) and non-base (blue) pairing ligands saturation coverage in $MgCl_2$. The difference in total adsorption seen in **Figure 2. 5** is eliminated in the $MgCl_2$ solutions, despite the longer ligand length and presence of a dsDNA base pairing region.

2.3.2 Modeling Kinetic Behavior

In order to gain insight into the processes governing the dynamics of adsorption a kinetic model for the nanoparticle adsorption was developed. As a starting point, a simple Langmuir adsorption model was fit. However, this rudimentary model failed to capture the dynamics of adsorption. Despite the inability of this model to capture the complete kinetics of adsorption, the

later time points could be reasonably captured by using the x-intercept as a fitting parameter (Figure 2. 7). As seen in the plots this model clearly failed to fit the early and intermediate time points, while describing the saturation points accurately, suggesting that perhaps more than one process was occurring during adsorption. For this reason, a dual phase Langmuir model was adopted. This model is simply a sum of two separate Langmuir processes each with individual time constants. The data acquired was fit to equation 2.2,

$$\Gamma_t = \Gamma_1\left(1 - e^{-\frac{t}{\tau_1}}\right) + \Gamma_2\left(1 - e^{-\frac{t}{\tau_2}}\right) \qquad \text{Equation 2.2}$$

where Γ_t, is the total adsorption, Γ_1, and Γ_2 are the maximum adsorptions at which the two processes act, and τ_1, and τ_2, are the time constants of these processes. These same four parameters were used to fit the QCM data. A comparison of the two phase model with the x-intercept fitting model is shown in Figure 2. 7. Here it can be seen that best overall fit is indeed achieved by the dual phase model, shown by the red dashed line, as opposed to the x-intercept fitting model, which will accurately capture the behavior of the later time points but shows high deviation in the early and intermediate time scales. The fitting residuals, shown at the bottom of Figure 2. 7 further confirm this trend. It can be seen that the magnitude of the residuals is far smaller for the dual fit model in the early and intermediate time points, confirming the more accurate fit.

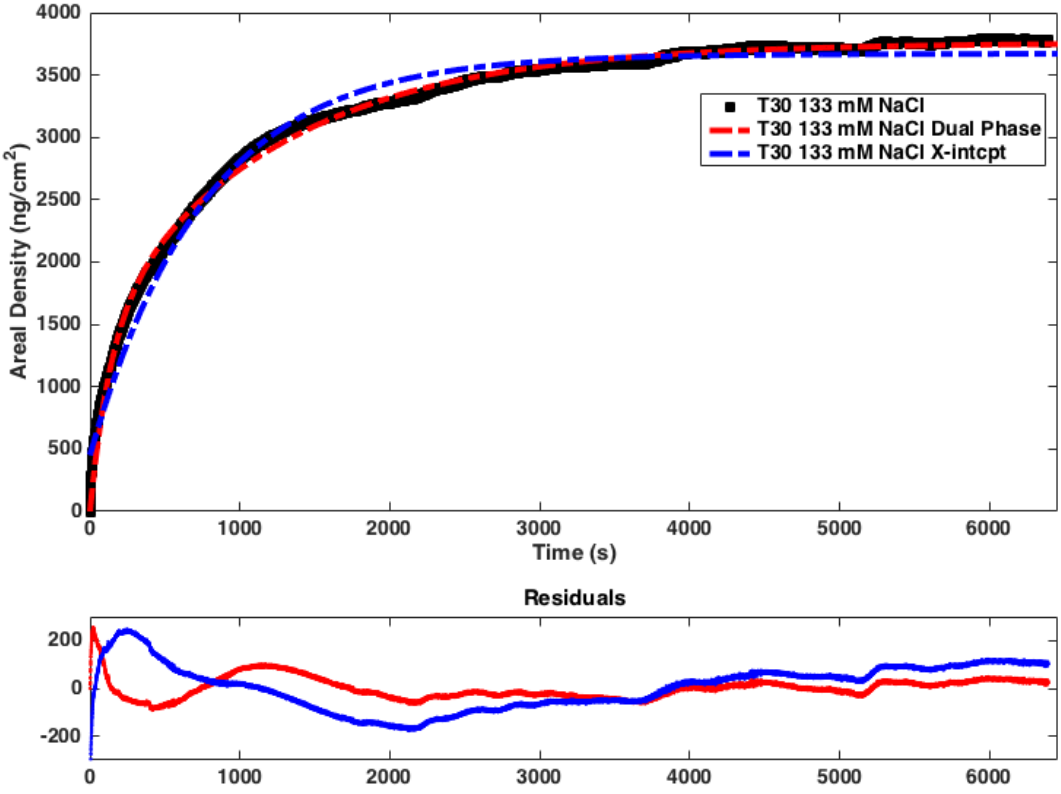

Figure 2. 7: T30 DNA-AuNP (black trace) kinetic trace obtained at 133 mM NaCl, (red dashed trace) fit of the dual phase modeled described by equation 2.2, and (blue dashed trace) a fit with a Langmuir model using the x-intercept as a fitting parameter. The best fit is obtained using the dual-phase model. The lower plot shows the fit residuals.

In order to extract kinetic parameters from the fitting of the dual phase model, the kinetic parameters, specifically the time constants, τ_1 and τ_2, were plotted as a function of NaCl ionic strength (Figure 2. 8). The time constants are related to the kinetics of the two processes of the dual phase model, with larger values indicating slower adsorption kinetics. The fitting results indicated two distinct regimes for the time constants, one smaller value (where $\tau_1 < 150$s) describing the faster, initial adsorption process, and one large value (where $\tau_2 > 150$s) which

describes the slower, later adsorption process. The fitting results summarized in Figure 2. 8, while exhibiting slight variation, show the clear slowing of kinetics at higher ionic strengths, as ionic strength increases, so do the time constants. This increase, however, is non-monotonic in both the T30 and T60 DNA-AuNPs, but monotonic for the T10 DNA-AuNPs.

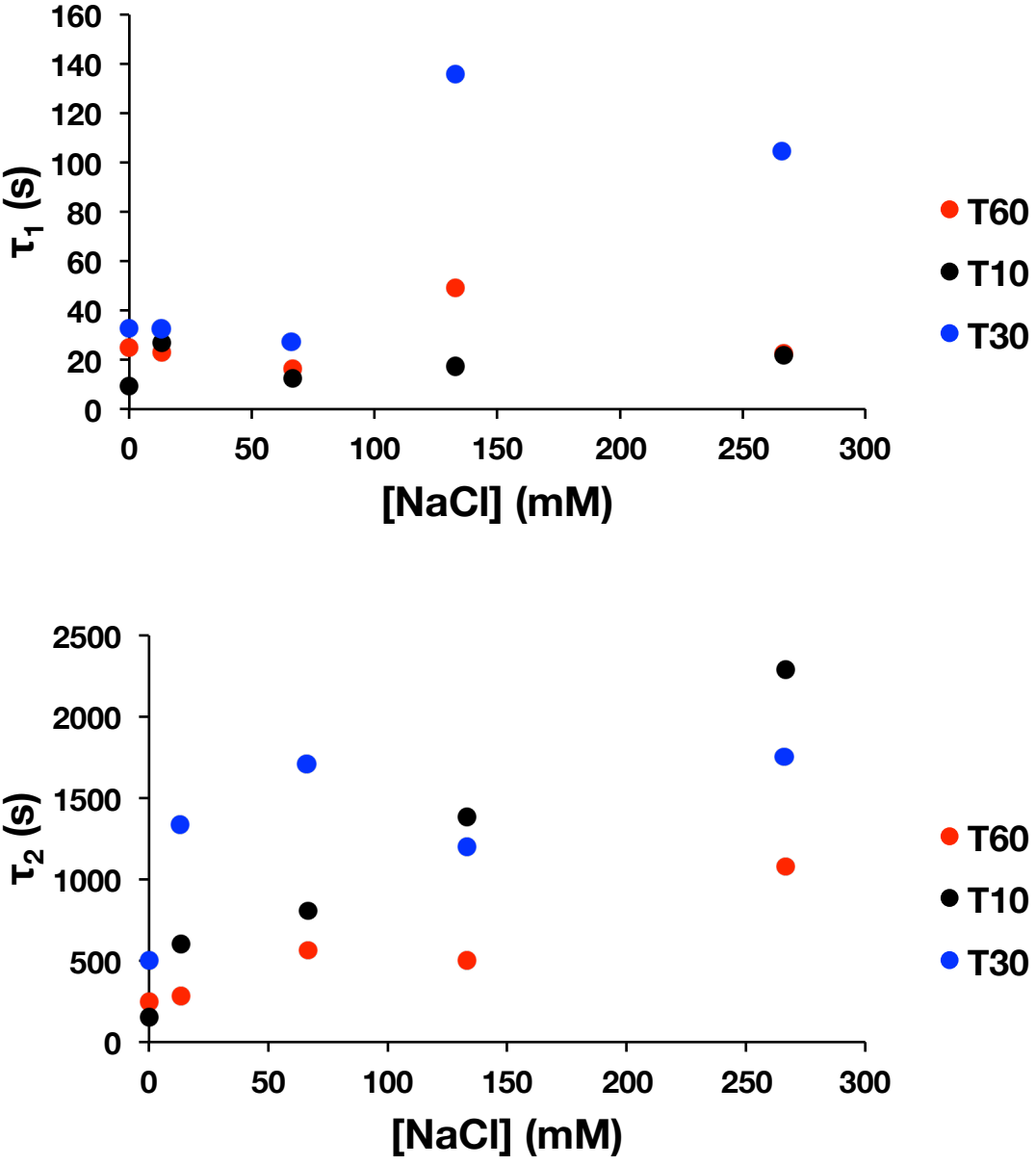

Figure 2. 8: Time constants, τ_1 (top) and τ_2 (bottom), fit from the dual-phase model at varying NaCl ionic strengths, for non-base pairing DNA-AuNPs with T10, T30, and T60 ligands. The general trend that can be seen shows that the time constants tend to increase in magnitude, indicating slower adsorption processes, though the increase is not monotonic.

In contrast to the non-base pairing nanoparticles, the addition of a base-pairing moiety seemed to have the opposite effects on adsorption kinetics. At higher ionic strengths, the magnitude of the slow time constant, τ_2, decreased indicating a faster adsorption process (Figure 2. 9). This contrasting behavior, with the addition of base pairing, can be attributed to the screening effects of the Na^+ counterion, which facilitates interparticle base pairing, effectively increasing interparticle attractions.[10] No clear trend was seen for τ_1, thus perhaps other models, which will be discussed below, may also be considered.

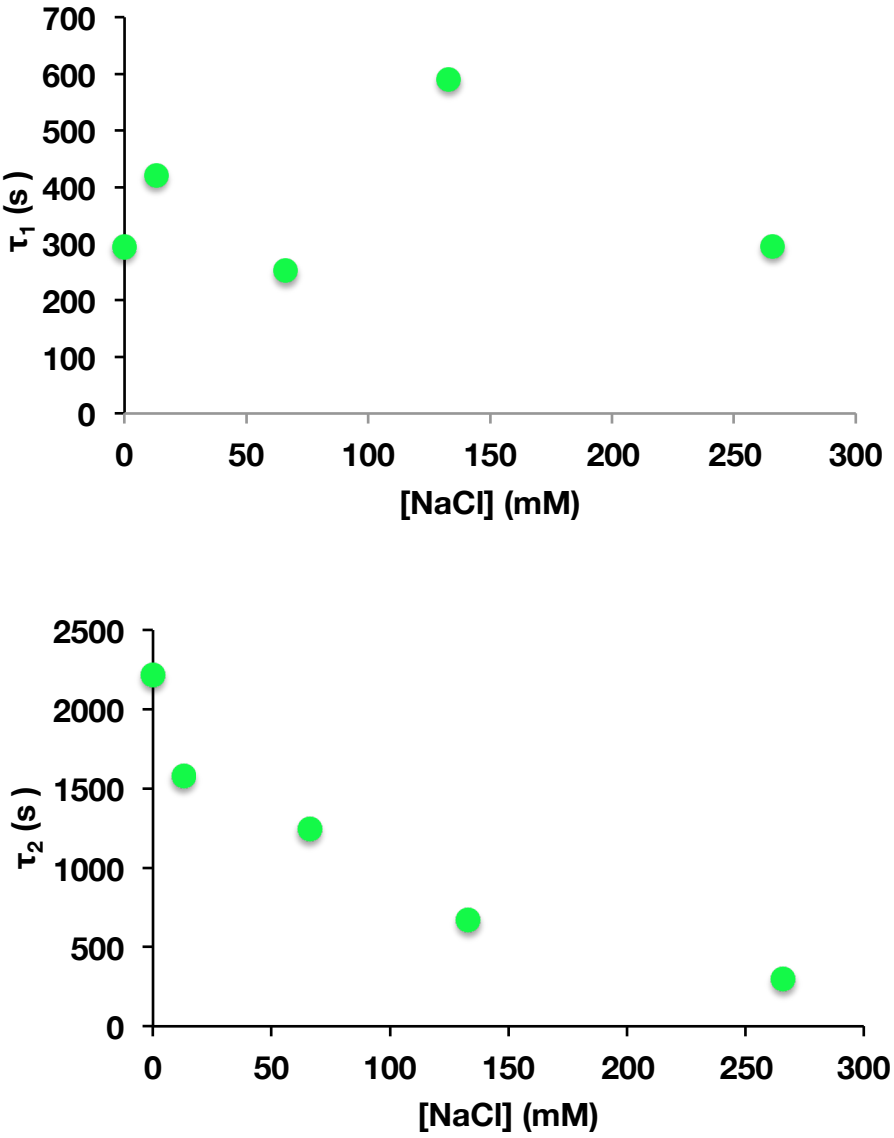

Figure 2. 9: Time constants, τ_1 (top) and τ_2 (bottom), fit from the dual-phase model at varying NaCl ionic strengths for the base pairing T30p DNA-AuNPs. No discernible trend was observed for the time constant, τ_1 , however, the time constant for the secondary, slow process, τ_2, can be seen to decrease in magnitude with increasing ionic strength, indicating a faster adsorption. This can be attributed to the facilitation of hybridization by salt screening.

Kinetic traces were also obtained for the T30 and T30p DNA-AuNPs in $MgCl_2$ solutions of equivalent ionic strengths to those tested in NaCl. In these cases the dual phase model again accurately captured the kinetic behavior. Despite the strong fit, no clear trends were evident for the time constants, τ_1 and τ_2. Another model that can be suggested to modify exponential behaviors such as Langmuir adsorption is a stretched exponential. Also known as a Kohlrausch-William-Watts (KWW) function, the stretched exponential introduces a power law into the exponential function, in this case the Langmuir adsorption model (equation 2.3).

$$\Gamma_t = \Gamma_{max}\left[1 - e^{-\left(\frac{t}{\tau}\right)^{\beta}}\right] \qquad \text{Equation 2.3}$$

Where Γ_t, is the adsorption at time t, Γ_{max}, is the maximum adsorption, and τ is a time constant. In a KWW function the exponential, β, describes a distribution of time constants, with values closer to 0 describing a broad distribution and a value of 1 corresponding to a single time constant for the system.

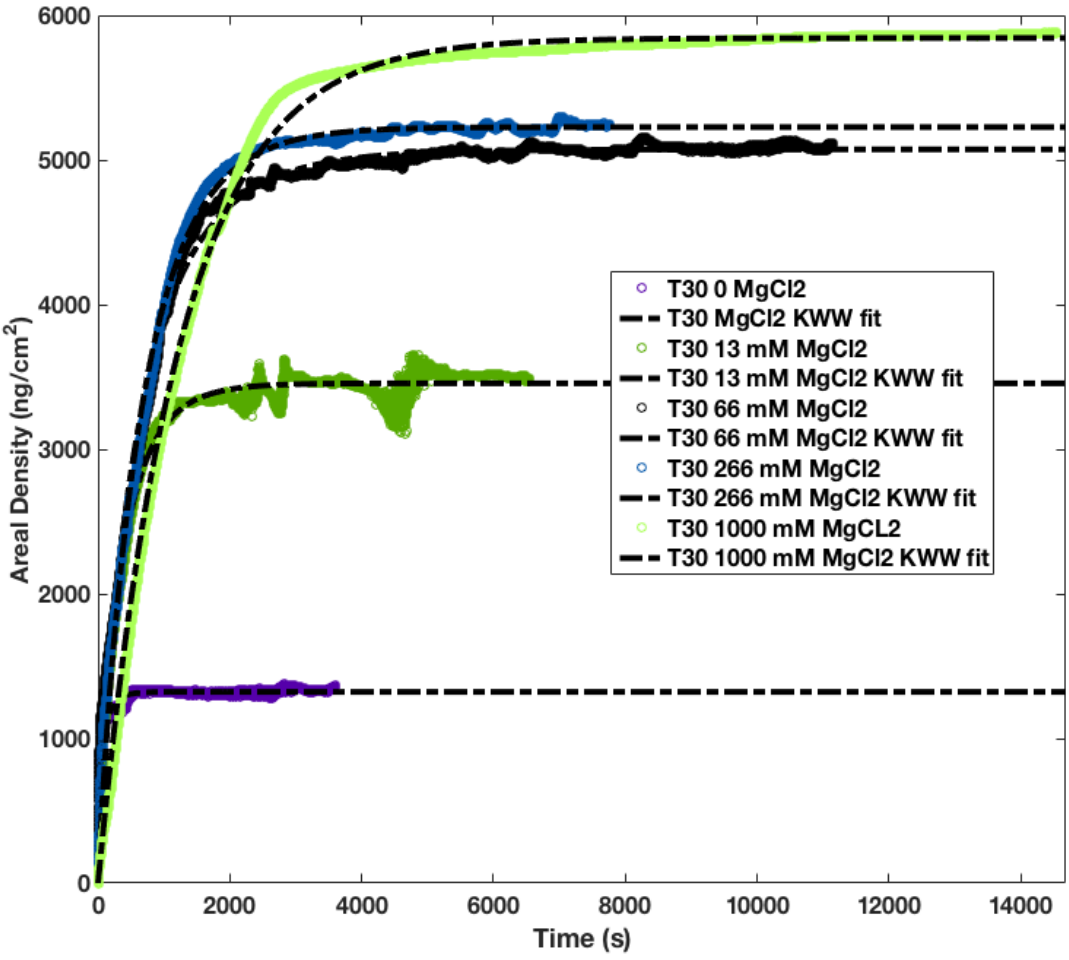

Figure 2. 10: QCM-D traces obtained for non-base pairing T30 DNA-AuNPs in solutions of various $MgCl_2$ ionic strengths, shown by the solid traces, and fits to a KWW kinetic model shown by the black, dashed traces.

For the non base-pairing, T30 DNA-AuNPs in NaCl, the dual phase model provided the best fit to the experimental data, however when kinetic traces obtained in $MgCl_2$ were fit, no clear trends for the four fitting parameters were apparent. On the other hand, when fit to a KWW function, clear, noteworthy trends emerged. Firstly, the time constant, τ, increased in magnitude at higher $MgCl_2$ ionic strengths, indicating slower adsorption kinetics (Figure 2. 11- top). Most

striking was the trend of the stretched exponential parameter, β, to converge towards unity for higher ionic strengths (Figure 2. 11- bottom). This noteworthy convergence indicates that at higher ionic strengths of $MgCl_2$, the adsorption follows the simple, single process Langmuir adsorption isotherm.

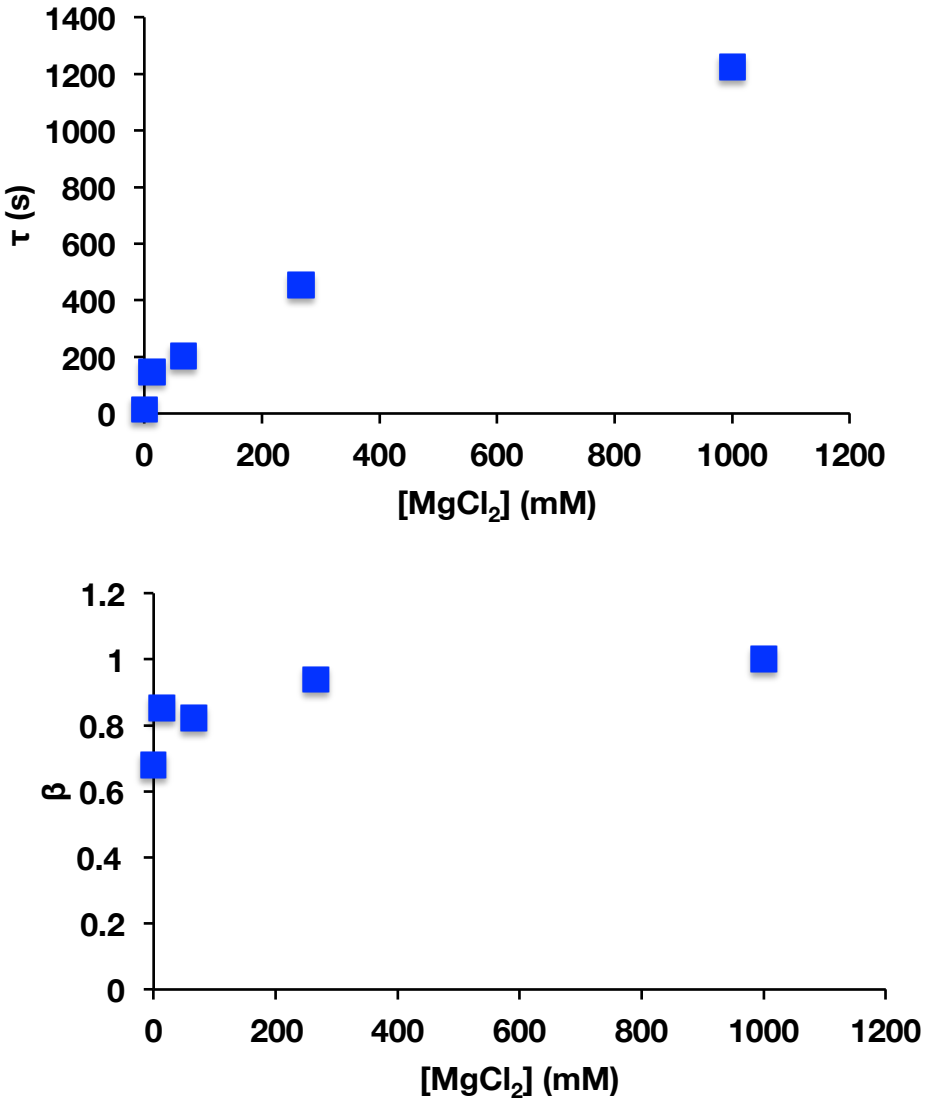

Figure 2. 11: Fit parameters for the adsorption kinetics of non-base pairing T30 DNA AuNPs in $MgCl_2$ solutions. The increase in magnitude of the time constant, τ (top), indicates slower kinetics at higher ionic strengths; the convergence of the stretched exponential, β (bottom), suggests that with increasing ionic strengths the adsorption kinetics follow simple Langmuir adsorption kinetics. All salt concentrations are listed as ionic strength.

An equivalent tendency was noted with the base pairing, T30p DNA-AuNPs in $MgCl_2$ solutions. Strikingly, the convergence to the simple Langmuir model, that is to a β value of unity, occurred in the lowest $MgCl_2$ ionic strength tested, at 133 mM, half the value as for the non-base pairing nanoparticles (Figure 2. 12). Although the kinetics were once again slowed with increasing ionic strength, the amount of nanoparticles adsorbed, Γ_{max}, reached saturation at 133 mM ionic strength.

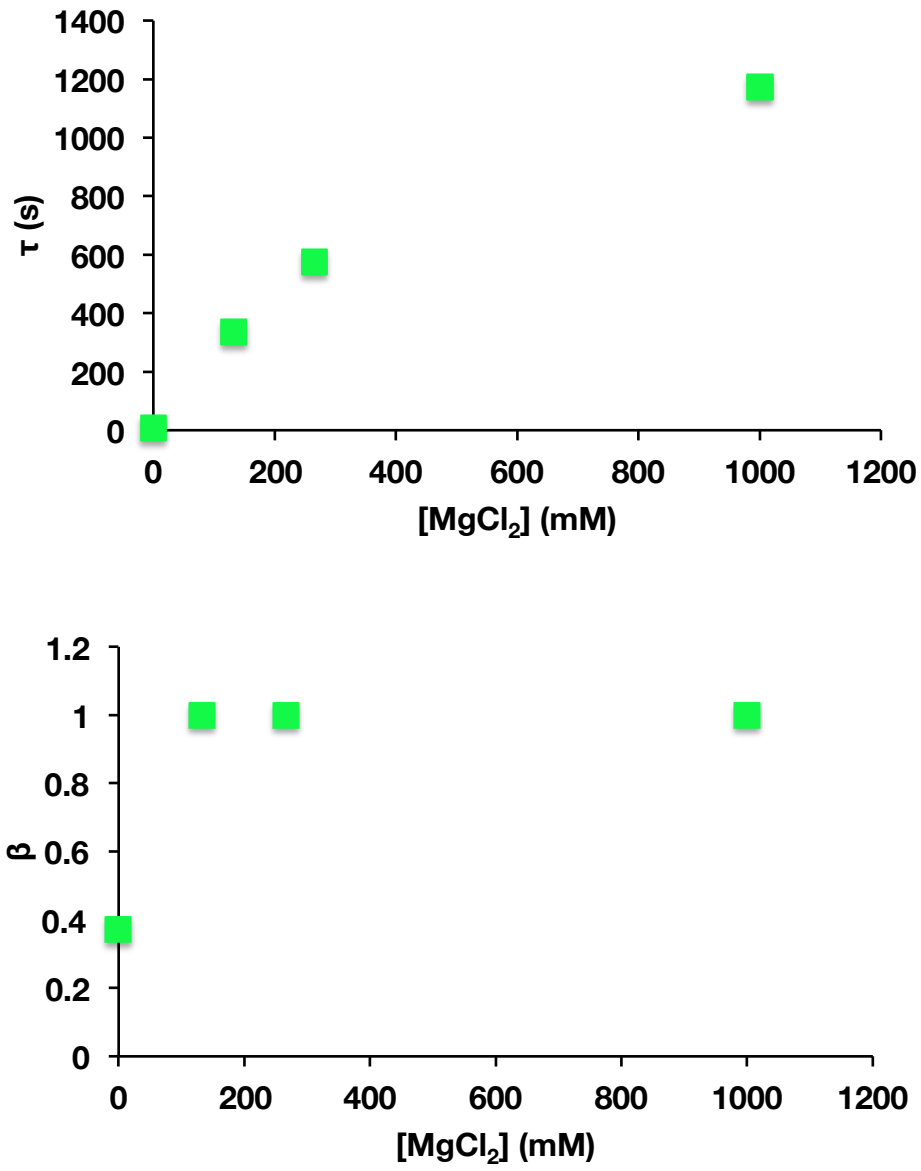

Figure 2. 12: Figure 2. 13: Fit parameters for the adsorption kinetics of base pairing T30p DNA AuNPs in $MgCl_2$ solutions. The same trend is observed as with the non-base pairing T30 DNA-AuNPs. The increase in magnitude of the time constant, τ (top), indicates slower kinetics at higher ionic strengths; the convergence of the stretched exponential, β (bottom), suggests that with increasing ionic strengths the adsorption kinetics follow simple Langmuir adsorption kinetics. All salt concentrations are listed as ionic strength.

The phenomena above did not appear to be unique to $MgCl_2$ solutions. For the base pairing, T30p DNA-AuNPs, comparable trends were noted in NaCl solutions of equivalent ionic strength. Fitting the adsorption kinetics to KWW Langmuir kinetics revealed not only that the kinetics were slowed with increasing ionic strength, but also that the stretched exponential converges to unity, again at 133 mM (Figure 2. 14). The fits conveyed the kinetics closely, the R^2 values were comparable to the four parameter, dual phase model fits described above (e.g. .9987 for the dual phase modes, and .9975 for the KWW model). In fact, at the values where the stretched exponential reached unity, the R^2 values were equivalent.

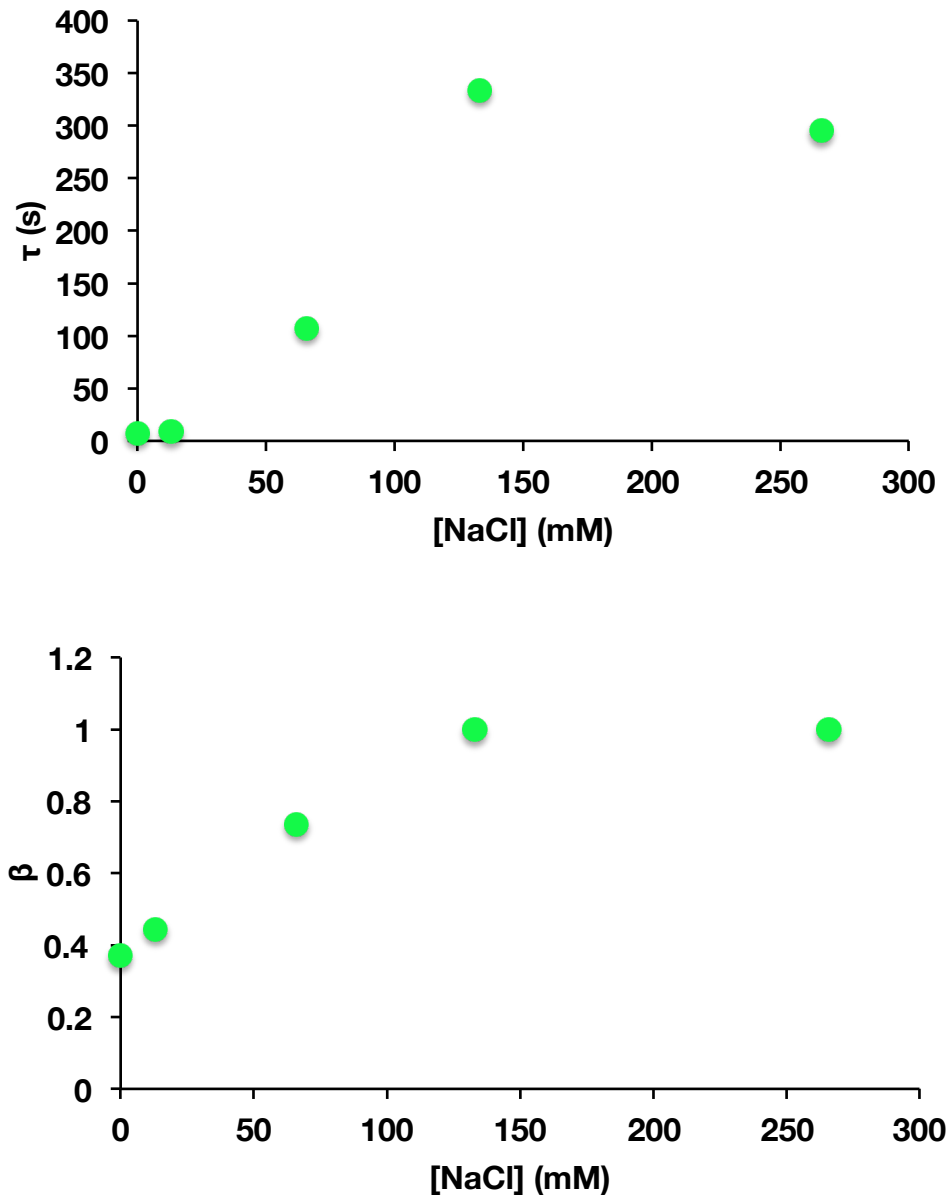

Figure 2. 14: KWW model fit parameters for T30p DNA-AuNPs in NaCl. Similarly to the $MgCl_2$ solutions the base pairing T30p DNA-AuNPs in NaCl fit well to the KWW kinetic model. Though the increase for the time constant, τ (top), was non-monotonic, the general trend was an increase in magnitude with higher ionic strengths. As above, this corresponds to a reduction in adsorption kinetics. Again, the stretched exponential parameter, β (bottom), converged to unity at 133 mM ionic strength.

2.3.3 Surface Structure as Probed by SAXS

In order to probe the development of the nanoparticle structure on the functionalized silicon surface, kinetic GISAXS spectra were recorded (Figure 2. 15). GISAXS spectra allow simultaneous extraction of both the distance between nanoparticles, d, as well as the relative arrangement of the nanoparticles on the surface. The average interparticle spacing of the unordered monolayer can be calculated by,

$$d\ (nm) = \frac{2\pi}{q} \qquad \text{Equation 2.4}$$

where d, is the distance in nm, and q, is the position of the first order peak, in nm^{-1}. Together with the intensity of the first order peak ($I(q)_{max}$), the interparticle distance, d, is plotted in Figure 2. 16. Unsurprisingly, the plot shows that as deposition time is increased, the interparticle spacing is decreased, as more nanoparticles are deposited. What is surprising is that this does not correlate exactly with the peak intensity, which indicates the amount of particles at the surface. While the peak maximum is constantly increasing, the interparticle distance remains constant at the later time points. The reason for this discrepancy is yet uncertain, but may be due to resolution effects of both the beam and the detector. The peak width is a function of the beam width as well as the pixel dimensions; it is possible that changes below a certain threshold cannot be determined under the experimental conditions.

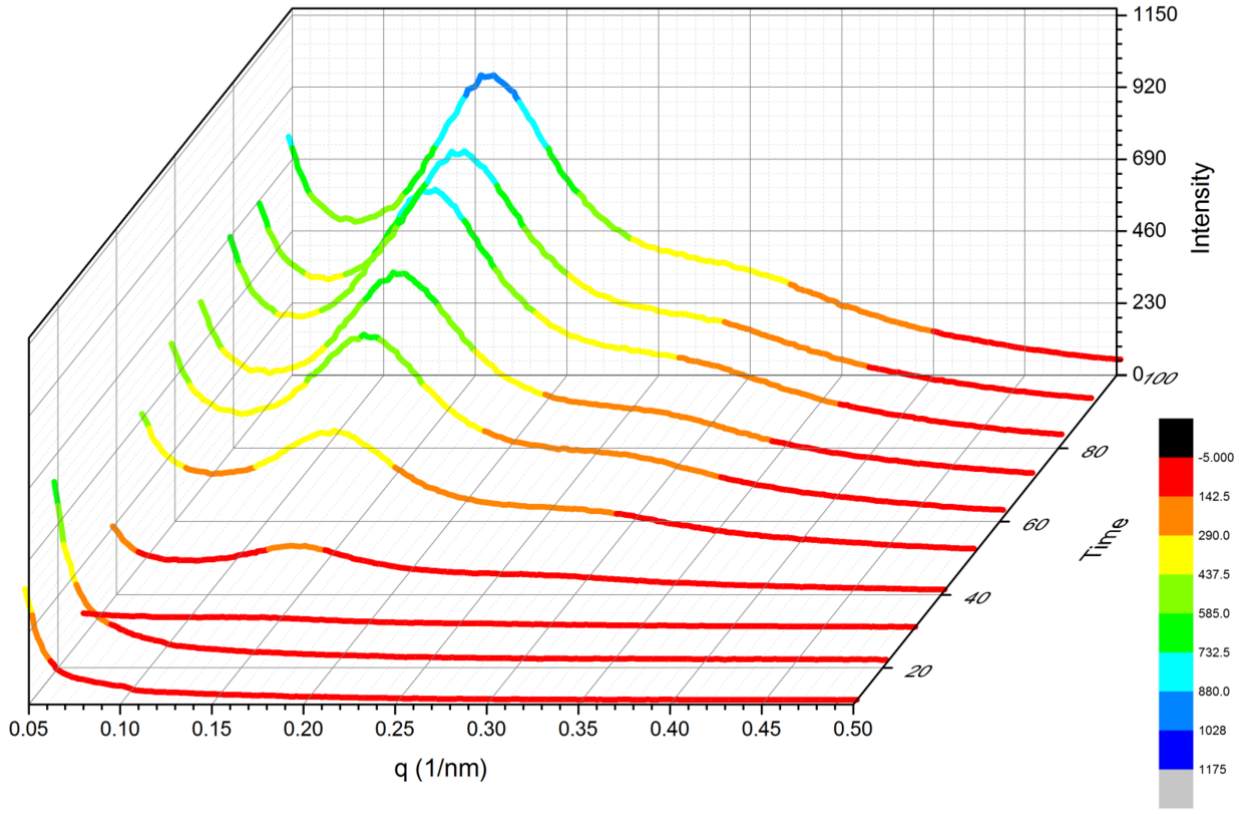

Figure 2. 15: Kinetic evolution of surface structure of T30 DNA-AuNPs on APTES functionalized silicon. One-dimensional GISAXS spectra are plotted over time. Note peak shift toward higher q values, indicating shorter interparticle spacing.

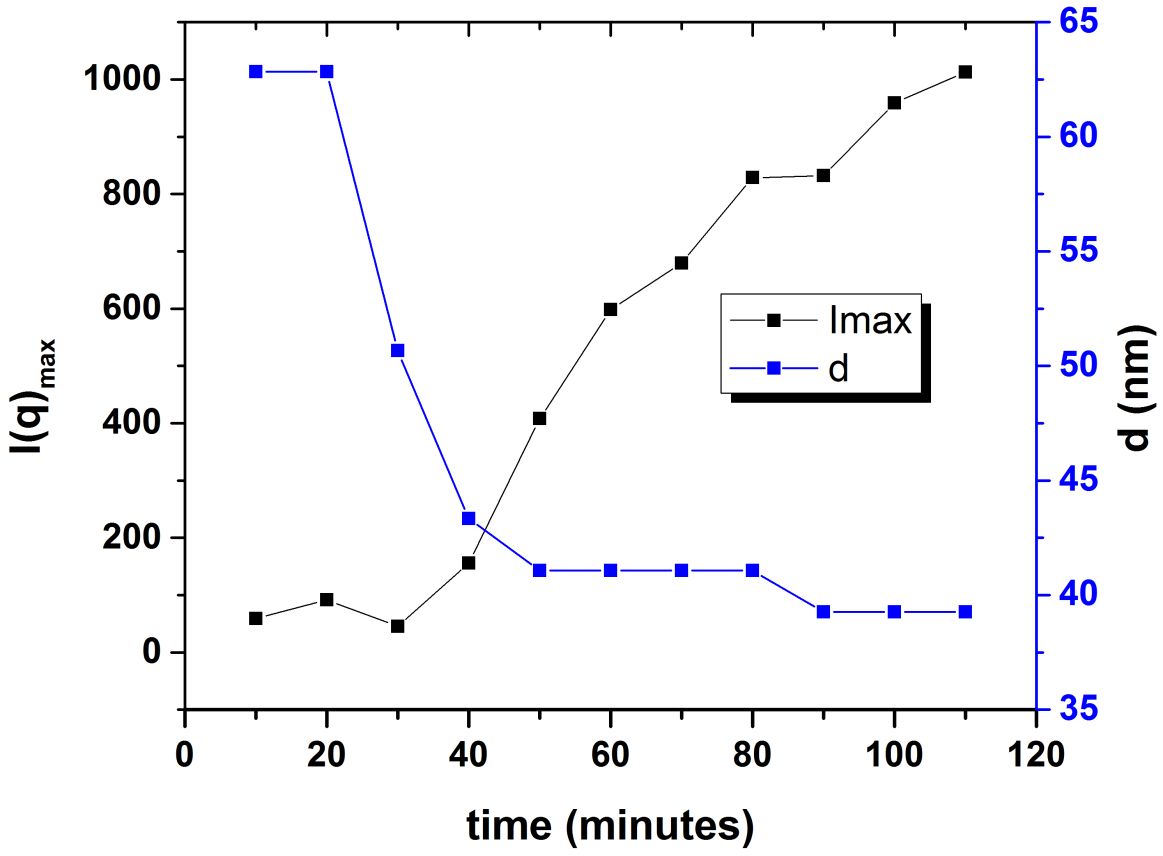

Figure 2. 16: Change in the (blue squares) interparticle spacing, d, and (black squares) peak intensity, $I(q)_{max}$, over time.

2.4 DISCUSSION

The above data present a comprehensive study of the adsorption of DNA-AuNPs on APTES functionalized silicon. By evaluating the various parameters governing the nanoparticle adsorption process, crucial insight can be gained to help optimize the system towards applications such as biosensing and optoelectronics.[11] The conditions studied herein suggest that in order to achieve the highest nanoparticle adsorption amount, short DNA ligands should be used, at high solution ionic strength. While not surprising, as shorter ligands will allow closer packing, and higher ionic strengths will screen repulsive electrostatic interactions, data such as

that presented in Figure 2. 2 show that not only does the difference between ligands increase with ionic strengths, but the saturation coverages seem to reach a maximum between 100-300 mM NaCl.

Further insight can be gained by evaluating the fittings of the QCM data to the kinetic models discussed. A simple Langmuir model cannot fully describe the kinetics of adsorption. This in itself is unremarkable, as the Langmuir model assumes that particle adsorption events will not affect subsequent adsorption, an assumption that cannot be made with the highly negative charged DNA-AuNPs[12]. Despite the simplicity of the Langmuir model, reasonable correlation to the experimental data to this model was seen. Seeking improved fits, two modified Langmuir adsorption models were considered. The first, a simple summation of two Langmuir processes (Equation 2.2), closely captured the kinetic behavior of the non-base pairing nanoparticles NaCl solutions. Inspection of the fitting parameters for the dual-phase model showed that the two time constants, τ_1 and τ_2, generally increased with increasing ionic strength thus showing that the kinetics of adsorption were slowed at higher ionic strength. Moreover, the disparate magnitudes of the time constants imply two processes operating on distinct time scales: one slow and one fast. The fast process likely dominates at the early time points, and would be diffusion limited, while the slow process would dominate at later time points.

These mechanistic insights were altered by the introduction of a base pairing DNA ligand. While the dual phase model did indeed correctly capture the dynamics of adsorption, no trends were seen in the fit parameters. However, it was noted that the time constants converged to the same value at higher ionic strengths. With this in mind, a second modified Langmuir model was explored. The introduction of a stretched exponential (Equation 2.3), β, to the simple Langmuir adsorption model, showed that the distribution of time constants, as described by β,

narrowed with increasing ionic strengths, finally converging to a single value above 133 mM. Notably, the same behavior was seen in $MgCl_2$ solutions with and without base pairing functionality. This leads to a remarkable finding; for DNA-AuNPs in moderate to high ionic strength $MgCl_2$ solutions, as well as base-pairing DNA-AuNPS in NaCl solutions of equivalent ionic strengths, adsorption to a positive interface follows Langmuir kinetics. The striking implication of this conclusion is that interparticle interactions can be effectively screened out at moderate ionic strengths of $MgCl_2$.

Initially the scope of the experiments was designed to find the optimal conditions in which to simply and reliably create ordered monolayers of DNA AuNPs. The GISAXS data from Figure 2. 15, however, do not show the appearance of higher order peaks. In fact the wide first order peaks imply relatively short-range order. Taken together with the relatively fast adsorption kinetics observed herein, it was theorized that the APTES/DNA-AuNP electrostatic bond forms rapidly and securely. With the goal of forming ordered DNA-AuNP systems this thought will serve as a starting point for experiments explored in later chapters.

REFERENCES

1. Sun, S.; Murray, C. B.; Weller, D.; Folks, L.; Moser, A., Monodisperse FePt nanoparticles and ferromagnetic FePt nanocrystal superlattices. *Science* **2000,** *287* (5460), 1989-92.

2. Lee, J.; Hernandez, P.; Lee, J.; Govorov, A. O.; Kotov, N. A., Exciton-plasmon interactions in molecular spring assemblies of nanowires and wavelength-based protein detection. *Nat Mater* **2007,** *6* (4), 291-5.

3. Elghanian, R.; Storhoff, J. J.; Mucic, R. C.; Letsinger, R. L.; Mirkin, C. A., Selective colorimetric detection of polynucleotides based on the distance-dependent optical properties of gold nanoparticles. *Science* **1997,** *277* (5329), 1078-81.

4. Burda, C.; Chen, X.; Narayanan, R.; El-Sayed, M. A., Chemistry and properties of nanocrystals of different shapes. *Chem Rev* **2005,** *105* (4), 1025-102.

5. Tan, S. J.; Campolongo, M. J.; Luo, D.; Cheng, W., Building plasmonic nanostructures with DNA. *Nat Nanotechnol* **2011,** *6* (5), 268-76.

6. Macfarlane, R. J.; Lee, B.; Jones, M. R.; Harris, N.; Schatz, G. C.; Mirkin, C. A., Nanoparticle superlattice engineering with DNA. *Science* **2011,** *334* (6053), 204-8.

7. Tan, S. J.; Kahn, J. S.; Derrien, T. L.; Campolongo, M. J.; Zhao, M.; Smilgies, D. M.; Luo, D., Crystallization of DNA-capped gold nanoparticles in high-concentration, divalent salt environments. *Angew Chem Int Ed Engl* **2014,** *53* (5), 1316-9.

8. A Boker, J. H., T Emrick, TP Russell, Self-assembly of nanoparticles at interfaces. *Soft Matter* **2007,** *3*, 1231-1248.

9. Macfarlane, R. J.; Lee, B.; Hill, H. D.; Senesi, A. J.; Seifert, S.; Mirkin, C. A., Molecular recognition and self-assembly special feature: Assembly and organization processes in DNA-directed colloidal crystallization. *Proc Natl Acad Sci U S A* **2009,** *106* (26), 10493-8.

10. Wolfe, A. R.; Meehan, T., The effect of sodium ion concentration on intrastrand base-pairing in single-stranded DNA. *Nucleic Acids Res* **1994,** *22* (15), 3147-50.

11. Nie, Z.; Petukhova, A.; Kumacheva, E., Properties and emerging applications of self-assembled structures made from inorganic nanoparticles. *Nat Nanotechnol* **2010,** *5* (1), 15-25.

12. Masel, R. I., *Principles of adsorption and reaction on solid surfaces*. 1st ed.; Wiley: New York, 1996; p xiv, 804 p.

CHAPTER THREE:

ELECTROSTATIC SELF-ASSEMBLY OF THREE DIMENSIONAL DNA-CAPPED GOLD NANOPARTICLES

3.1: BACKGROUND

DNA has long served as the gold standard in directing the self-assembly of nanoparticles into three-dimensional crystals. This success is highlighted in recent works by the Mirkin and Gang groups[1-4] whereby dozens of crystal structures have been realized using DNA as a nanoparticle capping ligand. In fact, using DNA the Mirkin group[3] has even managed to synthesize crystal structures that do not exist in nature. This remarkable success is, however, not without its limitations. Using DNA to produce three-dimensional crystals requires extensive sequence design and time-consuming functionalization and assembly steps. Its applicability is also hindered by the range of ionic environments in which these crystals can be formed; DNA-mediated self assembly of nanoparticle crystals is achieved using a very specific NaCl solution at precise temperature.

Recently our group demonstrated that by using single stranded non-base pairing DNA AuNPs could be made to crystallize in solutions of various ionic strengths, greatly extending the utility of DNA-AuNP crystals.[5] The crystals formed, while of remarkably high quality, were only formed in two dimensions at the air water interface. Here it is shown, that by using the same DNA ligands and similar crystallization methods, three-dimensional nanoparticle crystals can be formed in solution.

3.2 MATERIALS AND METHODS

3.2.1 Synthesis of DNA-capped Gold Nanoparticles

Gold nanoparticles DNA conjugates were synthesized as described in section 2.2.1. Similar sequences were used, that is polythymine oligonucleotides of varying length, T10, T15,

T30, T45, and T10.

3.2.2 Small Angle X-ray Scattering Experiments

Small angle X-ray scattering experiments (SAXS) were performed at the D1 experimental station at the Cornell High Energy Synchrotron Source (CHESS). An incident X-ray beam with a flux of ~10^{12} photons s^{-1} mm^{-1} was used with a bandwidth of 1.5% achieved using a multilayer monochromator. The dimensions of the collimated X-ray beam were 0.3 mm (horizontal) and 0.2 mm (vertical). Data from two separate runs were used- nanoparticle crystals made using Ca^{2+} counterions was conducted in 2012. During these experiments a MedOptics CCD detector with a pixel size of 46.9 x 46.9 microns was used, with a sample-to-detector distance of 1873 mm and a wavelength of 1.26 Å. The crystallites formed using Mg^{2+} counterions were prepared in 2016 using a 1.168 Å beam, a sample-to-detector distance of 1416 mm, and a Pilatus 200k detector with a pixel size of 172 x 172 microns. The Pilatus detector consists of two vertically stacked detector modules with a non-detecting space in between. In order to collect data that may be present in this space select images were taken by vertically moving the detector. These images were used only for qualitative evaluation.

Individual scattering spectra were collected by placing a ~2 μL of DNA-AuNPs in salt solution on a cleaned Si substrate. In order to avoid drying effects, the substrate was placed in a sealed sample environment chamber with a reservoir of equal salt concentration (Figure 3. 1). A raster scan of the droplet was then performed by moving the sample stage to obtain a droplet profile. This allowed spectra to be selected from the solid-liquid, bulk, or air-water interface.

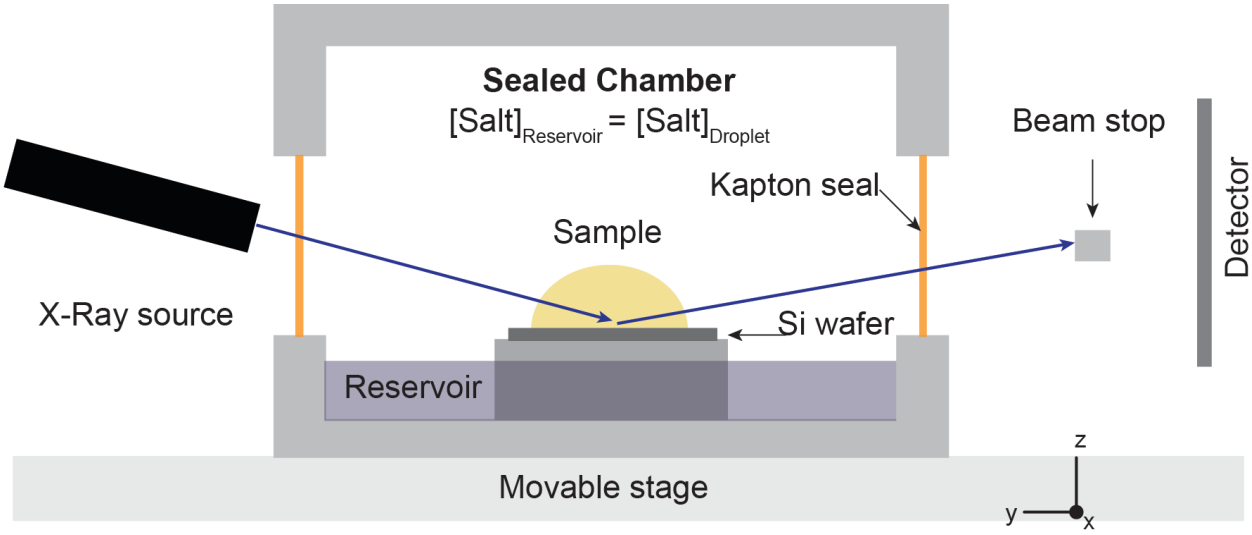

Figure 3. 1: Schematic of the sealed sample environment chamber used to minimize drying effects of colloidal droplets.

3.2.3 X-ray Data Analysis

The two dimensional scattering intensity, $I(q)$, of the nanoparticles is proportional to the Vineyard factor, $V(q_z)$, accounting for substrate effects and depending on the incident angle of the X-ray beam, the structure factor of the distribution of nanoparticles, $S(q_x)$, and an average form factor due to the scattering from individual, non-interacting particles, $F(q_x, q_z)$: (reference)

$$I(q) = V(q)S(q)F(q). \tag{3.1}$$

The form factor can be accurately determined from a scattering spectrum of a dilute solution of nanoparticles. For spherical nanoparticles of radius R, the form factor itself can be expressed as

$$F(q) = \int_0^\infty N(R)P(q,R)R^6 dR, \tag{3.2}$$

where

$$P(q,R) = \left(3\frac{\sin(qR) - qR\cos(qR)}{(qR)^3}\right)^2, \tag{3.3}$$

and

$$N(R) = \frac{1}{\sigma\sqrt{2\pi}} exp\left[-\frac{(R-R_o)^2}{2\sigma^2}\right]. \quad (3.4)$$

where a Gaussian distribution of nanoparticles is assumed with mean radius R_0, and a standard deviation σ.

For the bulk solution and at the air-water interface, the Vineyard factor will be unity since there are no substrate effects. However, at the solid-liquid interface the silicon substrate may enhance the scattering near the critical angle, α_c, (0.18° for Si). In this case the Vineyard factor depends on the substrate critical angle, the incipient X-ray beam angle, and q_z:

$$V(q_z) = \begin{cases} 0, \ q_z < \frac{2\pi}{\lambda}\sin\alpha_i \\ \left| \frac{q_z - 2\frac{2\pi}{\lambda}\sin\alpha_i}{q_z - 2\frac{2\pi}{\lambda}\sin\alpha_i + \sqrt{\left(q_z - 2\frac{2\pi}{\lambda}\sin\alpha_i\right)^2 - \left(\frac{2\pi}{\lambda}\sin\alpha_c\right)^2 + 0.01i}} \right|^2, \ q_z \geq \frac{2\pi}{\lambda}\sin\alpha_i \end{cases}. \quad (3.5)$$

Here, q_x and q_z are calculated from the wave vector $q = k_f - k_i$, where q is composed of parallel and perpendicular components $q = (k_{f,x} - k_{i,x})\hat{\imath} + (k_{f,z} - k_{i,z})\hat{k} = q_x\hat{\imath} + q_z\hat{k}$. $\hat{\imath}$ is the x unit vector while $\hat{k}$ is the unit vector in the z direction, with vector magnitudes defined by $k_{f,x}, k_{i,x}, k_{f,z}, k_{i,z}, q_x,$ and q_z. The wave vector transfer coordinates, $q_x,$ and q_z, have angular dependence as defined by, $q_x = (2\pi/\lambda)[\sin 2\theta_f \cos\alpha_f]$, and $q_z = (2\pi/\lambda)[\sin 2\alpha_f \cos\alpha_i]$, where α_i is the incident beam angle, whose magnitude $|q| = q = \sqrt{q_x^2\hat{\imath} + q_z^2\hat{k}}$. In the case of isotropic scattering this can be simplified to $q = (4\pi/\lambda)\sin\theta_f$, at a scattering angle of $2\theta_f$. The resulting enhancement occurs at low q_x and quickly drop off to unity in the experimental setup, where an incident beam angle of 0.25° was used, unless otherwise noted. In the regime where dilute scattering effects at high scattering angles are minimal, the structure factor can be written as:

$$S(q) = S_0(q)D(q), \quad (3.6)$$

where $S_0(q)$ defines the location and shape of the Bragg reflections. In the case of the ssDNA-AuNPs, three crystal arrangements were considered, a simple two-dimensional hexagonal lattice, a three-dimensional face centered cubic lattice (FCC) , and a three-dimensional hexagonal close packed lattice (hcp). For the two-dimensional hexagonal lattice, the peak locations are given by

$$S_0(q_x) = \sum_{hk} m_{hk} L(q_x), m_{hh} = m_{h0} = 6, m_{hk} = 12, \quad (3.7)$$

and for the three-dimensional lattices

$$S_0(q_x) = \sum_{hk} m_{hkl} L(q), \quad (3.8)$$

where for FCC lattices the peak multiplicities, m, are m_{h00} = 6, m_{hh0} = 12, m_{hhh} = 8, m_{hk0} = 24, m_{hhk} = 24, and m_{hkl} = 48, while for the hcp lattice, m_{h00} = 6, m_{00l} = 2, m_{hho} = 6, m_{hk0} = 12, m_{0kl} = 12, m_{hhl} = 12, and m_{hkl} = 24. Deviation from an ideal lattice is accounted for by the static Debye-Waller factor, $D(q)$,

$$D(q) = \exp(-\sigma_{DW}^2 q), \quad (3.9)$$

where σ_{DW}, is the relative displacement from an ideal lattice. $L(q)$, is a Lorentzian function which describes the shape of the Bragg reflections,

$$L(q) = \frac{1}{1+\frac{D_g^2(q-q_{hkl})}{4\pi^2}}, \quad (3.10)$$

where D_g is the crystallite size. The Scherrer equation describes the relationship between the crystallite grain size, and the full width at half maximum of a peak, B_{hkl}:

$$D_g = \frac{K\lambda}{B_{hkl}\cos\theta_{hkl}}, \quad (3.11)$$

at a given Bragg reflection, θ_{hkl}, and wavelength, λ, with a Scherrer constant, K, of 0.90[6].

3.3 RESULTS

3.3.1 SAXS Spectra

The unique advantage of the experimental setup employed allows spectra to be selected from the region of interest. By raster scanning the droplet, a droplet profile can be obtained, clearly delineating the three aqueous environments of the DNA-AuNPs: the air-water interface, the bulk solution, and the solid-liquid interface. The ability to study all three regions simultaneously is necessary to fully probe the dynamics of DNA-AuNPs in salt solutions. A sample raster scan is shown in Figure 3. 2a. It should be noted that the detector employed records mirror images, thus the specular reflections imaged at the air-water interface shown at Figure 3. 2a, are actually reversed. From the figure it is evident that the three regions exhibit unique spectra, arising from a difference in the assemblies forming at each region. For instance, Figure 3. 2b shows a well-structured assembly from the air-water interface, while Figure 3. 2c shows a less structured spectrum mostly resulting fro the nanoparticle form factor. The spectrum shown in Figure 3. 2d shows the scattering resulting from a three-dimensional nanoparticle lattice at the solid-liquid interface, a typical grazing incidence small-angle x-ray scattering (GISAXS) spectrum. The nature of these differences will be discussed later.

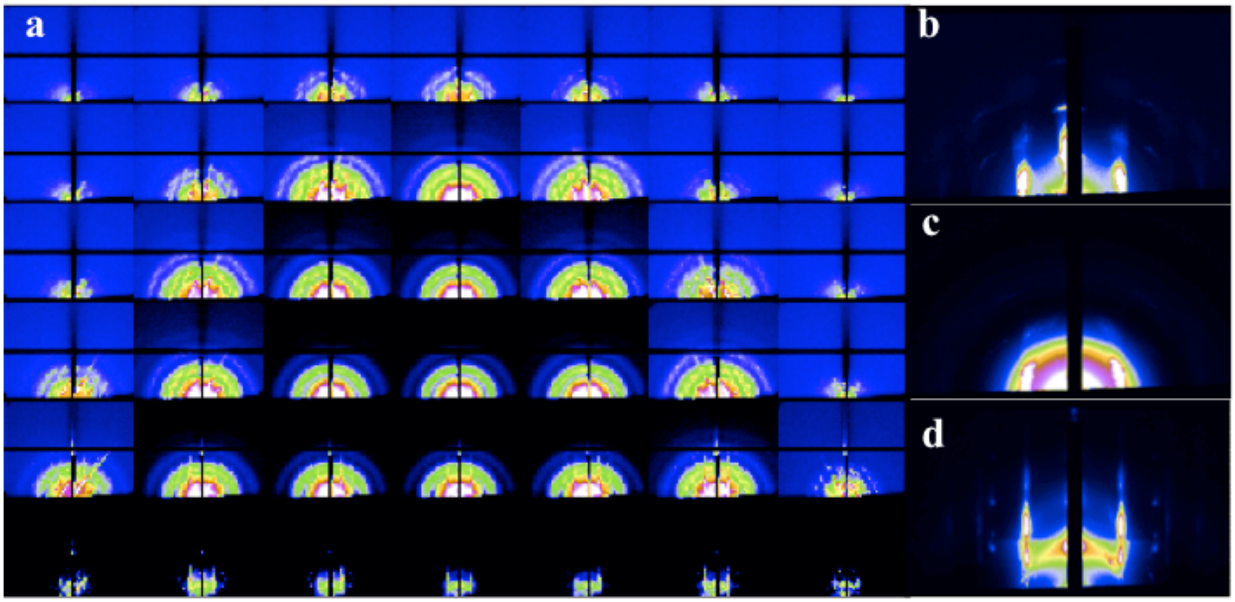

Figure 3. 2: Sample spectra obtained by raster scanning of droplet showing, a) droplet profile, b) an air-water interface scattering spectrum, c) bulk scattering spectrum, and d) solid-liquid interface spectrum.

SAXS experiments were conducted in solutions of $CaCl_2$ and $MgCl_2$ at ionic strengths of 0 to 2400 mM. Remarkably, the range over which the two salts formed structured three-dimensional aggregates greatly differed. Moreover, the types of crystal structures formed in solution could be varied with the choice of salt. Calcium chloride solutions were able to form ordered aggregates in a surprisingly narrow range of ionic strength. For the four DNA ligands tested, T15, T30, T45, and T60, only the three longer ligands, T30, T45, and T60 formed crystals. Furthermore, among the ionic strengths tested, 150 mM, 450 mM, 600, mM and 900 mM, long range order was only observed at 600 mM. 1D radially integrated spectra and the corresponding scattering 2D spectra are shown in Figure 3. 3. It can be seen that all three DNA ligands form similar structures.

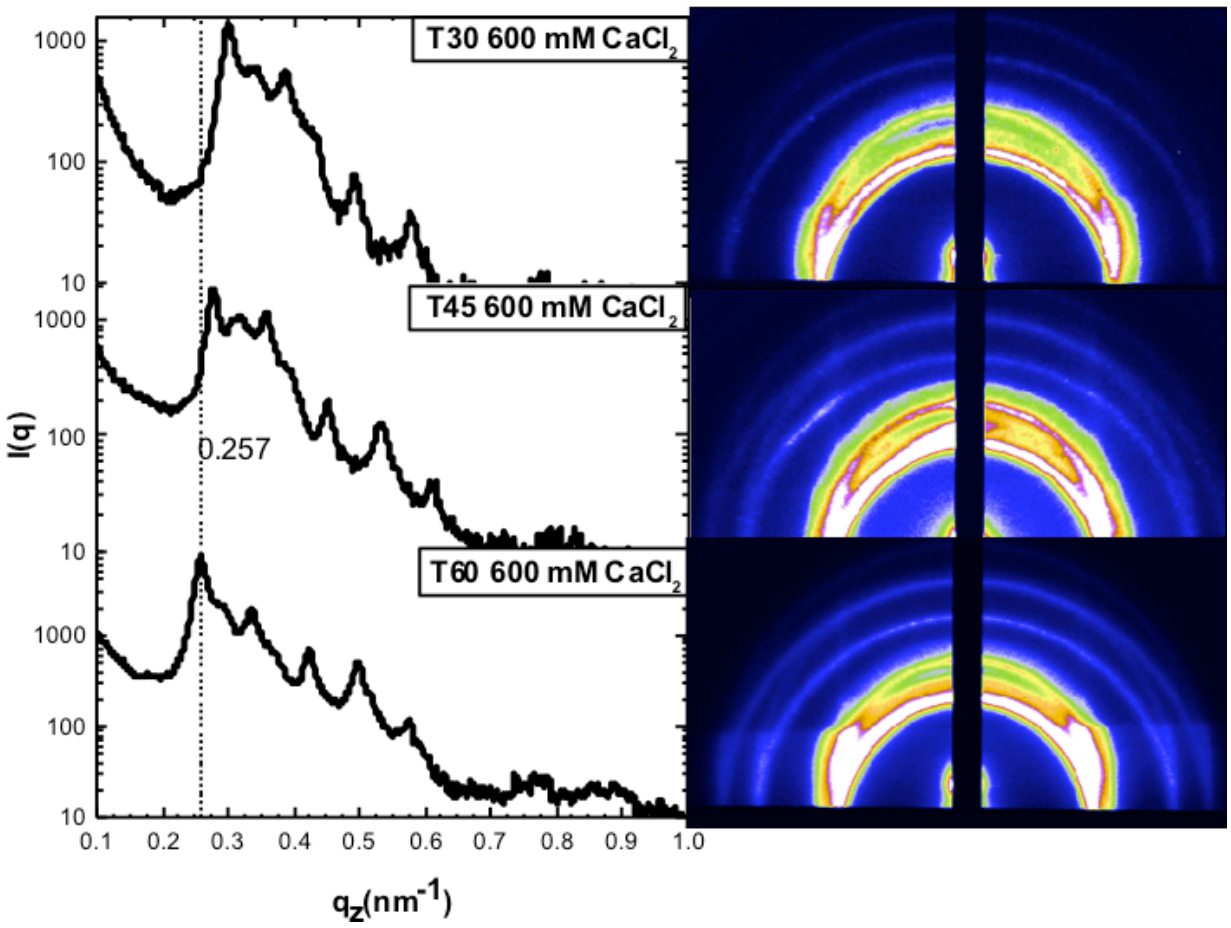

Figure 3. 3: 1D (left) and 2D (right) scattering spectra for the various ligands tested in 600 mM $CaCl_2$. The position of the first peak, marked by the dashed line for the T60 DNA-AuNPs, is inversely related to the interparticle spacing, and thus the T60 DNA-AuNPs exhibit the largest spacing.

The precise arrangement of the nanoparticles can be deduced by indexing the peak positions of the linecuts shown above. According to diffraction selection rules for a FCC crystal,[7] whose unit cell is shown on the left in Figure 3. 4, the relative peak positions should occur at q/q_1= 1, √4/3, √8/3, √11/3, 2, √19/3, √20/3, and √24/3 for the range shown above. Indeed, these peak positions correspond well to the FCC peak positions shown by the dashed red lines in Figure 3. 5.

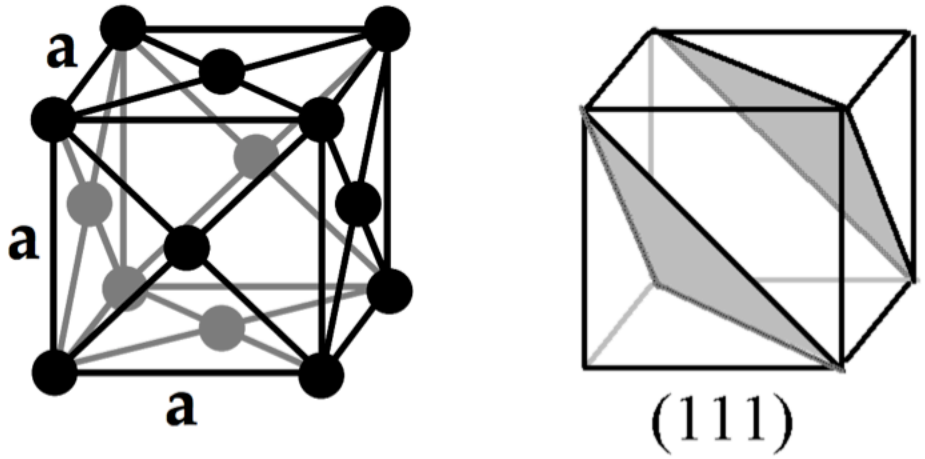

Figure 3. 4: FCC unit cell showing nanoparticle positions (left) and the poition of the (111) planes within the unit cell.

The structure factors, *S(q)*, shown in Figure 3. 5 were obtained by dividing out the experimentally obtained form factor (spectrum from a dilute nanoparticle solution with no salt added) from the spectra shown in figure 3.3. Due to the limited dynamic range of the Pilatus detector employed, the low pixel values in the high q region (where q > ~2), where little scattering is detected results in a low signal-to-noise ratio in this region. The arrangement into FCC crystals of DNA coated nanoparticles has previously been reported for a T45 DNA ligand, although at a different $CaCl_2$ concentration[8].

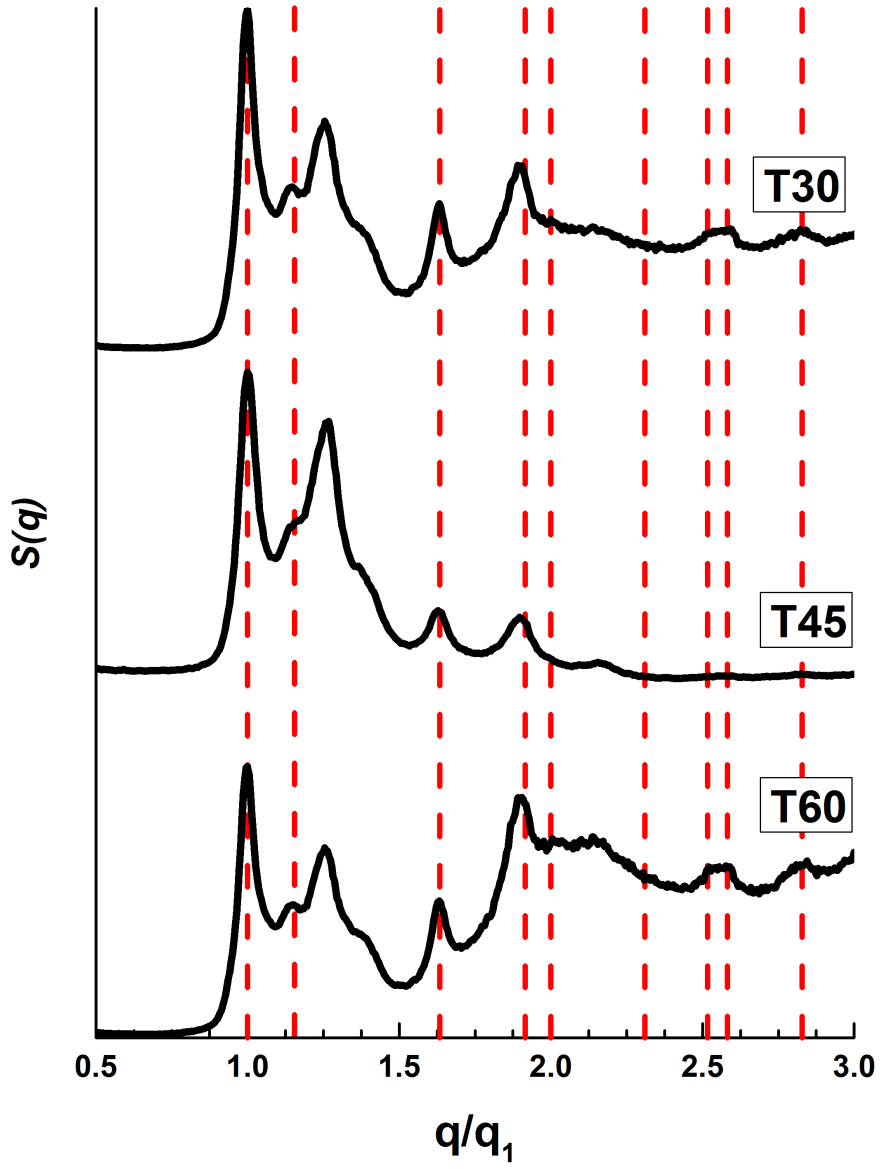

Figure 3. 5: Structure factors, obtained by dividing the 1D scattering spectra in **Figure 3. 3** by the experimentally obtained form factors, of the nanoparticle crystals formed in 600 mM $CaCl_2$. The close congruity with the FCC peak positions, indicated by the dashed red lines, confirms the crystal structure. The peak positions in each spectrum are normalized to the position of the first order peak.

As expected, the nanoparticle nearest neighbor distance increased for the longer DNA ligands.[9] This can be seen in Figure 3. 3 by the shift position of the first order peak, indicated by a dashed line for T60, where the horizontal axis, corresponding to reciprocal space in nm^{-1}, the shift to larger q-values for smaller ligands indicates a smaller spacing. For a FCC lattice, the first order peak corresponds to the Bragg reflection of the (111) plane (Figure 3. 2, right). Therefore, by applying geometric relations, the nearest neighbor spacing, $D_{nn,}$ can be calculated by

$$D_{nn}(nm) = \frac{\sqrt{6}\pi}{q}. \tag{3.12}$$

For the data shown in Figure 3. 3, this corresponds to nearest neighbor spacings of 29.9 nm, 27.6 nm, and 25.6 nm, for the T60, T45, and T30 ligands, respectively. By subtracting the contribution of nanoparticle core (13.82 nm) and the alkyl spacer of the thiol functional group of the DNA ligand (0.5 nm) this corresponds to DNA ligand lengths of 7.9 nm for T60, 7.6 nm for T45, and 5.6 nm for the T30 ligand.

Similar results were observed in $MgCl_2$ solutions. Figure 3. 6 shows the scattering from both T30 and T60 DNA-AuNPs at the highest $MgCl_2$ concentration tested, 2400 mM. As in the case of the $CaCl_2$ solutions, from the position of the first order peak it can be seen that the ligand can be used to control the lattice interparticle spacing. Once again FCC lattices were formed. The normalized structure factors with the corresponding FCC peaks are shown in Figure 3. 7. The curves indicate well ordered FCC crystals, but again a low signal-to-noise ratio is evident in the high q range.

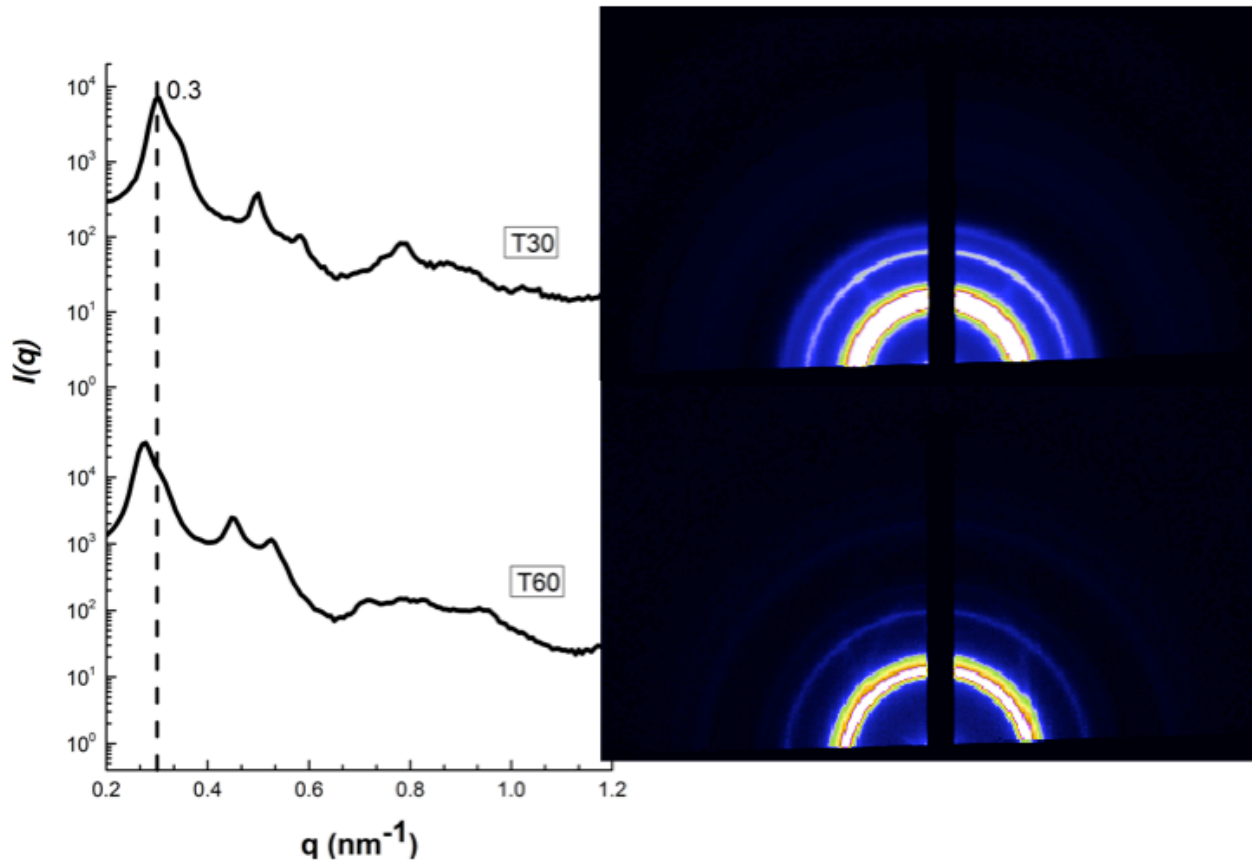

Figure 3. 6: 1D scattering curves (left) and full scattering spectra (right) of T30 and T60 DNA-AuNps in 2400 mM $MgCl_2$. The position of the first order peak, as indicated by the dashed line for the T30 DNA-AuNps, demonstrates the difference in spacing between the two samples.

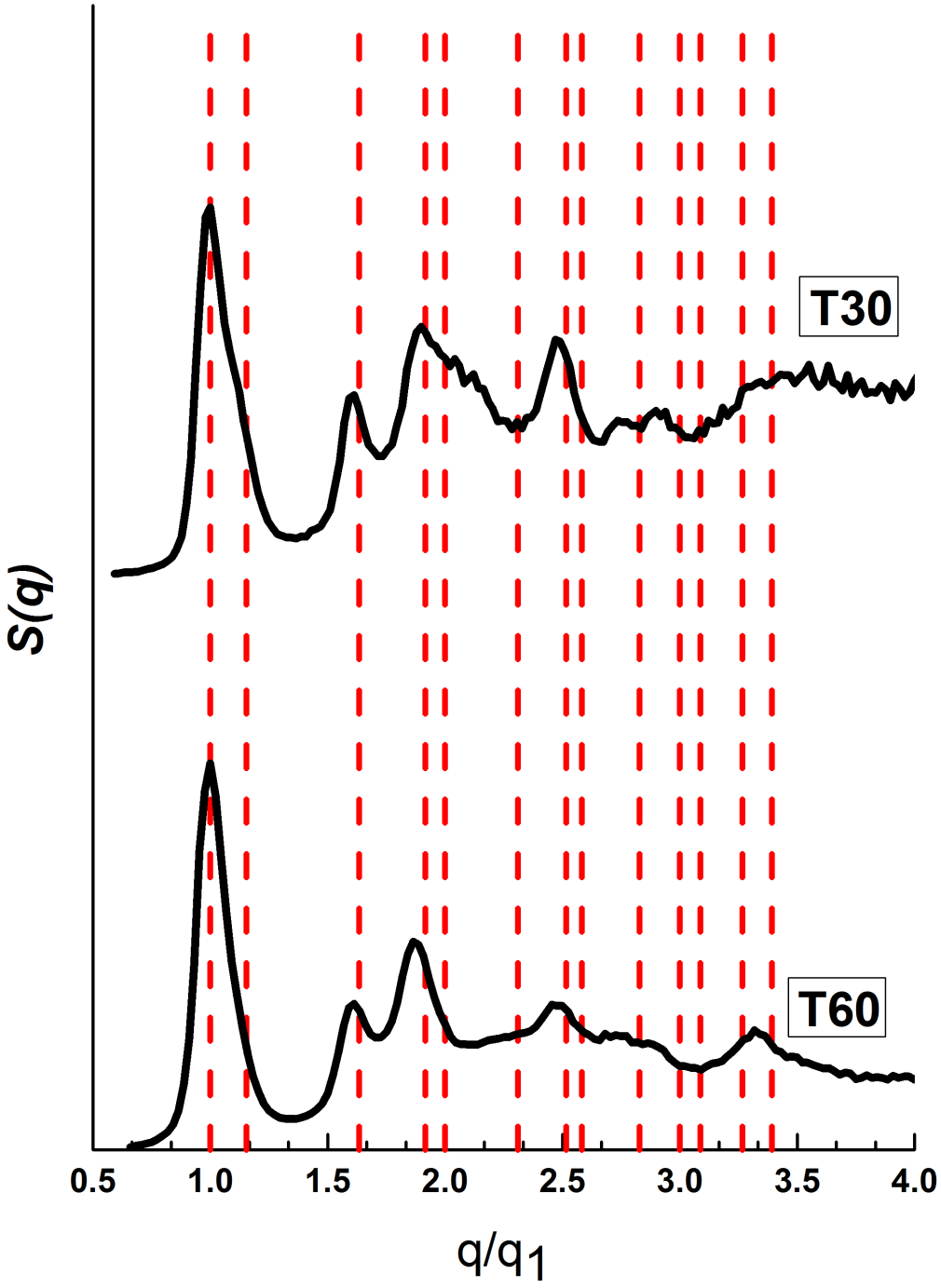

Figure 3. 7: Normalized structure factor for T30 and T60 DNA-AuNPs in 2400 mM $MgCl_2$. The red lines indicate the FCC peak positions.

Unlike the $CaCl_2$ solutions, the FCC lattices were formed over a range of ionic strengths. For the T30 DNA-AuNPs FCC lattices were formed at 1650, 1800, and 2400 mM (although, as mentioned above, only at 2400 mM $MgCl_2$ for T60 ligands, and not at all for the T15 ligands). While the quality of crystals formed did not seem to vary in this range, as interpreted by the number of FCC peaks present, the interparticle spacing was reduced at higher ionic strengths. The D_{NN}, as calculated above, was 26.0, 25.0, and 24.4 nm for the $MgCl_2$ solutions of 1650, 1800, and 2400 mM, respectively. This change in interparticle spacing is reflected in Figure 3. 8, where the first order peak for 1650 mM $MgCl_2$ is indicated by the dashed line. In addition to the aforementioned counterion species and ligand length, the solution ionic strength presents another parameter from which to vary the crystal structure.

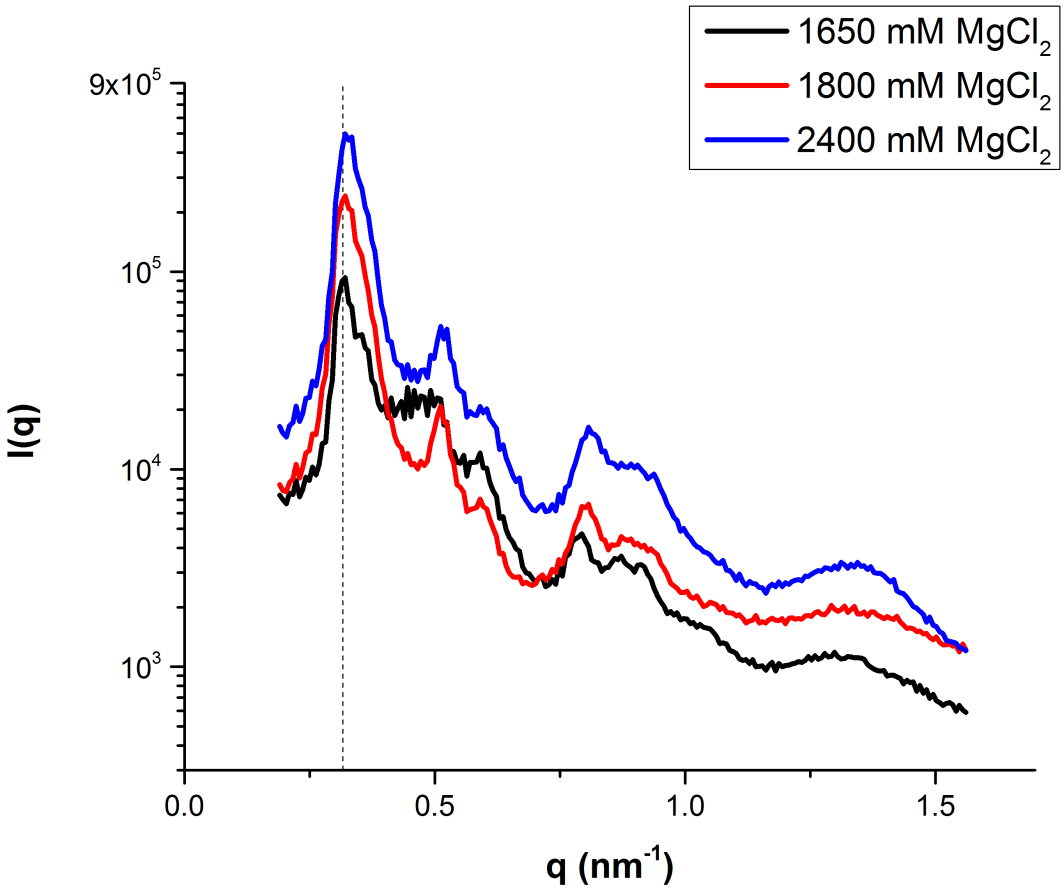

Figure 3. 8: Radially integrated scattering curves of T30 DNA-AuNPs in $MgCl_2$ solutions. The first order peak position, indicated by the dashed line for 1650 mM $MgCl_2$ moves to higher q values for higher ionic strengths, indicating smaller interparticle distances.

A remarkable difference in structure was observed at lower ionic strengths. For T30 DNA-AuNPs in solutions of 1500 mM $MgCl_2$, and in both 1650 and 1800 mM $MgCl_2$ for the T60 DNA-AuNPs, well-oriented three-dimensional structures resembling a hexagonal close packed (HCP) lattice were observed (Figure 3. 9A). The scattering observed, shown in spectra taken from the solid liquid interface, are the result of the stacking of two-dimensional hexagonal layers. The position of the vertical Bragg rods, are indicative of the two-dimensional nanoparticle arrangement (Figure 3. 9B). However, the truncation in the Bragg rods, as indicated

by the regularly spaced dots, are indicative of three-dimensional stacking. In the case of an FCC lattice each dot would be a doublet of peaks. However the regularly spaced scattering occurs as a single peak, indicating the presence of an HCP lattice, differing only from the FCC lattice by the relative stacking of the two-dimensional hexagonal crystal planes.[10] This is further confirmed when looking at a linecut taken from the truncated Bragg rods (Figure 3.9C), where the regularly spaced singlet peaks can be confirmed (Note: structure factor calculations were attempted but the low form factor detected proved difficult to fit). Smilgies *et al*. demonstrated that the GISAXS relative peak spacing in stacked hexagonal layers occur in intervals of 0.5 q_1 (or q/q_1= 1 q_1, 1.5 q_1, 2.0 q_1, … etc.). Close correlation to these theoretically predicted peaks can be seen from the vertical linecuts shown in Figure 3. 9D. The slight deviations from the HCP lattice theoretically predicted, as seen from slight deviations in ideal peak positions, may be explained by the lower total scattering values recorded at the solid-liquid interface. This may also be an indication of the existence of a random hexagonal packing (rHCP) lattice, where the HCP lattice and the FCC lattice are intermixed.

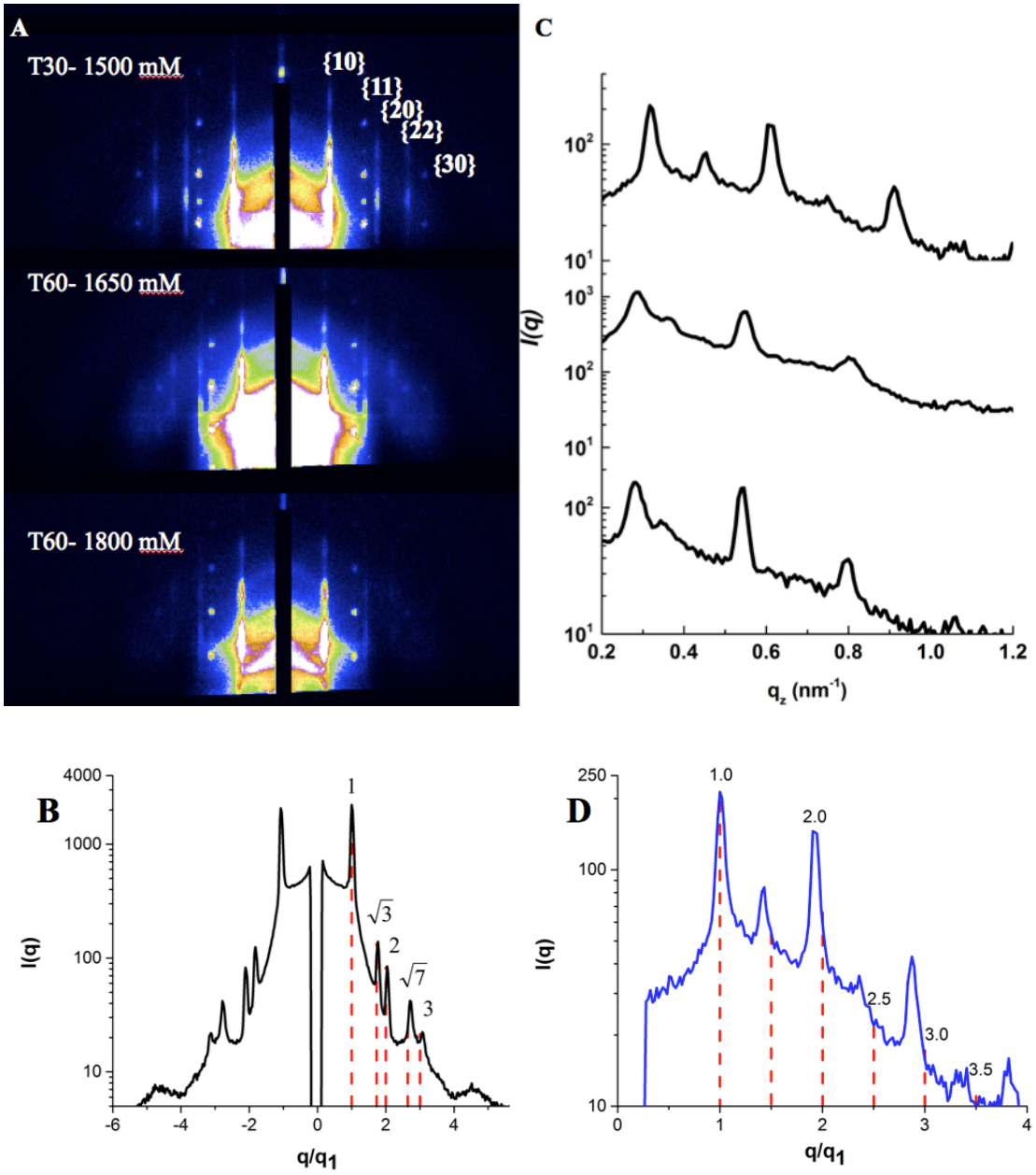

Figure 3. 9: Scattering spectra of (A-top) T30-DNA AuNPs at 1500 mM $MgCl_2$, (A-middle) T60 DNA-AuNPs at 1650 mM $MgCl_2$ and (A-bottom) T60 DNA-AuNPs at 1800 mM $MgCl_2$ forming HCP lattices. B) Horizontally integrated spectra of the T30 DNA-AuNP at 1500 mM $MgCl_2$ with corresponding 2D hexagonal reflections indicated by the vertical red lines. C) vertical linecuts along the {10} Bragg rod (B). D) Normalized vertical linecut along {10} Bragg rod of T30-DNA AuNP at 1500 mM $MgCl_2$ with HCP reflections indicated by the red lines.

		Crystallite Grain Size (nm)		
	IS (mM)	**T30**	**T45**	**T60**
Ca	**600**	810	880	860
	1650	350	not tested	--
	1800	400	not tested	--
Mg	**2400**	360	not tested	390

Table 3. 1: Estimated crystallite grain sizes

3.3.2 Grain Sizes

In addition to the variety of lattice types formed between the $CaCl_2$ and $MgCl_2$ samples, an important difference between the sizes of the FCC crystallites formed was noted. Using equations 3.1-3.10 to fit the scattering observed and subsequently equation 3.11 to estimate the grain size, a substantially larger crystallite was calculated for the $CaCl_2$ samples. The samples formed using calcium counterions formed crystallites around ~800 nm while those in magnesium were around ~375. The difference in the spacing (tabulated in Table 3. 1) can be seen in the scattering curves and fits in Figure 3. 10, where the larger first order peak width of the $MgCl_2$ sample illustrates the smaller crystallite grain size. Using the previously calculated interparticle spacings, this corresponds to ~31 nanoparticles per crystallite in $CaCl_2$ as compared to ~16 nanoparticles for the $MgCl_2$ samples. Both of these numbers are larger than those reported by Bedzyk and co-workers [8], whose crystallites were on the 250 nm scale.

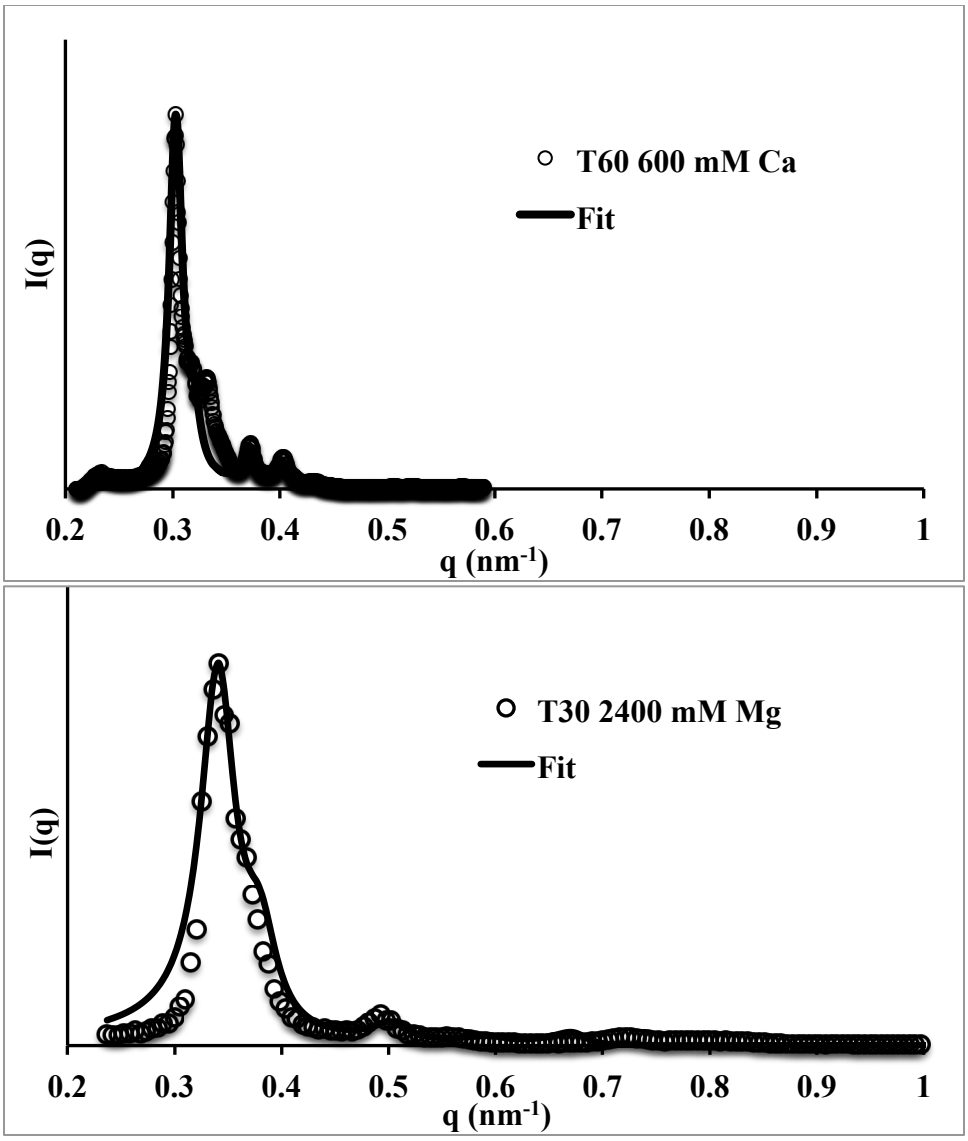

Figure 3. 10: Experimental scattering curve and model fit used to estimate the crystallite grain size for the (top) T60 DNA-AuNPs in 600 mM $CaCl_2$ and (bottom) for the T30 DNA-AuNPs in 2400 mM $MgCl_2$.

3.3.3 Crystal Structure Variation

To gain a full understanding of the nanoparticle dynamics in solution it is necessary to compare the scattering across the various areas of the droplets. Indeed, it can be seen from Figure

3. 1 that the scattering is not uniform throughout the droplet. In particular, differences between the two liquid interfaces stand out. Curiously, within the same droplet, two crystal lattices can be observed. At the solid-liquid interface, the FCC lattice is formed, as seen in the top of Figure 3. 11, while at the air-liquid interface, the peak spacings of the {11} Bragg rod indicate an HCP lattice.

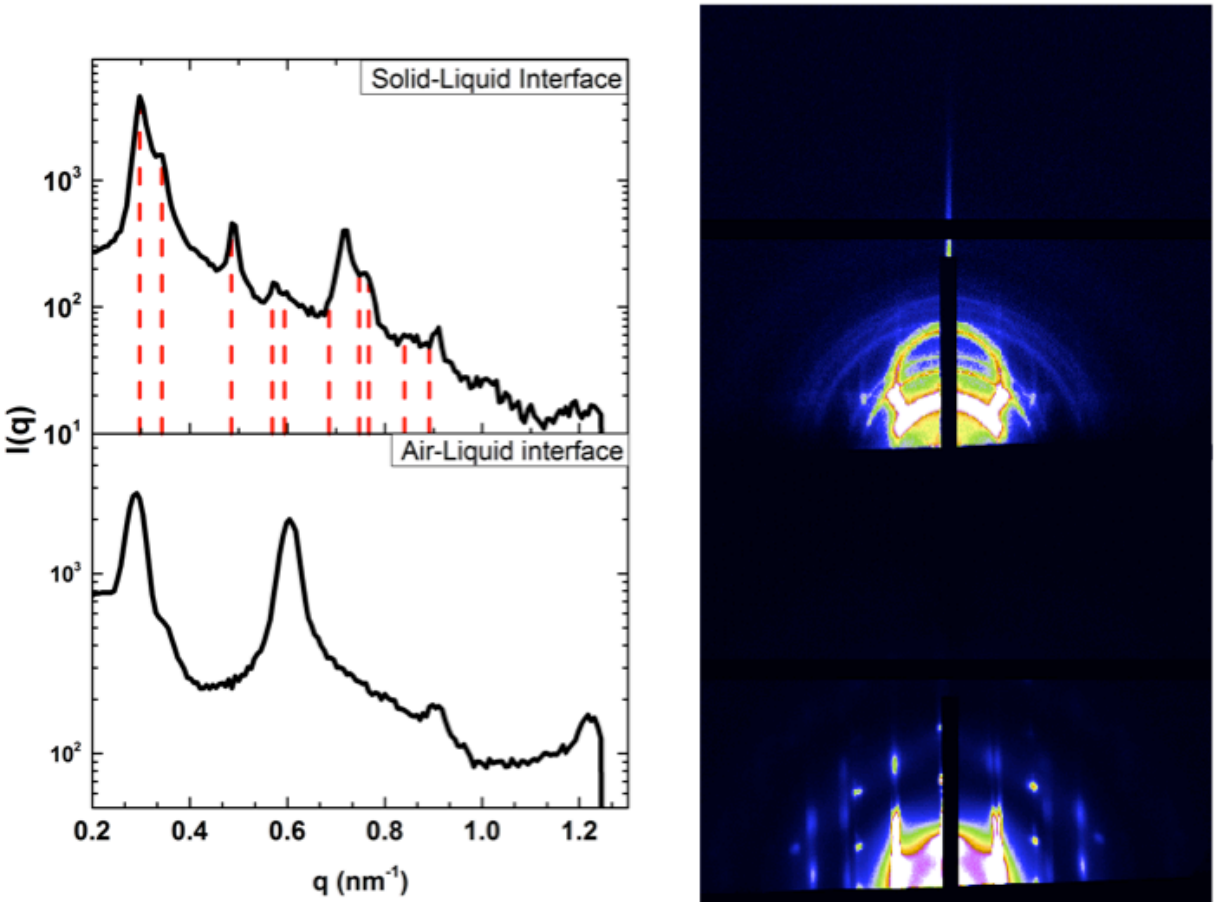

Figure 3. 11: 1D SAXS intensity profiles and scattering spectra at the solid-liquid interface (top) and at the air-liquid interface (bottom) for T30 DNA-AuNPs at 1800 nM. The 1D profile shown for the air-liquid interface is taken from the {11} Bragg rod. FCC peak positions are indicated for the FCC forming lattice at the solid-liquid interface.

Conversely, at higher $MgCl_2$ concentrations (2400 mM), the only 3D lattice present is FCC at the solid-liquid interface, although a 2D Gibbs layer persists at the air-liquid interface. As seen in Figure 3. 12, the 2D layer is a hexagonal Gibbs layer, as indicated by the peak positions in red. The absence of multiple FCC peaks, as shown in blue, and close correspondence with the hexagonal peaks further confirm this. Similarly, the solid-liquid interface spectra (top) agree closely with the FCC peaks as indicated in blue. This interfacial disparity can also be seen in the position of the first order peaks. The positions indicated in the 1D spectra coincide with a nearest neighbor spacing of 25.5 nm in the hexagonal layer of the air-water interface and 23.9 nm for the 3D crystals at the solid-liquid interface.

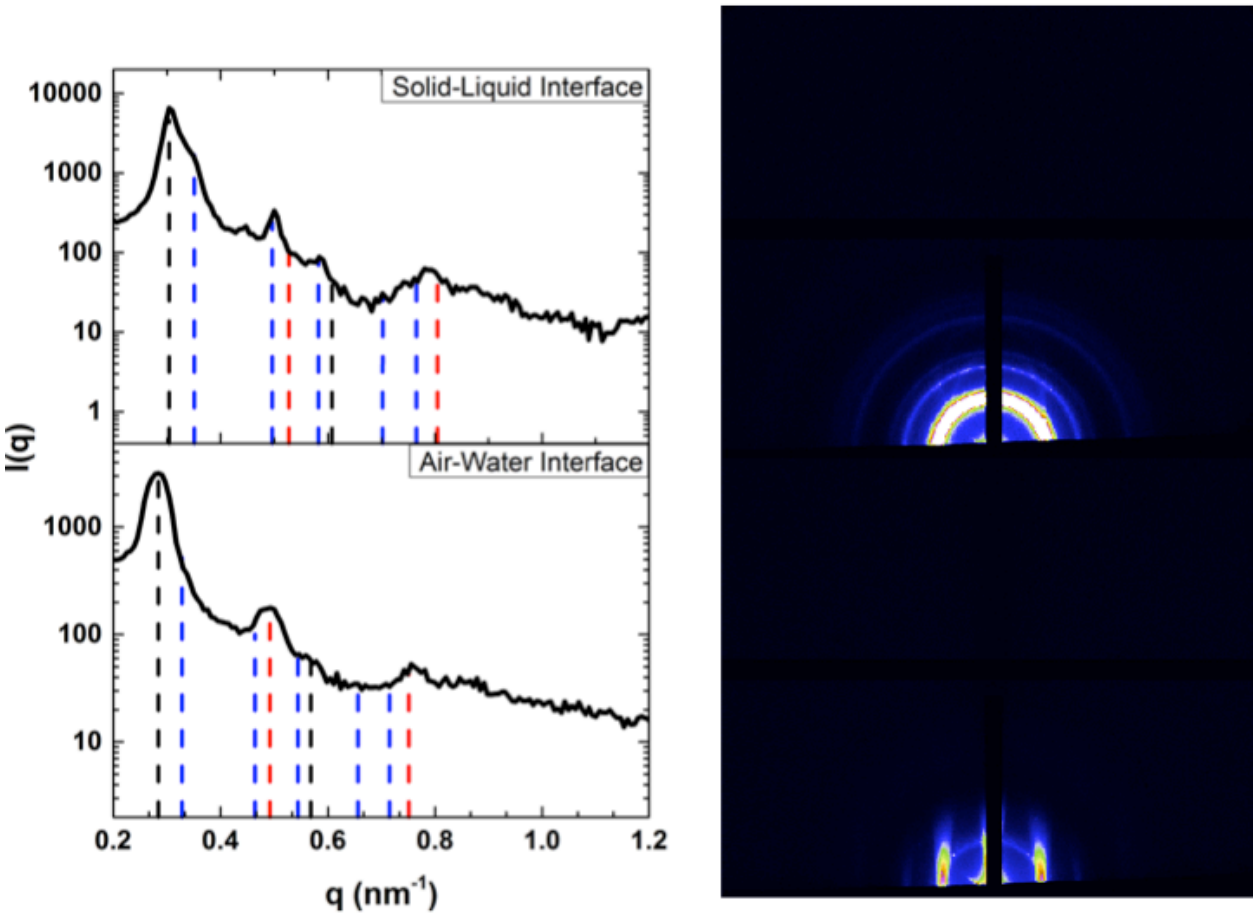

Figure 3. 12: 1D and 2D scattering spectra from the solid-liquid interface (top) and the air water interface (bottom) for T30 DNA-AuNPs at 2400 mM. The difference in 2D and 3D structure is noted in the 2D scattering spectra (right) whereby the rods are indicative of a two dimensional orientation and the scattering rings of three-dimensional order. This is further demonstrated in the 1D scattering (left) where the dashed lines indicate the peak position of the 3D FCC (blue) and 2D hexagonal (red). Peaks indicated by the dashed black lines are peaks where the position is the same in both the FCC and hexagonal lattice.

3.4 DISCUSSION

The results presented herein reveal a simple, solution based nanoparticle crystallization method. This method can be used to reliably prepare 3D nanoparticle crystals without the need

for extensive DNA design. Additionally, the crystal properties can be easily varied by tuning several parameters. The interparticle spacing was changed from ~24 nm to ~30 nm by selecting longer or shorter DNA ligands. Ligand length, among the conditions tested, provides coarse tunability with respect to interparticle distance; a change in DNA length of 15 bases corresponded to ~2 nm in length. Salt concentration, on the other hand, provided a finer ruler, with a change in 150 mM ionic strength resulting in approximately 1 nm change in spacing. Not only was solution ionic strength fundamental to the properties of the crystal produced, the species of salt used was of equal importance. Here, both $CaCl_2$ and $MgCl_2$ were shown to produce 3D nanoparticle crystals, though crystal attributes depended on the choice of salt species. FCC crystals formed from 1500-2400 mM in $MgCl_2$, while $CaCl_2$ solutions only produced 3D crystals at much lower conenctration, 600 mM ionic strength. However the crystallites displayed longer range order in $CaCl_2$.

Surprisingly, these same parameters afforded control over the type of crystal lattice produced- the solution ionic strength enabled switching between 3D HCP and FCC lattices. At all but the highest ionic strengths tested, 2400 mM $MgCl_2$, HCP lattices existed in solution. At 2400 mM $MgCl_2$ scattering spectra throughout the droplet indicated that the only 3D crystals formed were FCC crystals, which were found exclusively at the solid-liquid interface. This leads to an important finding about the solution dynamics of the DNA-AuNPs tested; the precipitation mechanism by which the crystallites are formed proceeds through crystal rearrangement. That is, at the lower ionic strengths the crystals are exclusively HCP (Figure 3. 9) but as the salt concentration increases these crystals become FCC. Although the energies of both crystal structures are similar, the FCC has a slightly lower energy than that of the HCP and would thus generally be favored.[11] However as has been found with DNA-AuNPs of base pairing

functionality, growing crystallites undergo a transition from HCP to FCC. While the grain sizes in Table 3. 1, do not necessarily agree with this, growing crystallites will rearrange to a denser packing, which is consistent with the smaller interparticle spacing seen at higher ionic strength[12]. It is hoped that future experiments can further address this question.

The utility of our lab's previous nanoparticle assembly method [5] has here been demonstrated to be extendable to three dimensions. Unfortunately, the applicability of a sessile droplet is still limited. In order to be used in plasmonic and electronic applications the crystals described herein would ideally be able to be transferrable to multiple surfaces and withstand a variety of conditions. The next chapter will describe our progress towards these goals

REFERENCES

1. Macfarlane, R. J.; Lee, B.; Jones, M. R.; Harris, N.; Schatz, G. C.; Mirkin, C. A., Nanoparticle superlattice engineering with DNA. *Science* **2011,** *334* (6053), 204-8.

2. Jones, M. R.; Macfarlane, R. J.; Lee, B.; Zhang, J.; Young, K. L.; Senesi, A. J.; Mirkin, C. A., DNA-nanoparticle superlattices formed from anisotropic building blocks. *Nat Mater* **2010,** *9* (11), 913-7.

3. Nykypanchuk, D.; Maye, M. M.; van der Lelie, D.; Gang, O., DNA-guided crystallization of colloidal nanoparticles. *Nature* **2008,** *451* (7178), 549-52.

4. Liu, W.; Tagawa, M.; Xin, H. L.; Wang, T.; Emamy, H.; Li, H.; Yager, K. G.; Starr, F. W.; Tkachenko, A. V.; Gang, O., Diamond family of nanoparticle superlattices. *Science* **2016,** *351* (6273), 582-6.

5. Tan, S. J.; Kahn, J. S.; Derrien, T. L.; Campolongo, M. J.; Zhao, M.; Smilgies, D. M.; Luo, D., Crystallization of DNA-capped gold nanoparticles in high-concentration, divalent salt environments. *Angew Chem Int Ed Engl* **2014,** *53* (5), 1316-9.

6. Smilgies, D. M., Scherrer grain-size analysis adapted to grazing-incidence scattering with area detectors. *J Appl Crystallogr* **2009,** *42* (Pt 6), 1030-1034.

7. Forster, S.; Timmann, A.; Konrad, M.; Schellbach, C.; Meyer, A.; Funari, S. S.; Mulvaney, P.; Knott, R., Scattering curves of ordered mesoscopic materials. *J Phys Chem B* **2005,** *109* (4), 1347-60.

8. Kewalramani, S.; Guerrero-Garcia, G. I.; Moreau, L. M.; Zwanikken, J. W.; Mirkin, C. A.; Olvera de la Cruz, M.; Bedzyk, M. J., Electrolyte-Mediated Assembly of Charged Nanoparticles. *ACS Cent Sci* **2016,** *2* (4), 219-24.

9. Hill, H. D.; Macfarlane, R. J.; Senesi, A. J.; Lee, B.; Park, S. Y.; Mirkin, C. A., Controlling the lattice parameters of gold nanoparticle FCC crystals with duplex DNA linkers. *Nano Lett* **2008,** *8* (8), 2341-4.

10. Smilgies, D. M.; Heitsch, A. T.; Korgel, B. A., Stacking of hexagonal nanocrystal layers during Langmuir-Blodgett deposition. *J Phys Chem B* **2012,** *116* (20), 6017-26.

11. Woodcock, L. V., Entropy difference between the face-centred cubic and hexagonal close-packed crystal structures. *Nature* **1997,** *385* (6612), 141-143.

12. Macfarlane, R. J.; Lee, B.; Hill, H. D.; Senesi, A. J.; Seifert, S.; Mirkin, C. A., Molecular recognition and self-assembly special feature: Assembly and organization processes in DNA-directed colloidal crystallization. *Proc Natl Acad Sci U S A* **2009,** *106* (26), 10493-8.

CHAPTER FOUR:

TOWARDS THE APPLICATION OF DNA-CAPPED GOLD NANOPARTICLE SUPERLATTICES

4.1: BACKGROUND

Nanoparticle crystallites exhibit many unique properties distinct from both the bulk material and the individual nanoparticle due to the collective interactions within their assemblies[1]. For example, the optical properties of superlattices of gold nanoparticles can be tuned based on both the nanoparticle distance and the crystal structure[2]. It can be envisaged that such materials could be used to realize tailor-made optoelectronic devices. However, integration into semiconductor devices requires that these materials be integrated onto semiconductor surfaces. Our group's aforementioned interfacial 2D superlattices greatly extend the ionic environment in which nanoparticle crystals can exist[3], but at the same time is limited by its aqueous environment. Not only is the aqueous environment precisely controlled in the experiments, but the use of the superlattice is limited by its interfacial confinement.

Here, the robustness of the droplet system is explored. A facile technique for the interfacial transfer of nanoparticle superlattices is demonstrated. By exploiting the electrostatic affinity of DNA-capped gold nanoparticles and positively charged silicon surfaces, it is shown that crystallites existing at the air-water interface can be readily transferred with high fidelity to a silicon substrate. Secondly, it is shown that by simply allowing the sessile droplet to equilibrate outside of the previously used environmental chamber, not only does the droplet not dry, but also the interfacial monolayer increases in grain size.

4.2 MATERIALS AND METHODS

4.2.1 Synthesis of DNA-capped Gold Nanoparticles

Gold nanoparticle DNA conjugates were synthesized as described in section 2.2.1. Similar length sequences were used, that is polythymine oligonucleotides of varying length, T10,

T30, T45, and T60. However, multiple sizes of gold nanoparticles were used.

4.2.2 *Interfacial Transfer of Gibbs Monolayers*

The transfer process is facilitated by the electrostatic adsorption of highly negatively charged DNA-AuNPs on a positively charged APTES surface. The APTES functionalization was achieved by the first incubating an approximately 1 x 1 cm cleaned silicon wafer substrate overnight in a 2% APTES solution prepared in 95% ethanol. After rinsing in pure ethanol followed by a rinsing in isopropanol, the silicon was baked at 95 °C for 1 hour followed by another rinsing cycle.

Interfacial transfer was subsequently achieved by preparing a 1-2 µL droplet containing 250 nM DNA-AuNPs and the appropriate amount of salt solution on a cleaned silicon substrate, resulting in a well ordered Gibbs monolayer. Tweezers were then used to lightly press an inverted APTES functionalized substrate onto the Gibbs monolayer. The substrate was then immediately withdrawn and quickly rinsed in three separate containers of deionized water followed by drying with a gentle stream of air (Figure 4. 1).

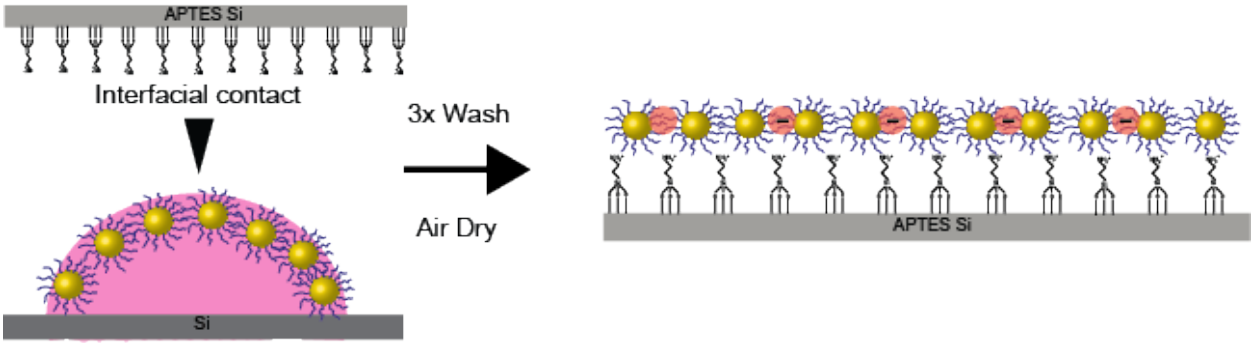

Figure 4. 1: Process for transferring ordered Gibbs monolayers to APTES functionalized silicon substrate

4.2.3 Small Angle X-ray Scattering Experiments

SAXS experiments were conducted at the D1 experimental station at the Cornell High Energy Synchrotron Source (CHESS). The Pilatus 200k detector was employed under the same conditions as in section 3.2.2. Individual scattering spectra were again obtained first in the sample environment chamber as previously described. Samples were then removed and allowed to equilibrate on the benchtop for at least one hour before new scattering spectra were obtained in the chamber without placement of the lid, exposing the droplet to the lab environment.

4.2.5 X-ray Data Analysis

Analysis and interpretation of the SAXS data was conducted according to the analyses described in section 3.2.3. As the spectra obtained indicated monolayer structure, the analysis focused on the two-dimensional hexagonal lattice described by equation 3.7.

4.2.6 Scanning Electron Microscopy

Scanning electron micrographs of the dried transferred superlattices were obtained on a LEO 1550 FESEM, in Clark Hall on Cornell University Campus. Data was extracted from the micrographs using a combination of ImageJ and R, both freely available. To measure the interparticle (center-to-center) distances, the ImageJ line tool was used to count the number of pixels between nanoparticles, and subsequently converted to nanometers using the scale bar of the image to determine a pixel:nm ratio. Radial distribution functions were calculated by first using the ImageJ particle analysis tool obtain the pixel coordinates of the center of each nanoparticle in the images. These coordinates were then imported into R, where native functions were employed to calculate the radial distribution functions.

4.3 RESULTS

4.3.1 Electrostatically Assisted Superlattice Transfer

The lattice transfer method described above, although rudimentary, yielded consistent, repeatable results using the nanoparticles optimized for long range ordered Gibbs monolayers.[3] The technique facilitated the superlattice transfer of all but the shortest DNA-AuNPs tested. Specifically, nanoparticles with T30, T45, and T60 ligands all resulted in hexagonally oriented nanoparticle superlattices with long range order. The resultant superlattices on APTES silicon is shown in Figure 4. 2, Figure 4. 3, and Figure 4. 4 for the T30, T45, and T60 DNA-AuNPs, respectively. In all of the micrographs clear evidence is seen of the two-dimensional hexagonal arrangement. Another interesting attribute shared between the superlattices is the appearance of defects in the form of nanoparticle "holes", whereby a nanoparticle is missing from the center of a hexagonal packing arrangement. There are of course, more significant defects, such as "holes" with more than one nanoparticle vacancy.

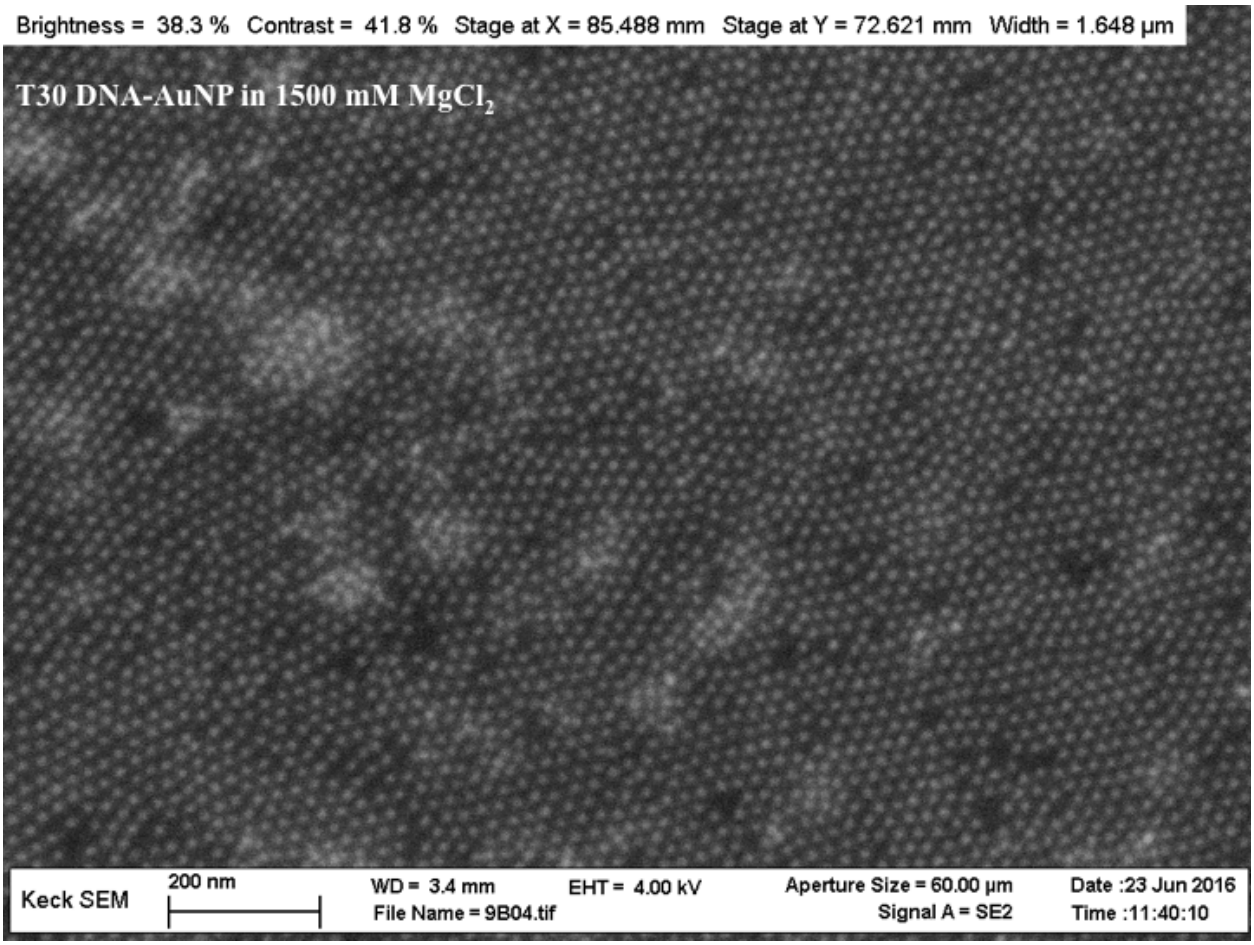

Figure 4. 2: T30 DNA-AuNP superlattice prepared in a 1500 mM $MgCl_2$ and transferred onto APTES functionalized Silicon.

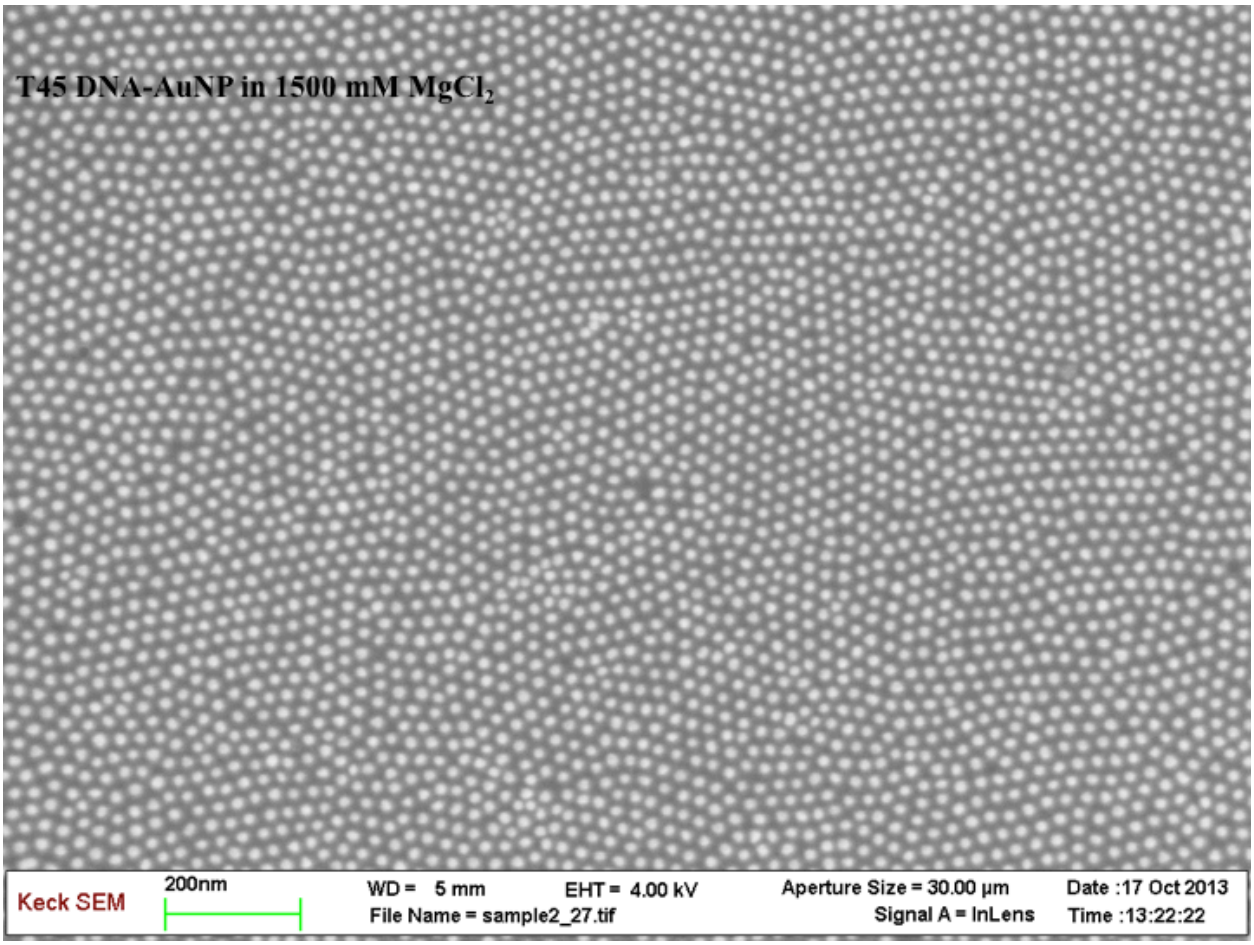

Figure 4. 3: T45 DNA-AuNP superlattice prepared in 1500 mM $MgCl_2$ and transferred to APTES functionalized silicon.

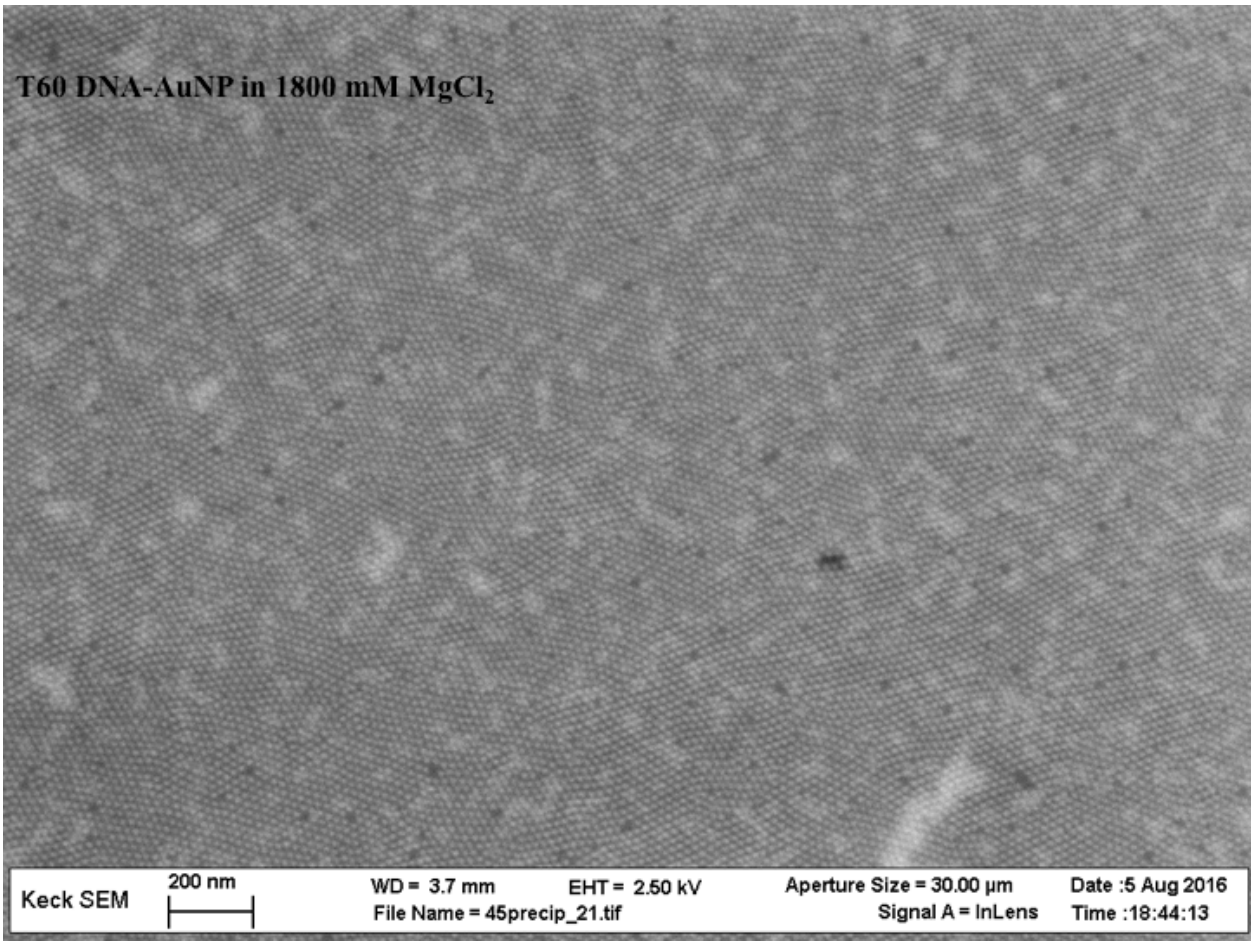

Figure 4. 4: T60 DNA-AuNP superlattice prepared in 1800 mM $MgCl_2$ and tranferred to APTES functiionalized silicon.

Despite the existence of imperfections the superlattices of the DNA-AuNPs tested were of high quality. Elementary quantitative analyses of the superlattices were performed by plotting radial distribution functions of the micrographs shown above. In its simplest terms, the radial distribution function describes the probability of finding a particle at a distance r away from a reference particle. The radial distribution functions are shown in Figure 4. 5A, B, and C, for the T30, T45, and T60 DNA-AuNPs, respectively. The plots show a high degree of correlation over a ~200 nm area, with the T60 DNA-AuNPs (Figure 4. 5) exhibiting, the highest primary peak, though this may be due to the larger amount of nanoparticles present in the obtained images.

Fourier transforms were taken over a 200 x 200 nm area in each micrograph (Figure 4. 5, D-F) as well as over the entire image (Figure 4. 5, G-I). The discrete dot patterns of the Fourier transforms over the smaller area clearly indicate a directional orientation of the hexagonal arrangements, however, when taken over the entire image, this orientational preference is lost. This can be seen by the dots' disappearance and the appearance of rings, indicating no directional orientation. More evidently, this can be seen in the corresponding SEM images, where lattice grains can be observed to have preferred orientation. These grain sizes can be visually estimated to be on the order of 250-300 nm. Much smaller than the grain sizes previously measured from air-water interface data,[3] which may be accounted for by drying effects. Analogous to the 3D crystals from the previous chapter and our labs air-water interface data, the spacing was controlled by the length of the nanoparticle ligand. The shortest, T30 ligands resulted in an interparticle distance of 19.8±1.0 nm, the intermediate T45 ligands, 22.9±0.8nm, and finally the longest T60 ligands, 23.8±0.6 nm.

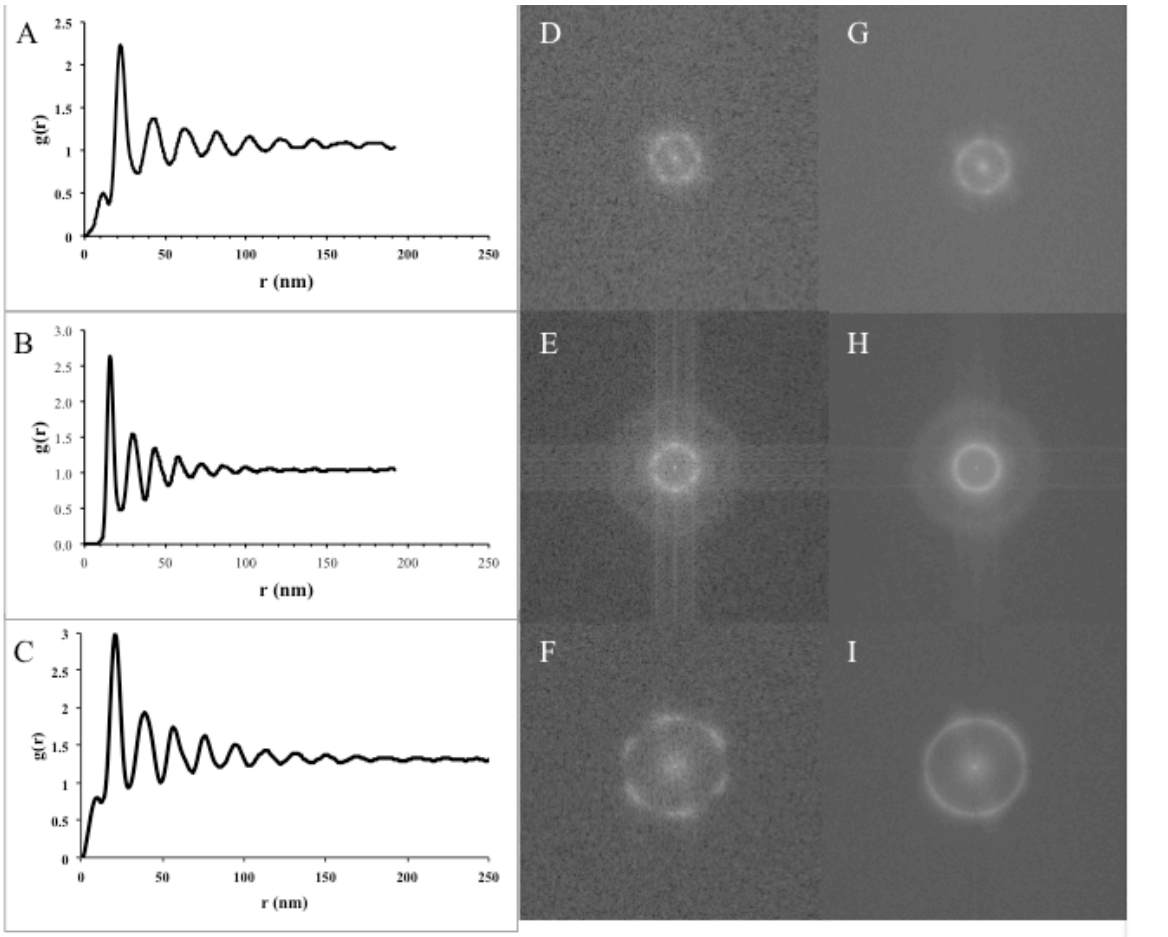

Figure 4. 5: Radial distribution functions of the A) T30 DNA-AuNPs, B) T45 DNA-AuNPs, and the T60 DNA-AuNPs above, shown alongside the corresponding Fourier transform over (D-F) a ~200 x 200 nm area as well as (G-I) over the entire image.

The above solutions have been optimized for interfacial transfer ~15 nm gold nanoparticles. Under similar conditions, larger nanoparticles, 30 nm in diameter were not found to result in transferrable ordered monolayers. This may be due to the difficulty in obtaining high concentration large diameter nanoparticles; the stock solutions are orders of magnitude more dilute. On the other hand, smaller nanoparticles, of 5 nm diameter, do seem amenable to the interfacial superlattice transfer technique. Figure 4. 6 shows the superlattice formed in 1800 mM

$MgCl_2$ for 5 nm diameter gold nanoparticles with a T30 DNA ligand. While clearly not as ordered as with the larger diameter nanoparticles, the smaller nanoparticles do show a hexagonal arrangement, albeit with lower grain sizes on the order of ~200 nm. The lower monodispersity of the smaller diameter nanoparticles, which can be seen in the image likely contributed to this reduction in quality. The interparticle spacing, 20.3±0.7 nm, as dictated by the ligand corresponds well to the spacing measured with the 15 nm particles. 19.8±1.0 nm. The slight increase in the spacing with the smaller nanoparticles may be a result of the lower van der Waals forces between smaller particles[4], resulting in a smaller attractive force between the nanoparticles.

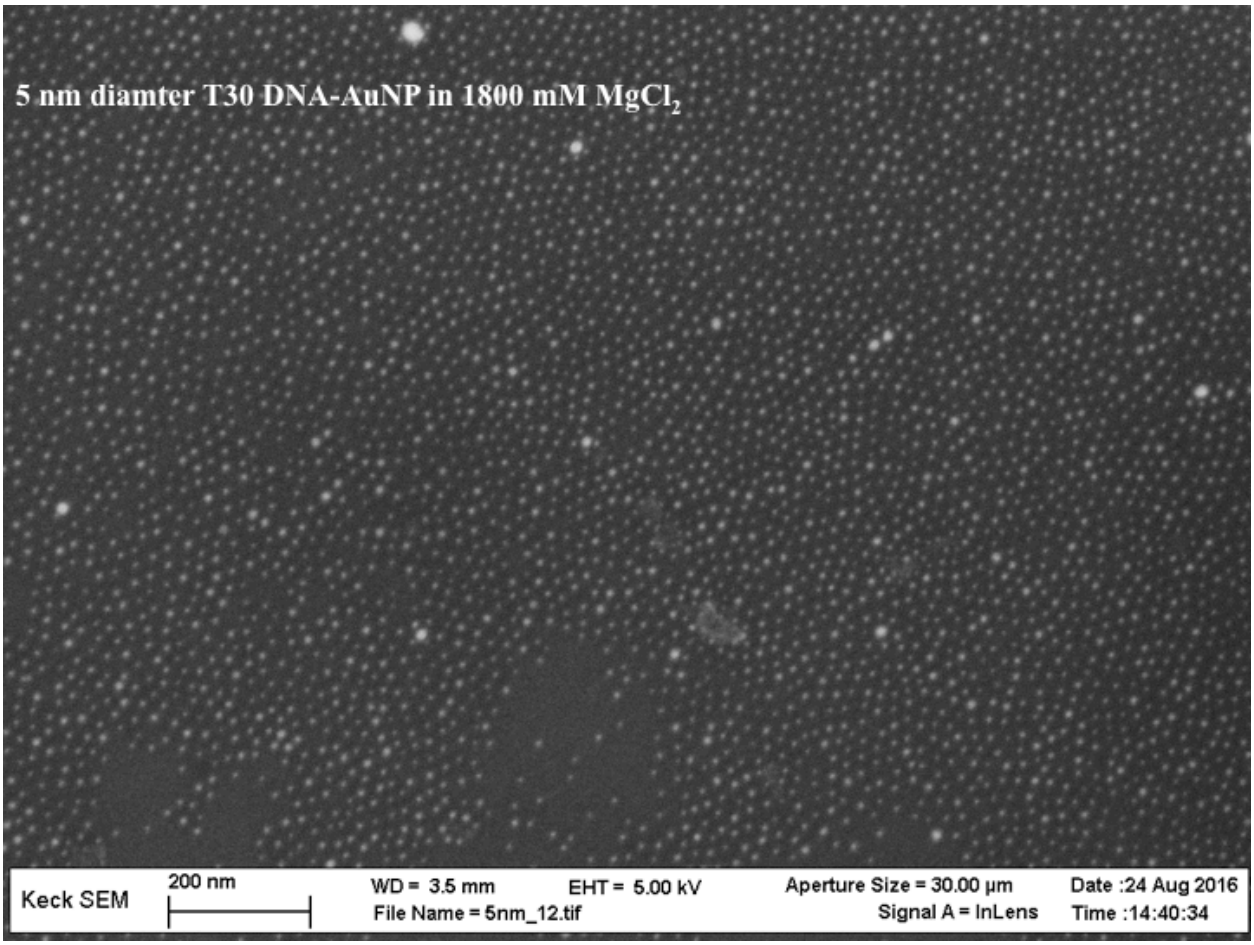

Figure 4. 6: A superlattice prepared from 5 nm diameter T30 DNA-AuNPs in 1800 mM $MgCl_2$ and transferred to an APTES functionalized silicon substrate.

4.3.2 Stability of Gibbs Monolayers in an Uncontrolled Environment

The above superlattice transfer technique successfully demonstrated the extension of the Gibbs monolayers from the air-water interface to the solid interface, not only allowing the superlattices to be stored indefinitely but also integrated into traditional silicon based devices. The move away from the liquid droplet facilitates further processing of the nanoparticle crystallites, however the liquid crystallites still provide the highest ordered assemblies, and are free of any defects imposed by the drying process. Unfortunately the stability of liquid droplets themselves are subject to ambient conditions, most often resulting in drying. Here it is shown

that due to the high concentration of $MgCl_2$ in solution the liquid droplet is only subject to limited drying processes and that this small amount of drying results in an increase in crystalline order. The result is a pseudo-stable droplet that after equilibrating to the ambient environment remains stable for months, enabling the droplet to be incorporated into devices previously inaccessible.

The apparent stability of the droplet stems from the deliquescent property of aqueous salt solutions; above a threshold relative humidity level salt solutions will absorb moisture from the air.[5] In previous studies on aqueous droplets sealed environmental sample chambers were employed (see Chapter 3), with a reservoir of equal salt concentration to that of the droplet, thereby ensuring the relative humidity of the droplet and reservoir were equal, so that no drying of the droplet occurs. In the experiments described herein the droplets were first allowed to equilibrate to the ambient atmosphere for at least an hour and then scattering images were obtained without sealing the sample chamber. An example raster scan of a droplet in a sealed chamber and then after equilibration to the ambient conditions can be seen in Figure 4. 7. Before equilibration (top) the droplet was prepared using T30 DNA-AuNPs in a 600 mM $MgCl_2$ ionic strength solution. For saturated $MgCl_2$ solutions the critical relative humidity occurs at ~30%. After equilibrating on the benchtop the droplet showed considerable shrinkage but did not dry (Figure 4. 7-bottom). Note the small amounts of scattering seen in the upper half of the droplet scan of the equilibrated droplet. This is due to the finite beam dimensions (0.3 x 0.2 mm), which are larger than step size employed in the scans, contributing to scattering, although the beam center may be above the droplet. This partial drying, consistently occurred for the droplets in $MgCl_2$, all the while remaining stable for months.

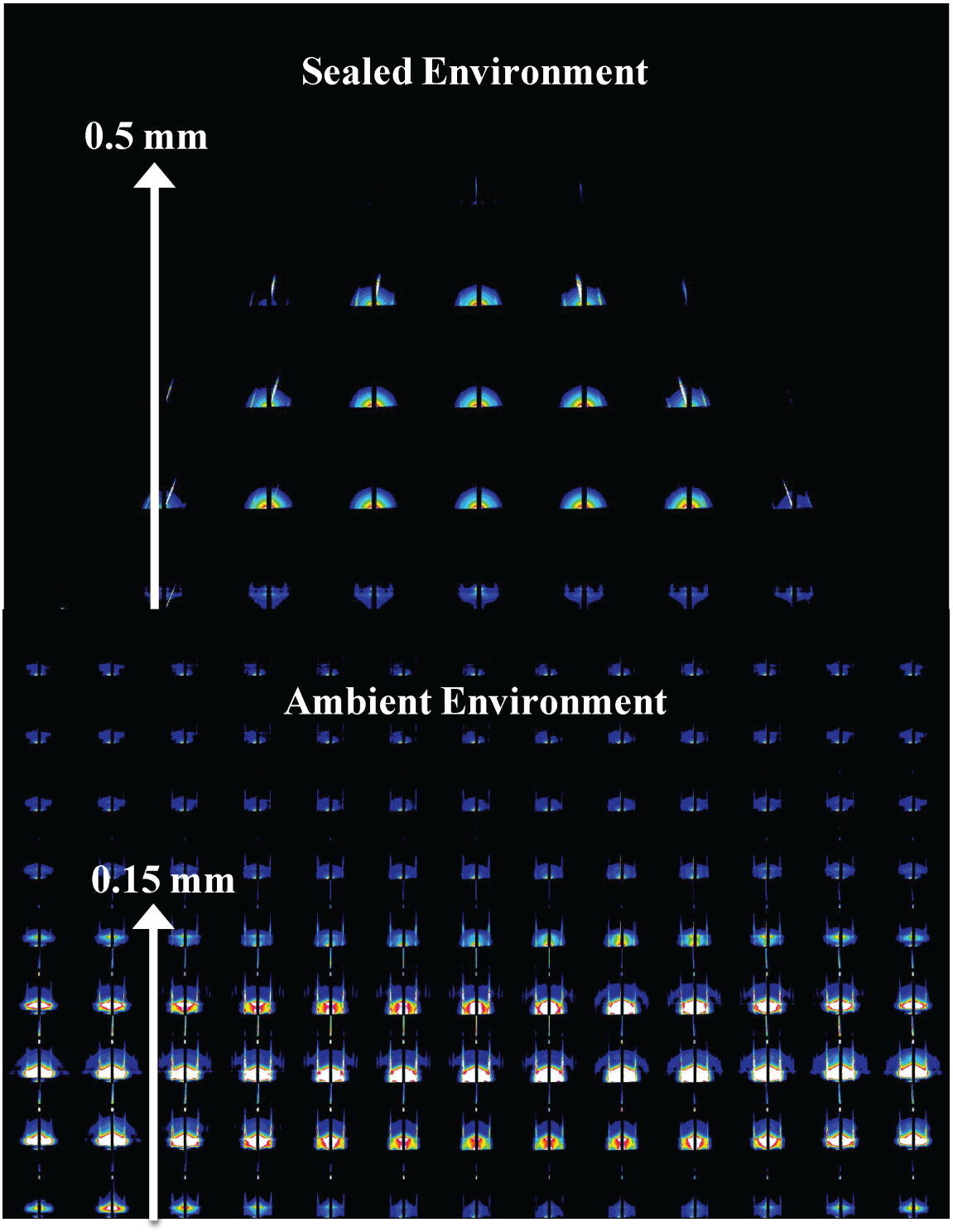

Figure 4. 7: A droplet of T30 DNA-AuNPs in 600 mM $MgCl_2$ in top) sealed environemental sample chamber, thus avoiding any drying and bottom) open to the ambient environment, after equilibration, involving incomplete droplet drying, as evidenced by the reduction in droplet size.

The reduction in droplet in size was accompanied by a dramatic increase in the long range order of the Gibbs monolayers. In the initial, humidity controlled environment, only weak first ordered peaks were visible in the scattering spectrum. Remarkably, after ambient equilibration, distinct fourth order peaks were observed (Figure 4. 8). Though a slight increase in order may be expected from the increase in ionic strength due to the droplet shrinkage, the extent of the increase is much greater than previously recorded.[3]

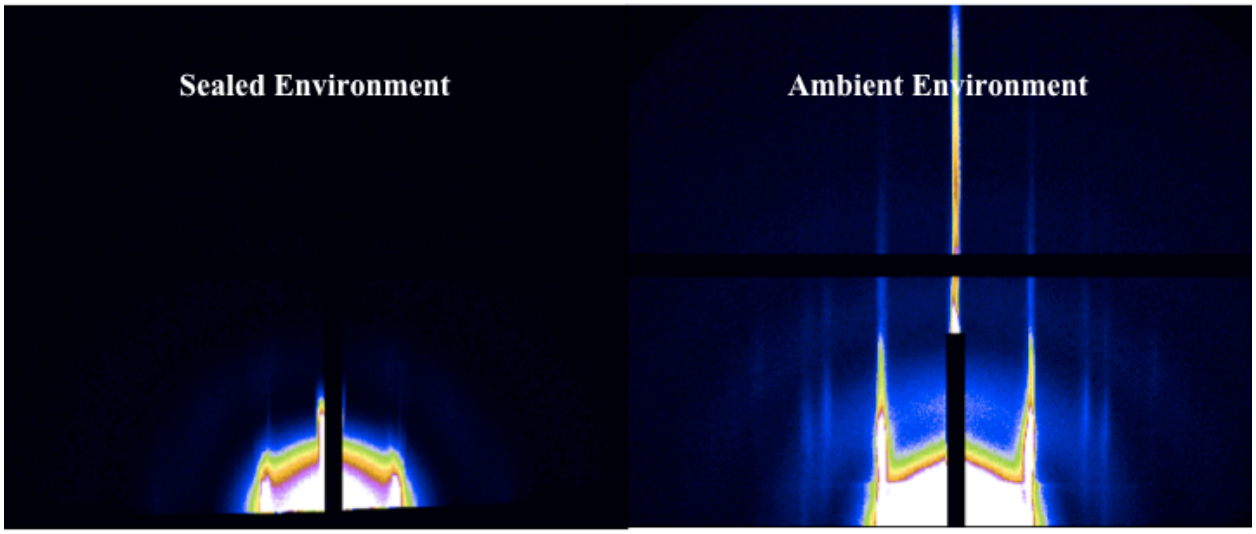

Figure 4. 8: Superlattices formed at the air-water interface of the left) droplet in the sealed environmental sample chamber and right) after equilibration. Here, the increase in higher order peaks as well peak narrowing, indicating larger grain sizes with longer-range order after equilibration can be seen.

In relation to the increase in long range order an equivalent increase in the crystallite grain size was recorded. For both the T30 and T60 DNA ligands, a more than doubling of the grain size was detected. In the sealed environmental chamber, the T10 DNA-AuNPs assembled into crystallites of 220 nm, after ambient equilibration this increased more threefold to 750 nm. Similarly, the T30 DNA-AuNPs increased from 225 nm to 620 nm. The increase in grain size can be seen as first order peak narrowing in the integrated spectra shown in Figure 4. 9 for the T30 DNA-AuNPs and in Figure 4. 10 for the T10 DNA-AuNPs. The plots also show that the grain size increase was combined with a decrease in the interparticle spacing- the first order peak of sealed droplets, shown by the black traces, occurred at lower *q* values than ambient doplets, shown by the blue traces. For the T30 DNA-AuNPs this corresponded to a shift from 27.4 nm to 24.2 nm, and from 21.6 to 19.9 nm for the T10 DNA-AuNPs shown in Figure 4. 9 and Figure 4. 10.

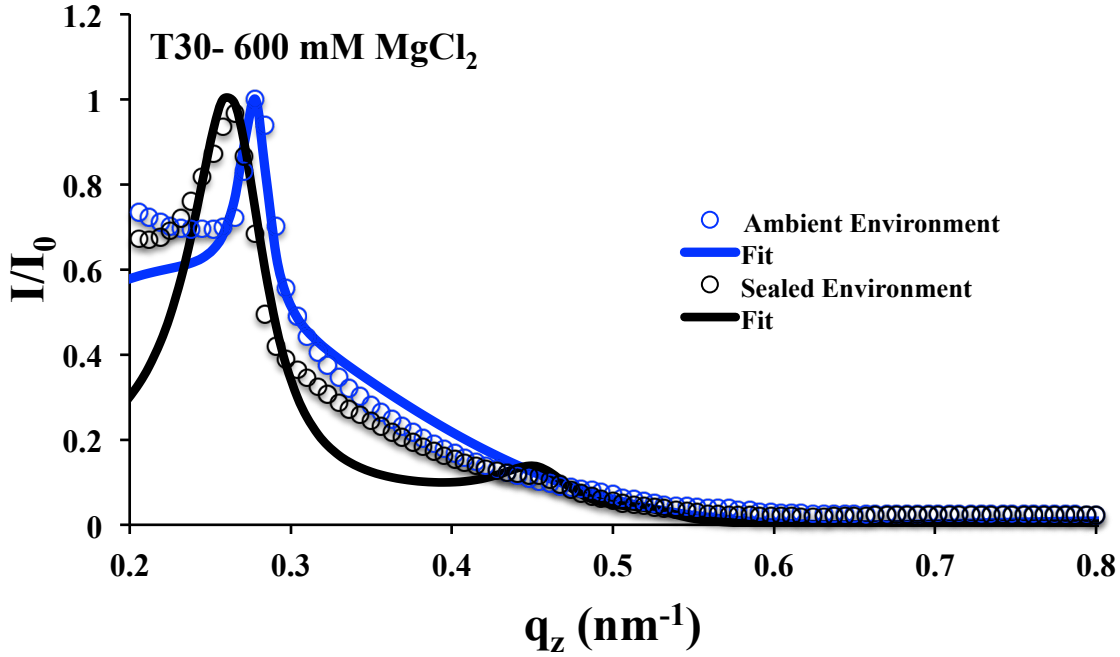

Figure 4. 9: Normalized experimental data (open circles) and the fit used to calculate the grain sizes (lines) from the sealed sample (black) and after ambient equilibration (blue) for the T30 DNA-AuNPs at 600 mM $MgCl_2$.

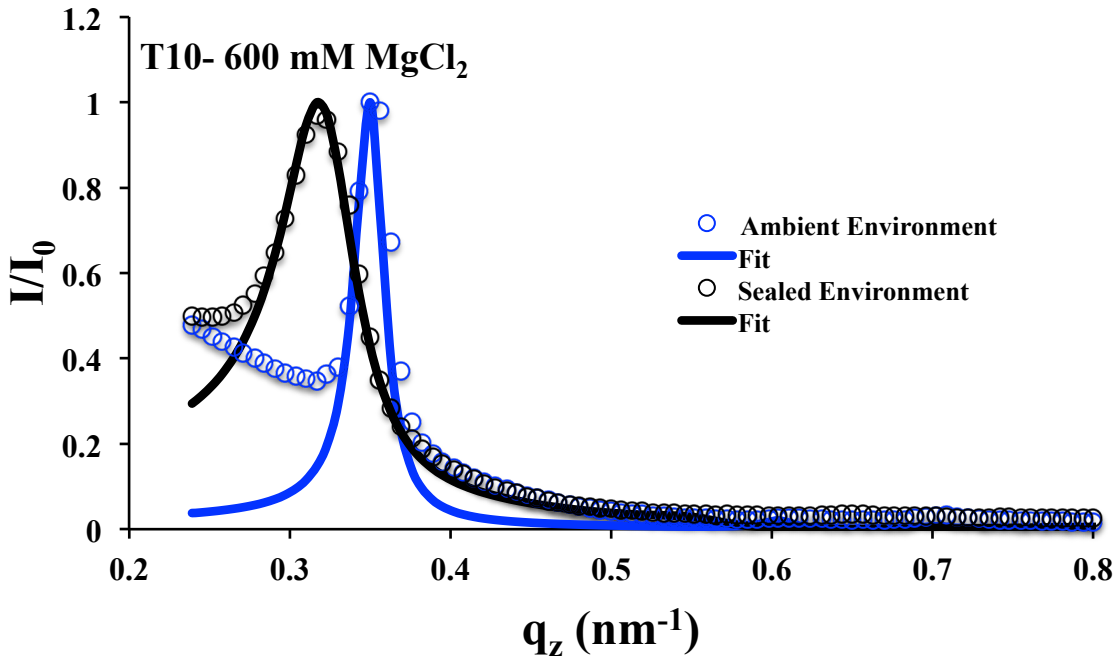

Figure 4. 10: Normalized experimental data (open circles) and the fit used to calculate the grain sizes (lines) from the sealed sample (black) and after ambient equilibration (blue) for the T10 DNA-AuNPs at 600 mM $MgCl_2$.

Droplets were also prepared and equilibrated at $MgCl_2$ ionic strengths of 150, 300, and 750 mM for both the T10 (Figure 4. 11) and T30 (Figure 4. 12) ligands (however, without scanning in the sealed environment, due to time constraints). The maximum grain sizes were obtained at the 600 mM concentration shown above, though comparable results were achieved at 300 mM for the T10 DNA-AuNPs (Figure 4. 11B, F) and 750 mM for the T30 DNA-AuNPs (Figure 4. 12D, H). The integrated spectra (E-H) are shown in the figures, where relative peak heights can be more easily discerned. For both nanoparticle ligands third order peaks and above

are seen for all $MgCl_2$ above 150 mM. At 150 mM, however, only medium range order is observed, as ascertained by only the presence of second order peaks. The results of the grain sizes and nanoparticle spacings are summarized in Table 4. 1. Once again, interparticle distance can be tuned by changing the initial ionic strength of the solution, with higher ionic strength resulting in smaller distances. What this also demonstrates though, is that if as previously thought, among DNA-AuNPs with the same ligands, the interparticle distance is controlled by the solution ionic strength alone, the droplets are not drying to the same equilibrium ionic strength. Clearly, more data is needed, which specifically addresses the ambient relative humidity, to further explore this.

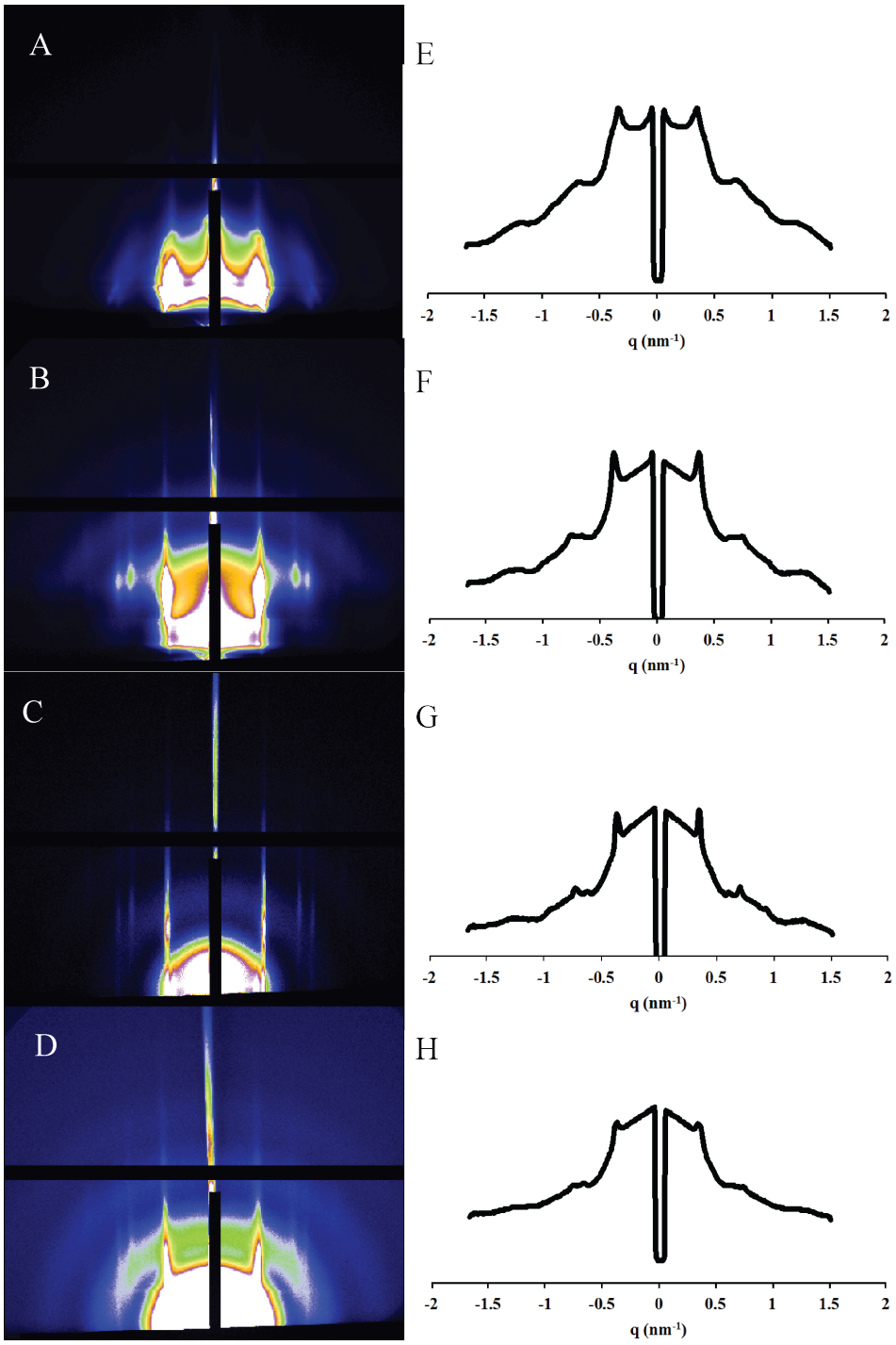

Figure 4. 11: (Left) 2D scattering spectra of droplets of T10 DNA-AuNP at A) 150 mM, B) 300 mM, C) 600 mM and D) 800 $MgCl_2$ alongside the (right) 1D integrated spectra (E-H) after ambient equilibration.

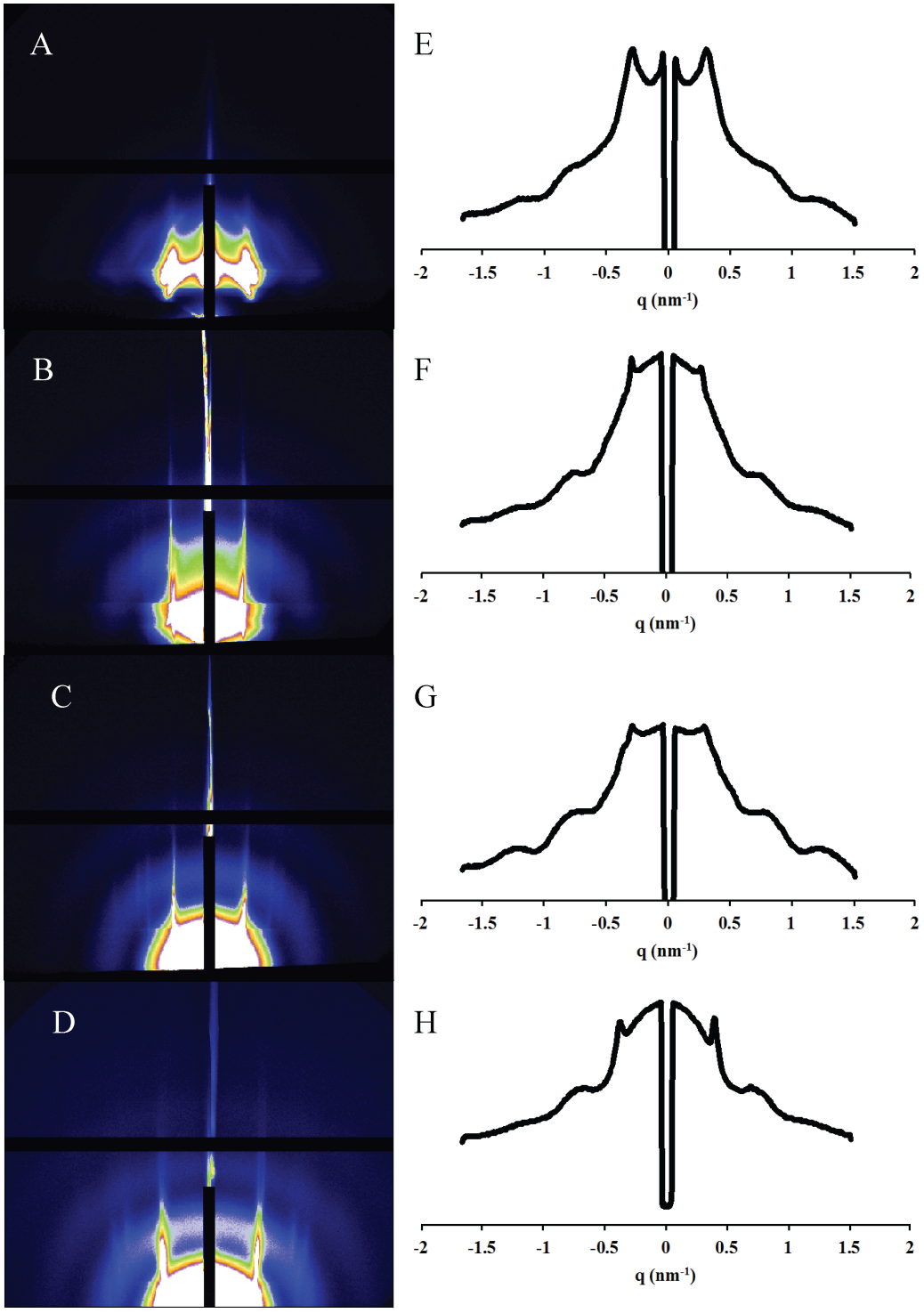

Figure 4. 12: (Left) 2D scattering spectra of droplets of T30 DNA-AuNP at A) 150 mM, B) 300 mM, C) 600 mM and D) 800 $MgCl_2$ alongside the (right) 1D integrated spectra (E-H) after ambient equilibration.

Table 4. 1: Summary of spacing data of equilibrated droplets for both T10 and T30 DNA-AuNPs at various ionic strengths.

	MgCl2 Ionic Strength (mM)				
Sample	**150**	**300**	**600**	**750**	
	292	410	750	160	**Grain Size (nm)**
T10	21.6	19.3	19.9	19.6	**Spacing (nm)**
	116	194	626	490	**Grain Size (nm)**
T30	25	24.9	24.4	19.3	**Spacing (nm)**

4.4 DISCUSSION

With a hope to integrate our lab's two-dimensional DNA-AuNP superlattices into functional devices two general strategies were presented above to facilitate this application. It is envisioned that by extending the environments in which the superlattices can be made, progress will be made towards this goal. Transfer of the air-water interfacial superlattice to a solid substrate is instrumental to integration into semiconductor devices. Furthermore, the simplicity of the transfer technique lends itself to the application in a wide variety of materials. Though so far efforts to use larger nanoparticles have not yielded consistent results, the initial results with the smaller diameter nanoparticles are promising, and other morphologies such as nanorods and prisms can be imagined. Of critical importance is the underlying electrostatic phenomena governing the process; the highly negatively charged DNA-AuNPs are rapidly and strongly adsorbed to the positively charged surface. Though the inherent properties of DNA such as sub-nanometer length precision, charge density, and persistence length certainly contribute to the

success of this technique, the above data can serve as a starting point from which to assemble many other materials.

The ability to stabilize the droplet in ambient environments can serve to further the goal of extending the utility of the superlattices. By preserving crystallites in their native environment no drying effects contribute to crystalline defects. Equivalently, the solution phase allows for a more dynamic environment, where factors such as pH, ionic strength, and solute species can be varied. Moreover, by allowing the droplet to equilibrate to ambient environments, the grain size can be considerably enlarged by more than three times in the best cases. Interestingly, as can be seen by the presence of only vertical rods in Figure 4. 7, the superlattice shows no directional preference. While exciting, more quantitative data including relative humidity is needed to fully optimize the droplet system described. Immediately, however, the stability of the droplets allows for a wide range of applications of this previously unexplored platform. Indeed, as shown by the two month old droplets pictured in Figure 4. , the droplets remain liquid for months. Perhaps more significantly, the superlattices clearly retain their plasmonic properties, and can even rehydrate themselves within minutes (Figure 4. C)!

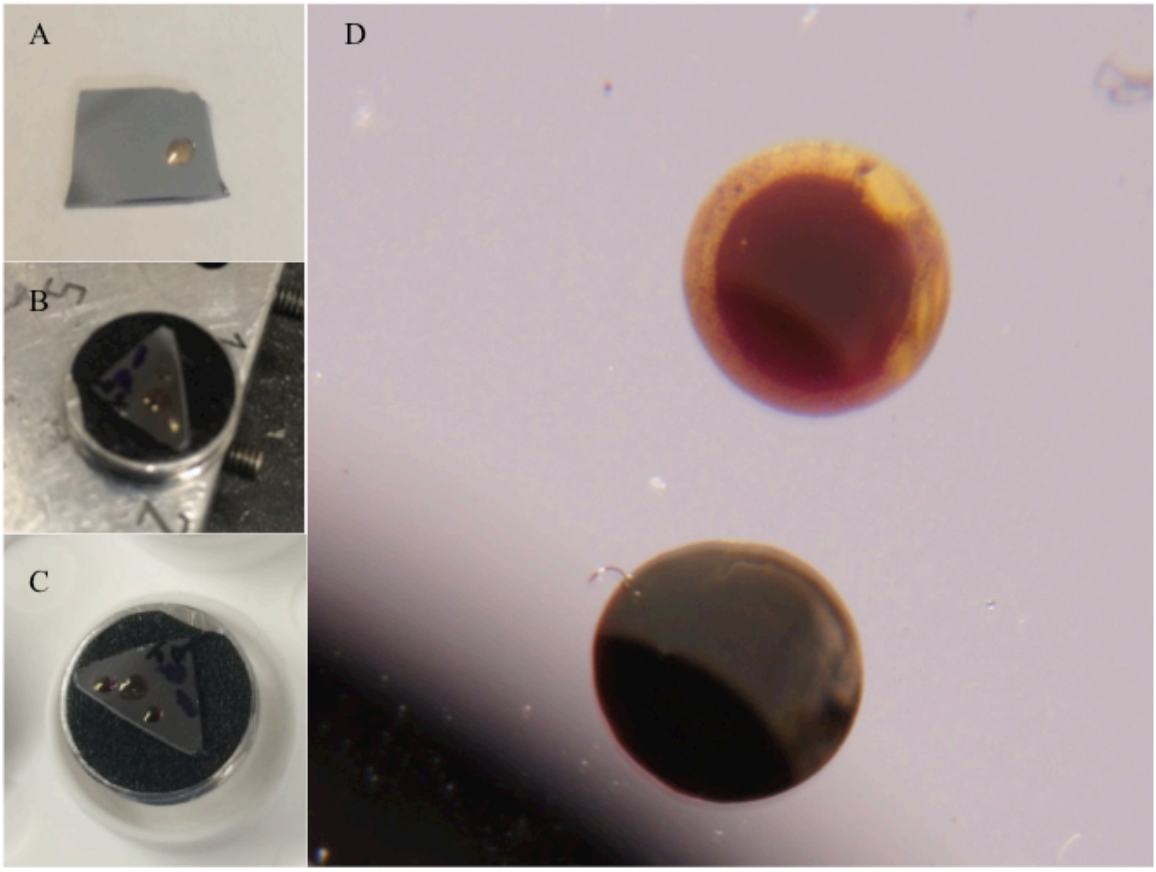

Figure 4. 13: DNA-AuNP droplets prepared on silicon substrates and left on the benchtop for two months. A) T10 DNA-AuNP at 200 mM $MgCl_2$, B) vacuum dried T30 DNA-AuNPs at 800 mM $MgCl_2$ and then C) after re-equilibrating in an ambient environment. D) Droplets were also prepared under the same conditions as A) but with different nanoparticle concentrations, 200 (top droplet) vs 300 nM nanoparticle concentrations.

REFERENCES

1. Tan, S. J.; Campolongo, M. J.; Luo, D.; Cheng, W., Building plasmonic nanostructures with DNA. *Nat Nanotechnol* **2011,** *6* (5), 268-76.

2. Ross, M. B.; Ku, J. C.; Vaccarezza, V. M.; Schatz, G. C.; Mirkin, C. A., Nanoscale form dictates mesoscale function in plasmonic DNA-nanoparticle superlattices. *Nat Nanotechnol* **2015,** *10* (5), 453-8.

3. Tan, S. J.; Kahn, J. S.; Derrien, T. L.; Campolongo, M. J.; Zhao, M.; Smilgies, D. M.; Luo, D., Crystallization of DNA-capped gold nanoparticles in high-concentration, divalent salt environments. *Angew Chem Int Ed Engl* **2014,** *53* (5), 1316-9.

4. Hamaker, H. C., The London - Van Der Waals attraction between spherical particles. *Physica* **1937,** *4*, 1058-1072.

5. Greenspan, L., Humidity Fixed-Points of Binary Saturated Aqueous-Solutions. *J Res Nbs a Phys Ch* **1977,** *81* (1), 89-96.

CHAPTER FIVE:

FUTURE WORK AND CONCLUSIONS

5.1 FUTURE WORK

The work presented in this dissertation has expanded the understanding and utility of parameters controlling the crystallization of DNA-capped gold nanoparticles, without the need for specific base-pairing. Progress towards a complete elucidation of the dynamics of DNA-capped gold nanoparticles in solution has been discussed. As is often the case in research, the answering of such complex questions also lays the foundation to tackle new, more complicated questions. Thus, there still remains potential for further developments, which will be discussed here.

5.1.1 QCM-D Studies in Multivalent Cation Solutions

The QCM-D studies performed in Chapter 2 established two kinetic models for the adsorption of DNA-AuNPs on an APTES functionalized Si substrate. For non-base pairing DNA-AuNPs in high ionic strength $MgCl_2$ solutions the model was equivalent to a simple Langmuir isotherm. Repetition of these experiments in solutions of additional multivalent cations, such as $CaCl_2$ could establish this behavior as a general trend for adsorption in multivalent cation solutions. Or, perhaps, if the convergence to Langmuir adsorption at high ionic strength was not again observed in $CaCl_2$ this would confirm the specific interaction of Mg^{2+} counterions with DNA that have been proposed.[1]

5.1.2 Ordering at the Solid-liquid Interface

The experiments described in Chapter 2 were designed to establish a set of kinetic parameters that could enable the construction of long-range ordered two-dimensional crystallites at the solid-liquid interface. Unfortunately, scanning electron microscopy

studies of the adsorbed DNA-AuNPs did not indicate the establishment of ordered nanoparticle arrays. Even after heating at 200 °C, no significant reorganization of the nanoparticles was noticed, a process which has been shown to facilitate nanoparticle rearrangements[2]. This suggests a remarkably strong electrostatic adsorption of the DNA-AuNPs to the APTES functionalized surface, blocking the translational freedom needed to establish an ordered system. Testing the adsorption of the DNA-AuNPs on less densely charged surfaces, such as a film of the weak polyeletrolyte, polyacrylic acid, on which the electrostatic bond between the DNA ligands and the positively charged surface is weaker could potentially enable the rearrangements necessary to establish a two-dimensional superlattice. Fine-tuning would be imparted by either adsorbing the DNA-AuNPs at elevated temperature, or a temperature post-treatment of adsorbed DNA-AuNPs.

5.1.3 Elucidation of the Crystalline Transition of Three-dimensional Superlattices

Chapter three established evidence suggesting that the three-dimensional crystallization of DNA-AuNPs proceeds via a lattice shift from HCP to FCC. In lower ionic strength solutions HCP crystals were seen at both the air-liquid and solid-liquid interfaces. However, in the highest ionic strength solutions no HCP crystals were observed, and the only three-dimensional lattices observed were FCC. Elucidation of the dynamics of this mechanism could be performed via controlled drying of droplets. By placing a DNA-AuNP droplet of low ionic strength, before any three-dimensional crystals have been established in a sealed SAXS chamber with a reservoir at an ionic strength in which only FCC crystals are observed, the droplet would dry to the reservoir

concentration.[3] If the drying rate was sufficiently slow so that raster scans of the droplet could be obtained with reasonable frequency, the development of nanoparticle superlattices at both low and high concentrations, as well as the transition could be observed. This would be the first such case of measuring the electrolyte mediated nanoparticle crystallization mechanism in solution.

5.1.4 Imaging of Three-dimensional DNA-capped Gold Nanoparticle Superlattices

Rudimentary attempts were made to image the three-dimensional superlattices above by simply vacuum drying a droplet and transferring to the scanning electron microscope. Even during the transfer from the vacuum to the microscope, the hygroscopic magnesium chloride re-wetted the sample. This made imaging of the droplet by SEM difficult, as the presence of water in the SEM vacuum chamber severely reduces the resolution and promotes charging. Even still, clear surface structure and nanoparticle orientation was visible (Figure 5. 1). It is highly likely that this may just be the Gibbs monolayer, but the edges visible suggest otherwise. If vitrifying the ionic strength droplets proves possible, imaging by cryo-electron microscopy, where the droplet is frozen before imaging would eliminate these effects.[4]

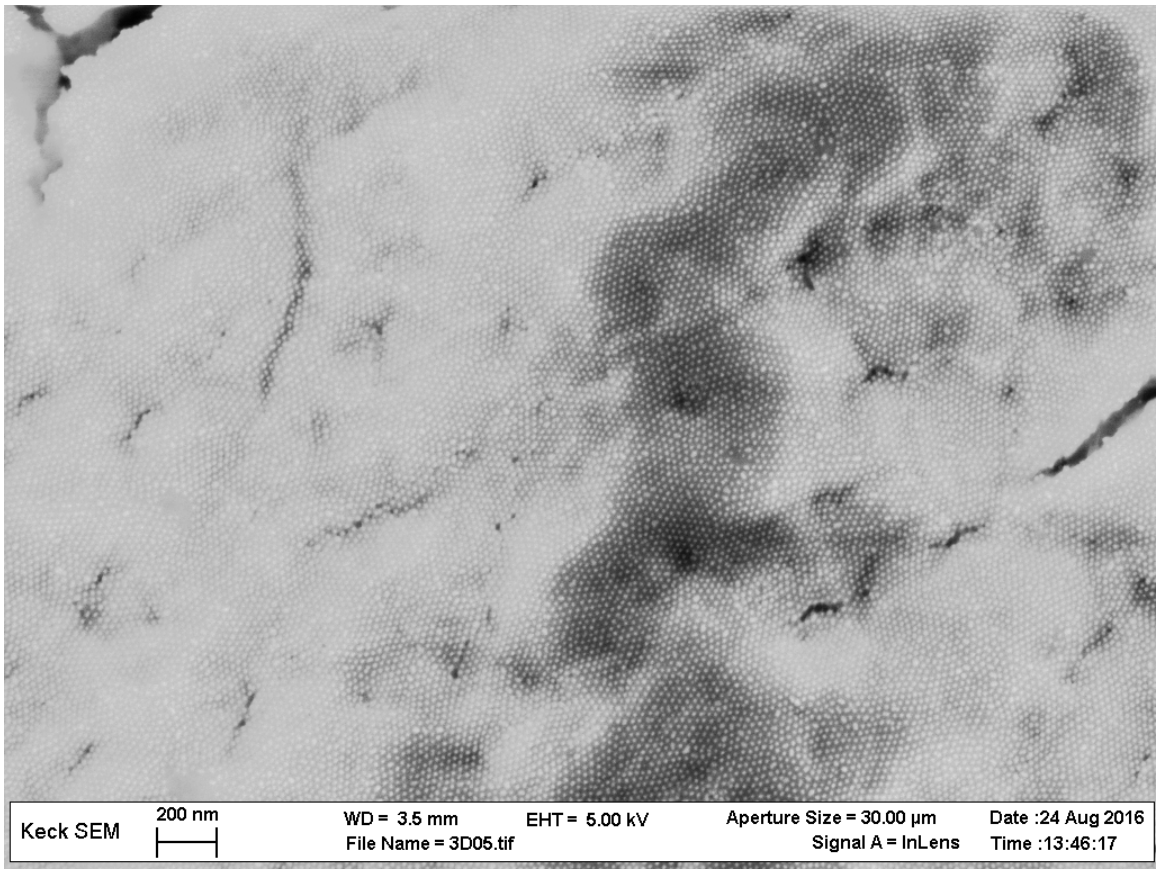

Figure 5. 1: Scanning electron micrograph of partially wetted DNA-AuNP droplet. While the presence of water in the sample made imaging difficult, the general orientation and three-dimensional nature of the nanoparticle lattice can be made out.

5.1.5 Multilayered Superlattices by Interfacial Superlattice Transfer

The superlattice transfer technique described in Chapter Four provides a powerful platform through which to reliably and rapidly create nanoparticle superstructures. An exciting direction forward would be to apply this technique to build multi-layered DNA-AuNP superlattices by repeated transfer steps. This would be achieved by first transferring the Gibbs monolayer onto the APTES functionalized silicon as previously outlined followed by controlled deposition of a thin film of the polyelectrolyte poly(allylamine hydrochloride). Subsequent lattice transfer and thin film growth would

enable the creation of multilayered nanoparticle superlattice (Figure 5. 2). Precise control of the number of layers, as well as layer spacing, as controlled by film growth time, and interparticle spacing, determined by ligand length would provide unprecedented control over the superstructures. Additionally, by alternating size and composition of the nanoparticles used in each layer, novel hybrid materials could be created.

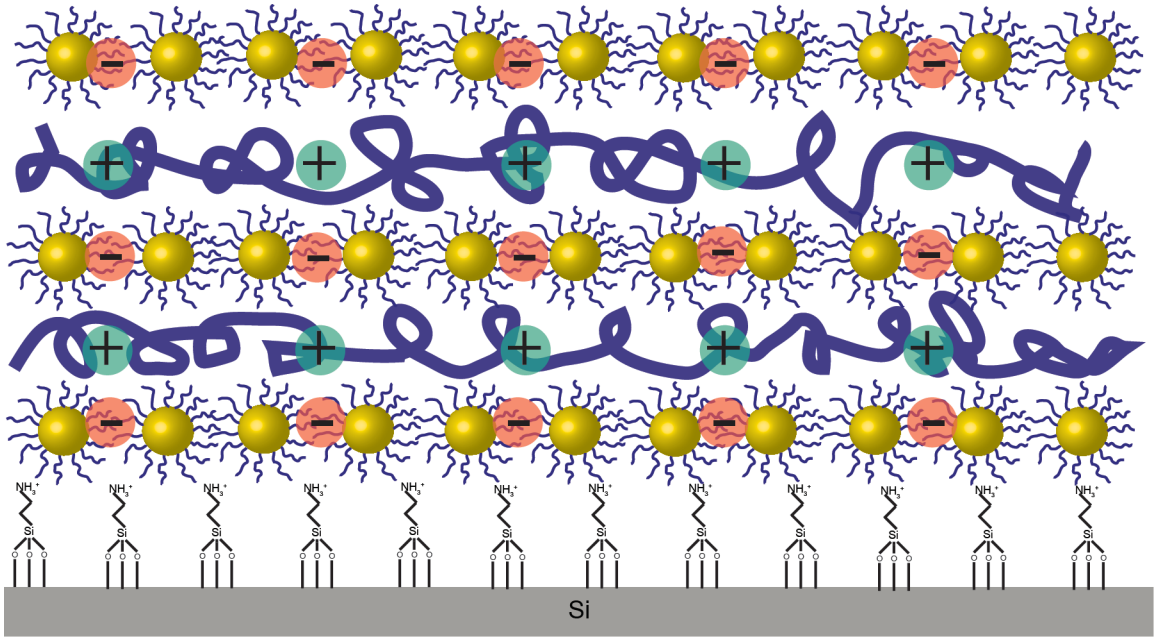

Figure 5. 2: Scheme depicting superlattice transfer method. Multilayered nanoparticle superlattices are proposed by first transferring an initial monolayer of DNA-AuNPs onto APTES silicon as previously described, followed by alternating polycation/nanoparticle deposition steps.

5.1.6 Optical Measurements on Aambiently Equilibrated DNA-capped Gold Nanoparticle Droplets

The surprising stability of the nanoparticle droplets described in section 4.3.2 allows the liquid droplets to be studied in ambient environments, without complicated experimental setups. A seen in Figure 4.13, the equilibrated droplets vary in their optical properties, namely their color and reflectivity. In fact this change of reflectivity, indicating metallic behavior is remarkable, given that the nanoparticles have not undergone a insulator-to-metal transition.[5] Coupled with the SAXS structure and spacing data, measurement of the optical properties of the droplet, and droplet surface would serve to further the theoretical understanding of the optical properties of collections of nanoparticles. Aside from providing a simple experimental system with which to test theoretical models, the droplet stability could be applied to systems where humidity dependent reflectivity is desired.

5.2 CONCLUSIONS

The collection of studies put forward in this dissertation have established methods which simply the DNA-mediated assembly of nanoparticles. By treating DNA not as a "programmable" ligand but instead a short polyanion, solution electrostatics could be tuned to create various morphological assemblies. A shown, both two- and three-dimensional nanoparticle superlattices could be constructed, showing that the utility of DNA is not lost in such a simple system. Furthermore the solution phase parameters dictating the adsorption on a positively charged substrate were modeled, providing

important insights into the adsorption kinetics and mechanism. Taken together, it is expected that these findings will contribute to the application of nanoparticle self-assembly, ultimately resulting in novel optoelectronic devices

REFERENCES

1. Kirmizialtin, S.; Elber, R., Computational exploration of mobile ion distributions around RNA duplex. *J Phys Chem B* **2010,** *114* (24), 8207-20.

2. Goodfellow, B. W.; Rasch, M. R.; Hessel, C. M.; Patel, R. N.; Smilgies, D. M.; Korgel, B. A., Ordered structure rearrangements in heated gold nanocrystal superlattices. *Nano Lett* **2013,** *13* (11), 5710-4.

3. Campolongo, M. J.; Tan, S. J.; Smilgies, D. M.; Zhao, M.; Chen, Y.; Xhangolli, I.; Cheng, W.; Luo, D., Crystalline Gibbs monolayers of DNA-capped nanoparticles at the air-liquid interface. *ACS Nano* **2011,** *5* (10), 7978-85.

4. Stewart, P. L., Cryo-electron microscopy and cryo-electron tomography of nanoparticles. *Wiley Interdiscip Rev Nanomed Nanobiotechnol* **2016**.

5. Young, K. L.; Ross, M. B.; Blaber, M. G.; Rycenga, M.; Jones, M. R.; Zhang, C.; Senesi, A. J.; Lee, B.; Schatz, G. C.; Mirkin, C. A., Using DNA to design plasmonic metamaterials with tunable optical properties. *Adv Mater* **2014,** *26* (4), 653-9.